Imperial College London
Department of Physics

A Study of Stratosphere-troposphere Coupling with an Aquaplanet Model

Jacob Ching Ho Cheung

Aug 2011

Supervised by Prof Joanna Haigh, Dr Arnaud Czaja

Submitted in part fulfilment of the requirements for the degree of
Doctor of Philosophy in Physics of Imperial College London
and the Diploma of Imperial College London

Declaration

I herewith certify that all material in this dissertation which is not my own work has been properly acknowledged.

Jacob Ching Ho Cheung

Abstract

The coupling between stratosphere and troposphere (ST) has been studied extensively using simple circulation models. It is known that the ozone-rich stratosphere interact with the troposphere through both radiative and dynamical processes. However, many of the models used in these studies only assume a slab ocean with a fixed sea surface temperature (SST) profile.

To investigate the role of the ocean in the stratosphere-troposphere coupling, a fully coupled atmosphere-ocean model, FORTE (Fast Ocean Rapid Troposphere Experiment) is used in this study. In this project the Earth is modelled as a perfect sphere with its surface covered with water. In the first set of our experiments we introduce a perturbation to the stratosphere by increasing ozone concentration by a factor of five. In the second experiment we repeat the ozone perturbation experiment with a fixed SST profile such that the atmosphere-ocean coupling is shut off.

Our results demonstrate that by including a dynamical ocean, the strength of the jet streams is less sensitive to stratospheric ozone perturbations whereas the extent of their latitudinal displacements is greater. Both of these are found to be a consequence of SST anomalies induced by ocean dynamics. On the other hand, our results show that in the presence of an interactive ocean, there is a general increase in tropospheric air temperature except for polar regions, while lacking the banded anomaly pattern observed in our fixed SST experiment and other ST coupling studies.

Acknowledgements

Firstly I would like to express my gratitude to both of my supervisors, Prof. Joanna Haigh and Dr. Arnaud Czaja, who have supported me throughout my PhD with their knowledge and patience. This thesis would not have been completed without their encouragements and attentiveness, which kept me reassured through many of the hard moments in my PhD.

My work was jointly funded by Higher Education Funding Council for England and my family. On the technical side, I would like to thank Dr. Richard Bantges for setting FORTE up locally at Imperial College London. I would also like to give thanks to Dr. Bablu Sinha and Dr. Adam Blaker from the National Oceanography Centre for their help with some of the technical issues in FORTE.

Contents

List of Figures **9**

List of Tables **19**

List of Symbols and Abbreviations **20**

1. Introduction **26**
1.1. Overview . . . 26
1.1.1. Stratosphere-Troposphere Coupling . . . 26
1.1.2. Atmosphere-Ocean Coupling . . . 32
1.1.3. Aim of Study . . . 36
1.2. Atmosphere . . . 37
1.2.1. Chemical composition . . . 37
1.2.2. General Circulation . . . 39
1.2.3. The Stratosphere-Troposphere System . . . 42
1.2.4. Equation of motion . . . 45
1.2.5. Energy Budget . . . 49
1.3. Ocean . . . 51
1.3.1. General Circulation . . . 51
1.3.2. Energy Budget . . . 53

2. Experimental Setup **58**
2.1. Model Requirements . . . 58
2.2. Description of FORTE . . . 60
2.2.1. Atmospheric Component - IGCM3 . . . 62
2.2.2. Ocean Component - MOMA . . . 66
2.2.3. Coupler - OASIS . . . 67
2.3. Hardware Specification . . . 68
2.4. Model Setup . . . 68

2.5. Aquaplanet Climatology 72
2.5.1. Atmosphere 73
2.5.2. Ocean 83
2.5.3. Sea Temperature Drift 87

3. Results: Ocean **92**
3.1. Changes in Surface Conditions 93
3.1.1. Windstress 93
3.1.2. Ekman Transport 94
3.1.3. Sea Surface Temperature 96
3.2. Meridional Overturning Circulation 98
3.3. Sea Potential Temperature 100
3.3.1. Global Mean 100
3.3.2. Meridional and Vertical Structure 102
3.4. Redistribution of Ocean Heat Content 104
3.4.1. Changes to Vertical Structure 104
3.4.2. Mechanism 105
3.5. Summary and conclusions 109

4. Results: Atmosphere **113**
4.1. Zonal Wind 114
4.2. Meridional Circulation 117
4.3. Transient Eddy Momentum Fluxes 121
4.3.1. Decomposition of the Circulation 121
4.3.2. Meridional Structure 122
4.3.3. Wavenumber Analysis 124
4.3.4. Origin of the Equatorial Transient Eddies 125
4.4. Eddy Fluxes and Feedbacks 129
4.4.1. Steady and Non-Dissipative Flow 129
4.4.2. Eddy Feedbacks 130
4.4.3. Vertically Integrated Momentum Budget 134
4.5. Summary and Conclusions 140

5. Results: Energy Budgets **144**
5.1. Air Temperature 145
5.1.1. Stratosphere 145
5.1.2. Troposphere 145

5.2. Moist Static Energy 147
5.2.1. Stratosphere 147
5.2.2. Troposphere 149
5.3. Radiation Budget 149
5.3.1. TOA 151
5.3.2. Surface 158
5.4. Remarks 166
5.5. Summary and Conclusions 168

6. Summary and Conclusions **169**
6.1. Future Work 176

Bibliography **178**

A. Derivation of Equations **188**
A.1. Motion in a Rotating System 188
A.2. Hydrostatic Equilibrium 189

B. Technical Issues **190**
B.1. Vertical Sea Water Velocity 190

C. IGCM3 Updates **192**
C.0.1. Extracting SST Data 192
C.0.2. Reading SST Data 193
C.0.3. Radiative Flux Output at Every Model Level 194

List of Figures

1.1. Time and zonally averaged zonal wind, as a function of latitude and pressure, for the experiment with a) no polar vortex in the stratosphere, b) $\gamma = 1$, c) $\gamma = 2$, d) $\gamma = 3$, e) $\gamma = 4$, where γ denotes the lapse rate at the winter pole and has the units $[K/km]$. γ is a parameter which controls the stratospheric temperature profile and the strength of the polar vortex. The contour level is 10 ms^{-1}. Negative contours are dashed. [50] 28

1.2. Meridional sections of the primary mean, eddy, and spectral fields for different stratospheric temperatures T_s. Labels at the top of each panel indicate the field depicted, the contour interval (CI). The contours have units: (a1)-(a3) ms^{-1}, (b1)-(b3) K, (c1)1)-(c3) s^{-1}, (d1)1)-(d3) Kms^{-1}, (e1)-(e3) m^2s^{-2}, (f1)-(f3) Kms^{-1}, and (g1)-(g3)m^2s^{-2}. The negative (zero) contours are dashed (dotted). The additional thick contour in the temperature fields indicates the position of the radiative relaxation tropopause.[68] 29

1.3. Same as figure 1.2 but for higher stratospheric temperatures T_s.[68] 30

1.4. SOI (solid) and SST anomaly [K] in the equatorial east Pacific Ocean (dashed) for period 1951-2000. [44] 35

1.5. A typical mid-latitude vertical temperature profile [65] 38

1.6. Annual mean absorbed solar radiation, emitted long-wave radiation, and net radiation. [44] 40

1.7. Schematic streamlines for a positive eddy momentum flux. The x- and y-axis denotes eastward and northward directions. [26] 41

1.8. Schematic of locations of jet streams and the general circulation pattern (Taken from NOAA National Weather Service webpage) 42
1.9. Simplified schematic illustrating the thermal wind relationship. 43
1.10. Schematic of Brewer-Dobson circulation (Bottom arrows) and the solstitial middle atmosphere circulation (Top arrows) [1] . 45
1.11. Schematic showing relative positions of surface winds and Ekman transport [44] 52

2.1. Schematics of Waterworld (Left), Ridgeworld (Middle) and Drakeworld (Right). Bottom row shows the plain view of each setup. Black denotes sea surface and grey denotes land. Both the seafloor and land are uniformly flat. [60] 62
2.2. Time-latitude plot of surface albedo at year 1020 (close equilibrium). White areas indicate the latitudes where there is no incident solar radiation around solstice. 69
2.3. Time-averaged zonal mean ozone profile near the tropopause in parts per million (ppm) (top). Ratio of the applied annual mean ozone perturbation at year 1020 and its original value (bottom). Note that the prescribed ozone has a seasonal cycle and hence the boundary of the perturbation is not exactly 5 times its original value when averaged annually. 71
2.4. Zonal mean air temperature (control) for annual-mean (top), DJF (middle) and JJA (bottom) conditions. Data averaged over years 1020-1035 [^oC]. Contour interval = 5^oC. 75
2.5. Zonal mean cross sections of air temperature (control) for annual-mean (top), DJF (middle) and JJA (bottom) conditions in ^oC [48] 76
2.6. Annual mean precipitation (control), averaged over years 1020-1035 [$mmday^{-1}$]. 77
2.7. Zonal mean zonal(contour) and meridional(meridional) wind field (control), averaged over years 1020-1035 [ms^{-1}]. Contour intervals are $5ms^{-1}$ for the zonal plot and $0.1ms^{-1}$ for the meridional plot. 78

2.8. Zonal mean cross sections of zonal wind (control) for annual-mean (top), DJF (middle) and JJA (bottom) conditions in ms^{-1}. Vertical profiles of hemispheric and global mean values are shown on the right. [48] 79
2.9. Zonal mean cross sections of the mass stream function, averaged over years 1020-1035 [$10kgs^{-1}$]. Contour intervals are $10kgs^{-1}$. Solid (dotted) lines shown clockwise (anticlockwise) circulation. 81
2.10. Zonal mean cross sections of the mass stream function in $10^{10}kgs^{-1}$ for annual, DJF, and JJA mean conditions. Vertical profiles of the hemispheric and global mean values are shown on the right [48]. 82
2.11. Time series of TOA net radiation (top) and its components (bottom), in Wm^{-2} in the control run. SW and LW denotes shortwave and longwave radiation respectively. The direction is indicated in the subscript in each legend entry. 84
2.12. Annual mean SST [^oC] and surface currents [cms^{-1}] (control), averaged over years 1020-1035. 85
2.13. Zonal mean meridional overturning circulation in the ocean (control), averaged over years 1020-1035 [Sv]. Contour interval = $10Sv$. Solid (dotted) line denote clockwise (anticlockwise) circulation. 86
2.14. Zonal mean sea potential temperature (control), averaged over years 1020-1035 [^oC]. Contour interval = 2^oC 88
2.15. Vertical profile of sea potential temperature (control), averaged over years 1020-1035 [^oC] 89
2.16. Time-integrated net downward energy flux (radiative+sensible+latent) at the surface (green) and time series of ocean heat content change (red) since model year 1020 [J]. Black curve shows the difference between the two. 90
2.17. Time series of annual mean sea potential temperature in K. . 91

3.1. Zonal mean zonal wind stress τ_x for the control (Red) and $x5O_3$ (Blue) run, averaged over years 1020-1035 [Nm^{-2}]. Errorbars show the standard deviations of the annual mean zonal wind stress for each latitude. 93

3.2. Top: Time series of global mean SST for the control (red) and $x5O_3$ (blue) run, averaged over years 1020-1035 $[K]$. Bottom: Global mean SST anomalies ($x5O_3$-Control) $[K]$. 97
3.3. Contour: MOC anomalies ($x5O_3$-Control), averaged over years 1020-1035 $[Sv]$. Contour interval = $1Sv$. Control MOC is shown in color for reference. 99
3.4. Top panel: Global mean sea potential temperature for the control (red) and $x5O_3$ (blue) runs $[K]$. Bottom panel: Global mean sea potential temperature anomalies ($x5O_3$-Control) . . 101
3.5. Change in sea potential temperature for 0-1000m(top panel) and 1000-5000m (bottom panel), averaged over years 1020-1035 $[^oC]$. Contour interval = 0.025^oC. 103
3.6. Time series of change in ocean heat content, after a perturbation of 5 times O_3 has been applied at model year 1020. $[J]$. 106
3.7. Schematic of a slab of ocean. 107
3.8. Time series of change in ocean heat content due to vertical advection, after a perturbation of 5 times O_3 has been applied at model year 1020. $[J]$. 110
3.9. Same as figure 3.9, but with the model levels within the top $300m$ taken as a single layer. 111

4.1. Black contours: Zonal mean zonal wind for $x5O_3$ (top) and $x5O_{3FSST}$ (Bottom). Colored contour plot shows the control zonal wind field for comparison $[ms^{-1}]$. 115
4.2. Black contours: Difference in zonal mean zonal wind between the two ozone experiments ($x5O_{3FSST}$ - $x5O_3$). Colored contour plot shows the $x5O_3$ zonal wind field for reference $[ms^{-1}]$.116
4.3. Change in zonal mean zonal wind for $x5O_3$ (top) and $x5O_{3FSST}$ (bottom) $[ms^{-1}]$. 118
4.4. Change in atmospheric mass streamfunction for $x5O_3$ (top) and $x5O_{3FSST}$ (bottom) runs. The control is plotted in color in the background for reference. $[10^{10}kgs^{-1}]$. Contour intervals are $0.2 \times 10^{10}kgs^{-1}$ in all cases 120
4.5. Northward transport of momentum flux by transient eddies for the control run $[m^2s^{-2}]$. Contour intervals are $5m^2s^{-2}$. . . 123

4.6. DJF Transient eddy momentum flux (Control) by different wavenumbers. Wavenumber increases from 0 to 3 in the left column and from 4 to 7 in the right column $[m^2 s^{-2}]$. Contour intervals are $2m^2 s^{-2}$. 126
4.7. Same as figure 4.6, but for NCEP data 127
4.8. Annual mean $[\overline{u'v'}]$ for the control run (top) and the control run with clouds removed from the radiation scheme in IGCM3. Data is computed and averaged over a period of 5 years (585-590). 128
4.9. Zonal mean eddy momentum flux $[u^* v^*]$ for the control run. Contour intervals = $2m^2 s^{-2}$. 131
4.10. Zonal mean eddy momentum flux anomalies $[u^* v^*]$ for the $x5O_3$ (top) and $x5O_{3FSST}$ (bottom) runs. Contour intervals = $1m^2 s^{-2}$. Signals that does not reach a 95% confidence level are shaded. 132
4.11. Terms in the vertically integrated zonal momentum equation for the control run $[Nm^{-2}]$. 137
4.12. Magnitudes of C_{Eddy} (green) term in the control run, calculated using different model output intervals: 90 mins, 1 day, 2days, 4days (see legend). Only data from year 1020 is used. C_{Zonal} (red), surface stress (blue) are constant in all cases and are plotted as a reference. The corresponding residuals (magenta) in the vertical momentum budget for each output interval are also plotted. All units in $[Nm^{-2}]$. 138
4.13. Anomaly of different terms in the vertically integrated zonal momentum equation for $x5O_3$ (top) and $x5O_{3FSST}$ (bottom) $[Nm^{-2}]$. 141

5.1. Air temperature anomalies for $x5O_3$ (top) and $x5O_{3FSST}$ (bottom) runs [K]. Regions that does not reach the 95% significance level are shaded. Contour intervals = $2K$. 146
5.2. Same as figure 5.1, but contour levels are chosen to put emphasis on the anomalies in the troposphere. Contour intervals = $0.05K$. 148

5.3. Globally integrated stratospheric (top) and tropospheric (bottom) moist static energy anomaly for $x5O_3$ (solid) and $x5O_{3FSST}$ (dashed) [J]. 150
5.4. Global mean upward shortwave radiative flux ($F_{SW\uparrow}$) anomalies at TOA for $x5O_3$ (Red) and $x5O_{3FSST}$ (Blue) [Wm^{-2}]. . 152
5.5. Global mean upward longwave radiative flux ($F_{LW\uparrow}$) anomalies at TOA for $x5O_3$ (Red) and $x5O_{3FSST}$ (Blue) [Wm^{-2}]. . 153
5.6. Global mean net (SW+LW) downward radiative flux anomalies at TOA for $x5O_3$ (red) and $x5O_{3FSST}$ (blue) [Wm^{-2}]. . . 154
5.7. Time series (360-day-smoothed) of global mean net (SW+LW) downward radiative flux at TOA for control (black), $x5O_3$ (red) and $x5O_{3FSST}$ (blue) [Wm^{-2}]. 157
5.8. Global mean upward (solid) and downward (dashed) shortwave radiative flux anomalies at sea surface for $x5O_3$ (red) and $x5O_{3FSST}$ (blue) [Wm^{-2}]. 159
5.9. Global mean upward (solid) and downward (dashed) longwave radiative flux anomalies at sea surface for $x5O_3$ (red) and $x5O_{3FSST}$ (blue) [Wm^{-2}]. 160
5.10. Global mean upward latent (solid) and sensible (dashed) heat flux anomalies at sea surface for $x5O_3$ (red) and $x5O_{3FSST}$ (blue) [Wm^{-2}]. 161
5.11. Global mean net (SW+LW+sensible+latent) downward energy flux anomalies at sea surface for $x5O_3$ (Red) and $x5O_{3FSST}$ (Blue) [Wm^{-2}]. 164
5.12. Time series of gain in ocean heat content (red) and time-integrated total net downward energy flux at the surface (green) since year 1020 for the control run [J]. Residual of the two is shown in black. 165
5.13. Time series of gain in moist static energy (red) and time-integrated net (TOA-Surface) global energy flux into the atmosphere (green) since year 1020 for the control run [J]. Residual of the two is shown in black. 167

A.1. A vertical column of air of density ρ, area A, height δz, and mass m. The pressure acting at the top and bottom of the column are $p(z+\delta z)$ and $p(z)$ respectively. 189

B.1. Annual mean vertical sea water velocity at 79^oN (top) and 79^oS (bottom) $[ms^{-1}]$. 191
B.2. Time averaged zonal mean vertical sea water velocity calculated using equation B.1 $[ms^{-1}]$. 191

List of Tables

1.1. Scale analysis of the zonal momentum equation 46

3.1. Comparison of $\vec{v}_{ek}$ and $\vec{v}_{Actual}$ at different latitudes in the NH. 3^{rd} and 4^{th} column shows their values in the control and $x5O_3$ run respectively. Positive (negative) values indicate poleward (equatorward) transport. 5^{th} column shows the % change of poleward transport after the ozone perturbation has been applied. 95

5.1. Change in SW and LW radiative flux at TOA, averaged over year 1020-1035 $[Wm^{-2}]$. The standard deviations of their annual means are also shown. Terms that have a negative contribution to the energy of the system are marked with †. . 155

5.2. Global mean cloud fraction for high, middle, low and convective clouds for $x5O_3$ and $x5O_{3FSST}$ runs. 156

5.3. Change in radiative, sensible heat and latent heat flux at surface, averaged over year 1020-1035 $[Wm^{-2}]$. The standard deviations of their annual means are also shown. Terms that have a negative contribution to the ocean heat content are marked with †. 163

List of Symbols and Abbreviations

A_C	Fractional cloud cover
c_{pa}	Specific heat of air at constant pressure ($= 1004 Jkg^{-1}K^{-1}$)
c_{po}	Specific heat of sea water at constant pressure ($\approx 4187 Jkg^{-1}K^{-1}$)
c_{va}	Specific heat of air at constant volume ($= 717 Jkg^{-1}K^{-1}$)
C_D	Drag coefficient
C_{Deep}	Deep convective cloud fraction
C_{High}	High-level cloud fraction
C_{Low}	Low-level cloud fraction
C_{Mid}	Mid-level cloud fraction
$C_{Shallow}$	Shallow convective cloud fraction
dQ	Change of heat
dW	Work done
dU_{adv}	Change of ocean heat content due to vertical advection of temperature
D	(1) Depth
	(2) Vorticity
f	Coriolis parameter ($= 2\Omega sin\phi$)
$\vec{F}_{Friction}$	Frictional force
$F_{Latent\uparrow}$	Upward latent heat flux
$F_{LW\downarrow}$	Downward longwave flux
$F_{LW\uparrow}$	Upward longwave flux
$F_{Net\downarrow}$	Net downward energy flux
$F_{Sensible\uparrow}$	Upward sensible heat flux
$F_{SW\downarrow}$	Downward shortwave flux
$F_{SW\uparrow}$	Upward shortwave flux
F_λ	Frictional force in zonal direction
g	Gravitaional constant ($= 9.81 m^2 s^{-2}$)
H	Enthalpy
H_a	Moist static energy of atmosphere
k	Zonal wavenumber

K	von Kármán constant
L_λ	Length of latitude circule in metres
$\vec{m}_{ek}$	Ekman mass transport
p	Pressure
p_s	Surface pressure
R	Mean radius of the Earth ($\approx 6371km$)
R_a	Specific gas constant of dry air ($= 286.9 Jkg^{-1}K^{-1}$)
RH	Relative Humidity
R_{Prep}	Time-averaged precipitation rate in mm/day
S	Salinity
T_r	Transmittance
u	Zonal component of wind
$\vec{U}_{ek}$	Ekman current
U	Internal energy
$\vec{U}_A$	Absolute velocity view from an inertial frame
$\vec{U}_o$	Horizontal component of ocean current
U_o	Internal energy of ocean
$\vec{U}_r$	Velocity relative to the rotating frame
$\vec{v}_{ek}$	Meridional component of Ekman current
v	Meridional component of wind
$\vec{v}_o$	Meridional component of ocean current
V	Volume
$\vec{w}_o$	Vertical component of ocean current
z	(1) Geometric Height
	(2) Depth
$d\eta$	Change of entropy
ϵ	Cloud emissivity
λ	Longitude
ω	Vertical component of wind
$\vec{\Omega}$	Angular velocity of the Earth ($7.292 \times 10^{-5} rads^{-1}$)
μ	Effective chemical potential for salinity
ϕ	Latitude
ψ_a	Mass streamfunction for atmosphere
ρ_a	Density of air
ρ_o	Density of sea water
σ	Sigma level ($= \frac{p}{p_s}$)

θ	Sea potential temperature
$\vec{\tau}$	Surface wind stress
τ_A	Optical depth of atmosphere
τ_C	Optical depth of cloud
τ_u	Zonal component of wind stress
ζ	Vorticity

ACC	Antarctic Circumpolar Current
AOGCM	Atmosphere-ocean coupled general circulation model
Br	Bromine
CERFACS	Certer Europeen et de Formation Avancee en Calcul Scientifique
CFCs	Chlorofluorocarbons
CH_4	Methane
Cl	Chlorine
CO_2	Carbon dioxide
DJF	December, January, February
ENSO	El Niño Southern Oscillation
FORTE	Fast Ocean, Rapid Troposphere Experiment
GCM	General circulation model
GFDL	Geophysical Fluid Dynamics Laboratory
H_2O	Water vapour
HadCM3	Hadley Centre Coupled Model, version 3
IGCM3	Intermediate General Circulation Model (IGCM3)
IR	Infrared
ITCZ	Intertropical Convergence Zone
JJA	June, July, August
LW	Longwave
LWP	Liquid water path
MOC	Meridional Overturning Circulation
MOMA	Modular Ocean Model, Array Version (MOMA)
N_2	Nitrogen
NCEP-NCAR	National Centers for Environmental Prediction-National Center for Atmospheric Research
NH	Northern hemisphere
N_2O	Nitrous oxide
NO	Nitric oxide
NWP	Numerical weather prediction
O_2	Oxygen
O_3	Ozone
OASIS	Ocean Atmosphere Sea Ice Soil coupler
OH	Hydroxide
$RWBM$	Reading Wide Band Model
SH	Southern hemisphere

SW	Shortwave
SLP	Sea level pressure
SOI	Southern oscillation index
SST	Sea surface temperature
ST	Stratosphere-troposphere
TOA	Top of atmosphere
UV	Ultraviolet
$x5O_3$	x5 ozone experiment
$x5O_{3FSST}$	x5 ozone experiment with fixed SST

$\overline{A} = \frac{1}{t_2 - t_1} \int_{t_1}^{t_2} A d\lambda$	Time average of A
$A' = A - \overline{A}$	Departure from time average of A
$[A] = \frac{1}{2\pi} \int_0^{2\pi} A d\lambda$	Zonal average of A
$A^* = A - [A]$	Departure from zonal average of A

1. Introduction

1.1. Overview

The Earth's climate is governed by the global circulations of the ocean and atmosphere. Understanding these circulations and the mechanisms of how they respond to different forcing, such as changes in solar irradiance, greenhouse gases, and aerosols etc, will aid the prediction of climate in the future.

In recent years, there have been an increasing number of studies suggesting the stratosphere and troposphere are coupled and that climate forcings that have a direct impact on the stratosphere could further induce adjustments in the troposphere. However, as most of these studies do not take account of the ocean dynamics, it is unknown that whether incorporating an interactive ocean into the climate models used in these studies will affect current findings.

1.1.1. Stratosphere-Troposphere Coupling

Evidence

Early evidence of stratosphere-troposphere (ST) coupling was found in a general circulation model (GCM) study by Haigh [20]. She suggested that stratospheric O_3 needs to be taken into account in order to assess the extent solar variability affects Earth's climate. Given that O_3 is a strong absorber of ultraviolet (UV) radiation and recalling the fact that solar radiation varies the most in the UV band, her finding is reasonable. In the study, Haigh simulated changes in incoming solar irradiance and its subsequent impact on stratospheric ozone to investigate the response of the Earth's climate system to the 11-year solar cycle using a general circulation model. It was found that as the stratosphere warms up during solar maximum, the stratospheric easterly wind also gets stronger. The strengthened wind penetrates down

into the troposphere and displaces the tropospheric jet poleward. The response was found to be much weaker in the case which only solar irradiance is increased. In a later study, Haigh et al. [22] reproduced a qualitatively similar tropospheric response by applying a temperature perturbation in the stratosphere.

Using simple thermal wind arguments, a change in the equator-to-pole temperature gradient in the stratosphere would result in a change in the wind field. With a simple GCM, Polvani & Kushner showed that as the stratospheric cooling lapse rate is increased, the stratospheric jet strengthens and is accompanied by a poleward shift of the tropospheric jet [50] (shown in figure 1.1). Note in the extreme case (figure 1.1 d & e), the stratospheric winds propagate downward and interact with the tropospheric jets at mid latitudes, forming a dipolar pattern.

These model results were confirmed to be consistent with observational data in a study by Baldwin [2], in which he studied anomalous zonal zonal-mean wind at 10hPa 60N, selecting 31-day long periods with strong vortices and compared with the ones when the vortices were at its weakest.

On the other hand, by increasing the stratospheric temperature (i.e lowering the tropopause), Williams [68] showed that there is a weakening and an equatorward shift of 2° of the tropospheric jet for every $5K$ increase in temperature in the stratosphere. The results are shown in figures 1.2 & 1.3. Although this is a different experiment to that of [50], Williams showed that as the stratosphere is heated sufficiently, the stratospheric wind and troposperhic jets will combine and form a double-jet state, which is qualitatively similar to the results of [50].

Using a simplified GCM, Haigh, Blackburn & Day [22] (hereby after HBD05) performed perturbation experiments by changing the temperature structure of the lower stratosphere. It was found that an uniform heating of the lower stratosphere at all latitudes results in a weakening and equatorward shift of the jets. On the other hand, in the case where an equatorial heating was applied to the lower stratosphere, a weakening and poleward shift of the jets was observed.

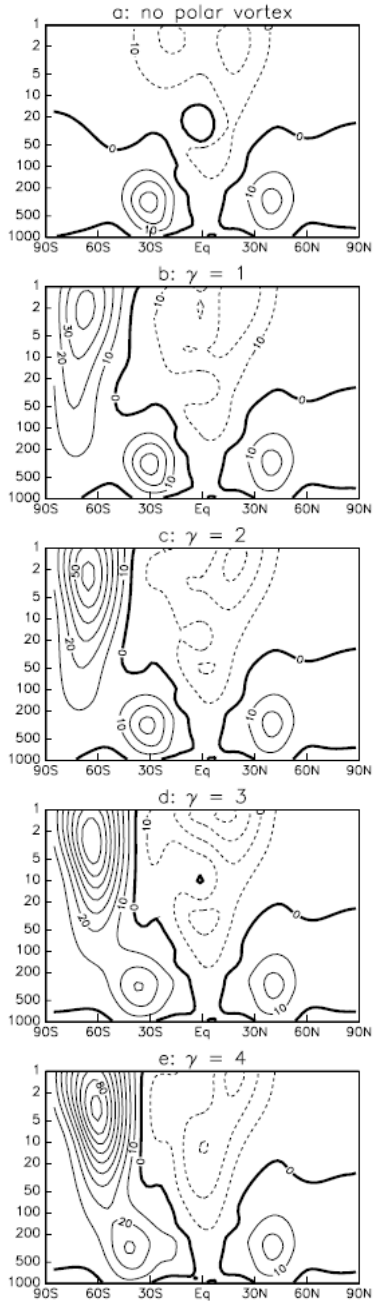


Figure 1.1.: Time and zonally averaged zonal wind, as a function of latitude and pressure, for the experiment with a) no polar vortex in the stratosphere, b) $\gamma = 1$, c) $\gamma = 2$, d) $\gamma = 3$, e) $\gamma = 4$, where γ denotes the lapse rate at the winter pole and has the units $[K/km]$. γ is a parameter which controls the stratospheric temperature profile and the strength of the polar vortex. The contour level is 10 ms^{-1}. Negative contours are dashed. [50]

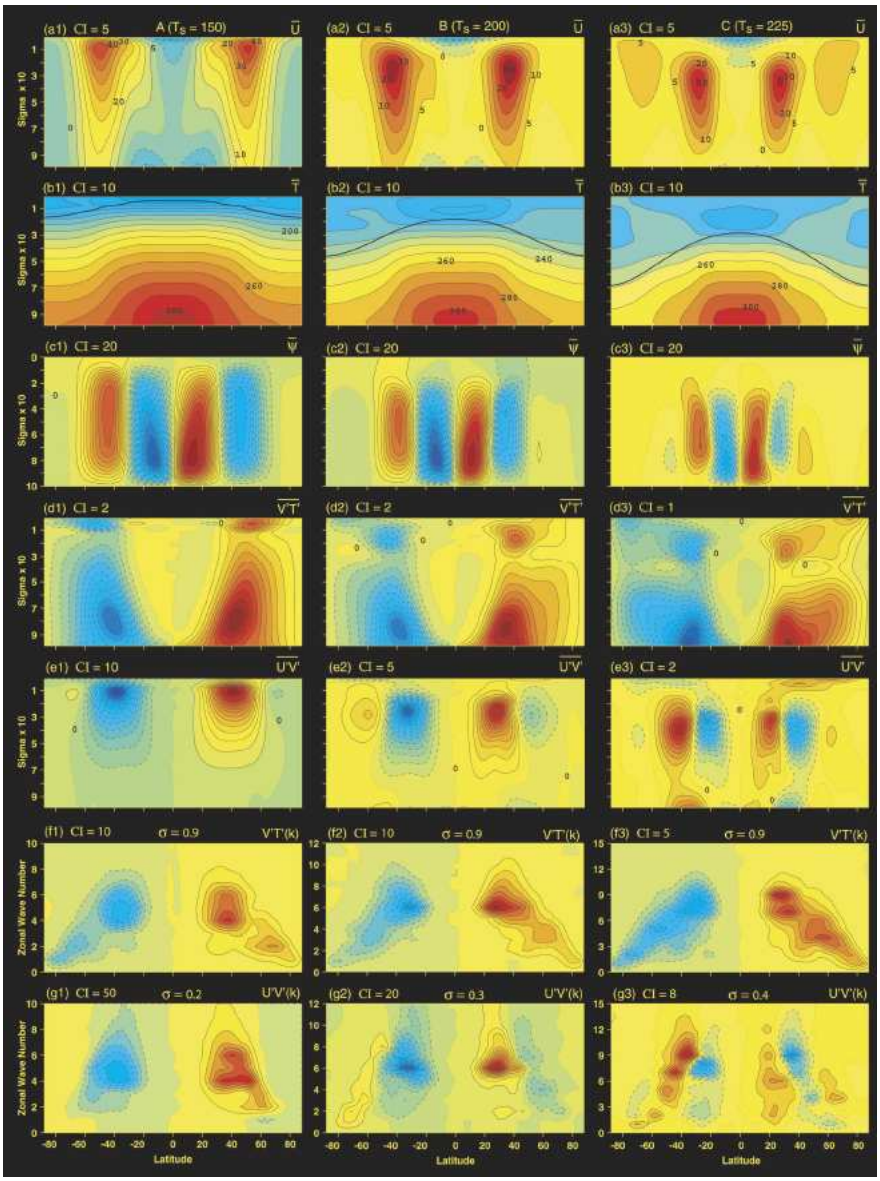


Figure 1.2.: Meridional sections of the primary mean, eddy, and spectral fields for different stratospheric temperatures T_s. Labels at the top of each panel indicate the field depicted, the contour interval (CI). The contours have units: (a1)-(a3) ms^{-1}, (b1)-(b3) K, (c1)1)-(c3) s^{-1}, (d1)1)-(d3) Kms^{-1}, (e1)-(e3) m^2s^{-2}, (f1)-(f3) Kms^{-1}, and (g1)-(g3)m^2s^{-2}. The negative (zero) contours are dashed (dotted). The additional thick contour in the temperature fields indicates the position of the radiative relaxation tropopause.[68]

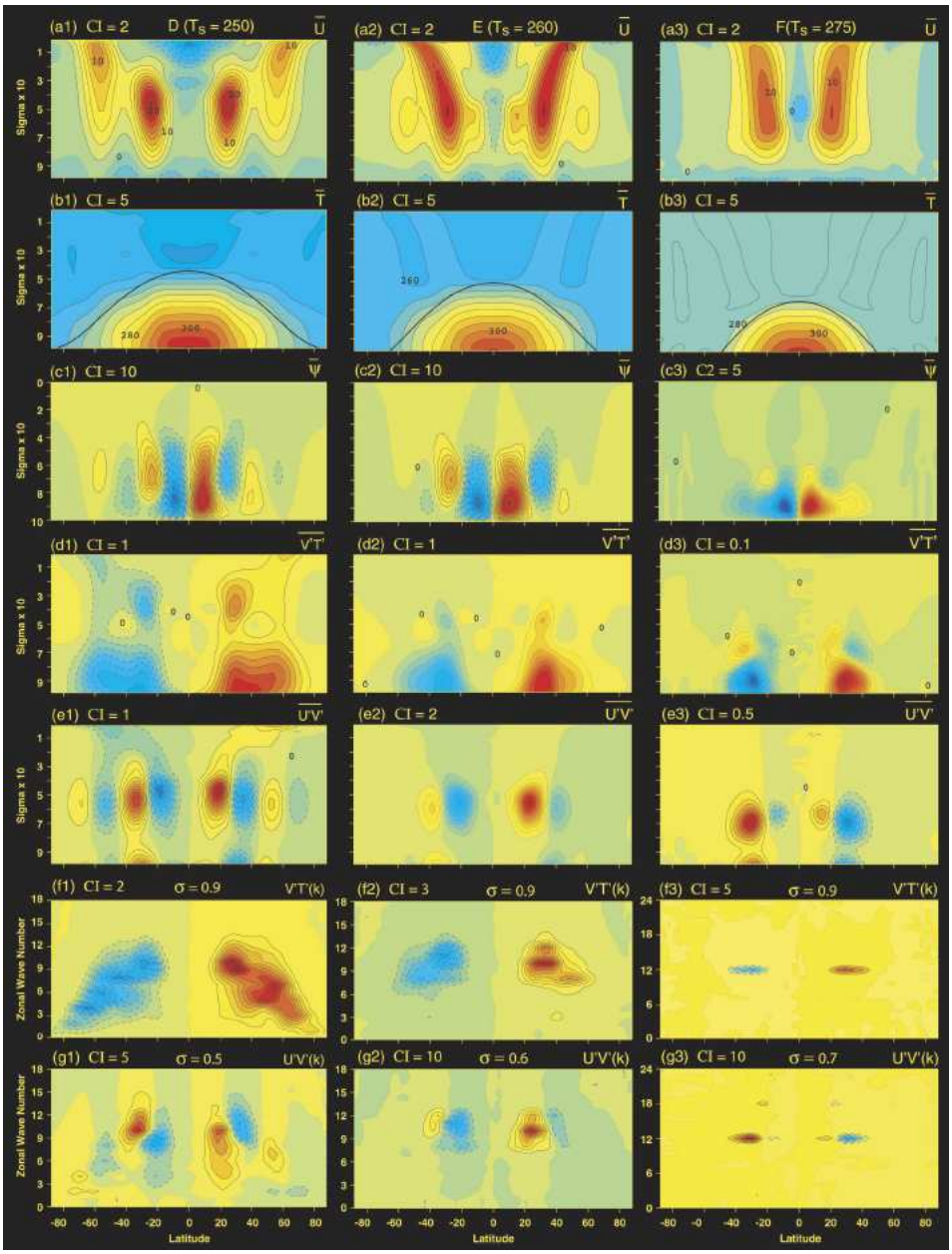


Figure 1.3.: Same as figure 1.2 but for higher stratospheric temperatures T_s.[68]

On the other hand, HBD05 performed a multiple regression analysis of the NCEP-NCAR reanalysis dataset to zonal mean zonal wind fields and concluded that there is also a weakening and poleward shift of the subtropical jet in response to increased solar activity. Qualitatively, this agrees well with the result from their equatorial heating experiment, which is an analogous situation to solar maximum.

As will be mentioned in section 1.2.1, the temperature of the atmosphere is determined by the abundance of different gases. For example, the majority of ozone lies within the mid-stratosphere and will affect the temperature & radiation budget by means of absorption & photochemical dissociation. By simulating the effect of ozone depletion in the stratosphere, Keeley [31] showed that Antarctic stratospheric ozone below 164 hPa plays an insignificant role in the tropospheric response while depleting ozone above 164hPa gives a similar pattern to the case which the full stratosphere is taken into account. This is a strong piece of evidence that the concentrations of ozone plays a role in affecting the climate in the troposphere.

On the other hand, Keeley [31] also showed that while there is a maximum cooling response in stratosphere during period of maximum ozone depletion, there is a delayed response in the troposphere. The question of whether the coupling between stratosphere and troposphere is purely dynamical, radiative, or a combination of both, is controversial.

Although these are rather different approaches, they strongly suggest that the stratosphere and the troposphere are coupled and ozone appears to play an important role due to its spectral property in the ultraviolet region.

As a side note, these studies also raise concern on the accuracy of numerical weather prediction (NWP), as many NWP centers do not include real-time ozone data in their assimilation systems in order to reduce computational costs [30]. Consequently, the vertical and latitudinal distribution of variation in irradiance could be wrong. With O_3 recognised as one of the major chemicals responsible for climate variability in the last 25 years, NWP from these systems could have been better. Unfortunately, besides hu-

man activities, the interdependence of ozone distribution and stratospheric temperature also make the incorporation of ozone chemistry into existing climate models difficult. Satellite observations have confirmed that stratosphere has cooled due to ozone depletion. However, as the stratosphere cools, ozone-destroying chemical reactions also slow down.

Mechanism

The main mechanism by which the stratosphere and troposphere are coupled is the transport of momentum by mid-latitude baroclinic waves. In a recent study by Simpson, Blackburn & Haigh (hereby after SBH09) [56], it is shown that a change in eddy momentum flux is essential in producing a full response in the troposphere when the stratospheric temperature is perturbed. By considering the zonal mean quasi-geostrophic refractive index, SBH09 showed that the change in zonal wind is initially driven by changes in meridional temperature gradient and eddy momentum fluxes in the lower stratosphere. On the other hand, the eddy momentum flux also changes in response to the altered wind field, which further accelerates the zonal wind. This feedback mechanism between the zonal wind and the eddy momentum flux results in a two-stage acceleration of the zonal wind. The acceleration driven by the feedback of eddy momentum flux, is found to be stronger than that by the change in meridional temperature gradient and eddy momentum flux at the initial stage. This gives a good insight on the mechanism of how troposphere and stratosphere are coupled together.

1.1.2. Atmosphere-Ocean Coupling

To date, simple GCM studies affirmed ST coupling and that the enhanced tropospheric response observed during solar maximum involves O_3 heating, followed by interactions between the stratosphere and the troposphere. However, many of the models used in these studies only assume a slab ocean with a fixed sea surface temperature (SST) profile. This could have a significant effect on the response of the troposphere for the following reasons.

Firstly there is an overwhelming difference in heat capacity in the ocean compared to the atmosphere. Hence, it makes sense that time taken for temperature adjustment in the ocean is much longer. The ocean actually

acts as a buffer and damps atmospheric temperature changes. One strong evidence is that there is a much weaker seasonal cycle in air temperature observed in the Southern Hemisphere, where there are less continents compared to the Northern Hemisphere [48].

The way ocean and atmosphere are coupled is mainly via changes in SST. SST anomalies introduce diabatic heating and cooling in the atmosphere, and subsequently adjusts the circulation in the atmosphere. However, the extent to which the atmosphere and ocean are coupled varies with latitude. For instance, surface winds in the tropical region are strongly controlled by SSTs while a weaker coupling between the atmosphere and ocean is observed at mid-latitudes [18]. Surface water in the tropics is often warm due to excess solar heating and therefore forces air to ascend. The climbing air in this region is often moist as warm air is capable of carrying more water vapour than cold air. Latent heat is constantly released into the atmosphere and hence controlling the tropical atmospheric circulation. In contrast, the ocean-atmosphere coupling at mid-latitudes is not as profound as it is in the tropics. One possible explanation contrasting the coupling in the two regions is that mid-latitude air is cooler and has less water vapour content. As a result, there is less latent heat transferred into the atmosphere and other mechanisms become dominant. It is still an area of intense research and many aspects of the coupling in this region remain controversial.

As will be discussed in more detail in section 1.3.1, surface ($0 \sim 100m$) circulation in the ocean is wind-driven while the water below is buoyancy driven. This implies that the surface winds play a role in spreading equatorial warm water poleward by horizontal advection. More importantly, having the power of driving surface ocean currents, an altered surface wind field has the capability of tilting the thermocline (the layer of ocean in which its temperature and density changes rapidly in depth) and exposing deep cold water to the surface via Ekman pumping (for more details see section 1.3.1).

In other words, a SST anomaly could effectively alter the atmospheric circulation and in return, impose changes on the thermal structure & circulation of the ocean and feedbacks to the SST.

The process of atmosphere and ocean anomalies forcing each other repeats over time, giving rise to a spontaneous oscillation of the Earth's climate system. The El Niño Southern Oscillation (ENSO) is a classic example of atmosphere-ocean coupling. Figure 1.4 shows the time series of the Southern Oscillation Index (SOI) and SST anomaly in the equatorial east Pacific Ocean. The SOI is defined as,

$$SOI = 10 \times \frac{SLP_{Tahiti} - SLP_{Darwin}}{\sigma_{\Delta SLP}} \tag{1.1}$$

where SLP_{Tahiti} and SLP_{Darwin} are the sea level pressure of Tahiti and Darwin(Australia) respectively. $\sigma_{\Delta SLP}$ is the standard deviation of numerator of equation 1.1. It is clear that figure 1.4 shows an anti-correlation between the east Pacific Ocean SST and the SOI, with a period of $2-7$ years in both series [44].

Apart from the feedback via Ekman pumping, there are many other mechanisms that could contribute to the coupling. For example, an altered wind field could have changed the evaporation rates at the surface. In other words, it limits the amount of heat leaving the ocean in the form of latent heat, and have a direct impact on the SST field. On the other hand, a stronger surface stress may have accelerated evaporation, and allow more cumulus clouds to form in the tropics. This also may have a direct radiative effect of reducing solar radiation incident at the sea surface, and hence a drop of SST. However, the interactions are location-specific and there isn't one single rule governing the significance of different atmospheric processes affecting the surface flux. For instance, Seager et al. [53] showed that surface wind anomalies are responsible for surface flux changes over the subtropical North Atlantic while horizontal advection of heat over the sea surface becomes notable north of the basin.

Similarly, it is evident that radiative forcing caused by a change in concentration of greenhouse gases, depending on the magnitude and distribution of applied perturbation, can affect the ocean circulation, and hence the SST indirectly. In a coupled GCM study by Wood et al. [71], the maximum overturning in the ocean is found to drop by 40% at $30°N$ in response to an increase of CO_2 by a factor of two. This is accompanied by a warming

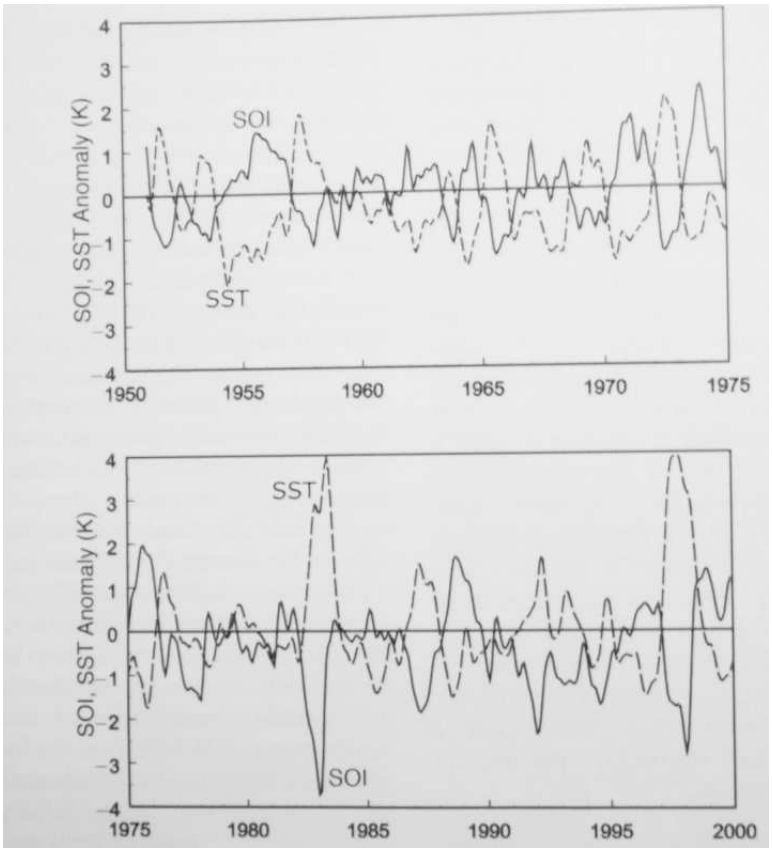


Figure 1.4.: SOI (solid) and SST anomaly [K] in the equatorial east Pacific Ocean (dashed) for period 1951-2000. [44]

of SST by several Kelvin. It is suggested that changes in ocean circulation is responsible for the surface warming. In analogous to CO_2, it is believed that other greenhouse gases such as O_3, will also cause adjustments in the SST and ocean circulation when perturbed. As proposed by Kushnir et al. [34], it is possible that the SST response to atmospheric forcing is capable of inducing adjustments in the jetstreams through a change of eddy momentum flux, analogous to the way the jets responds to a thermal perturbation in the stratosphere.

Atmosphere-ocean coupling is the key to understand many climate variabilities. The air-sea interactions occur on various timescales, ranging from monthly & seasonal timescales which is induced by external forcing, to interannual timescales that arise from positive and negative feedbacks from the atmosphere and ocean. Hence, the inclusion of an interactive ocean might have significant impacts to existing ST coupling studies.

1.1.3. Aim of Study

The objective of this thesis is to employ an atmosphere-ocean coupled general circulation model (AOGCM) and investigate the impact of an interactive ocean in ST coupling studies. As will be covered in more details in section 2.4, the Earth is modelled as a zonally symmetrical aquaplanet in the control run of this study. As a result, the model excludes many of the inter-annual variability observed in the real world such as ENSO and is favourable to our purpose.

After the model has reached equilibrium, stratospheric ozone is increased by five times and the climate anomalies are analysed. In order to address the impact of the interactive ocean, the experiment is repeated with the ocean coupling turned off. By doing so, this thesis attempts to answer the following questions:

- How does the ocean respond to an increased amount of ozone in the stratosphere?
- What difference, in terms of common diagnostic fields such as zonal wind and temperature, does an interactive ocean make in such an ozone perturbation study?

- Is the mechanism described in SBH09 still valid in explaining ST coupling in an AOGCM?

This chapter continues by going through the physical background of both the atmosphere and the ocean. The derivation of equations used in the thesis will also be presented.

1.2. Atmosphere

1.2.1. Chemical composition

The major source of energy which makes the Earth habitable comes from radiation of the Sun. The incoming solar radiation arriving at the Earth is either scattered, absorbed, or reflected by various components in the atmosphere, which includes different gases, aerosols and clouds. A majority of the radiation which happens to reach the surface is absorbed by the ocean, land and biomass. The absorbed solar energy will either be re-emitted into space or take the form of heat energy and subsequently be converted into other forms of energy (such as kinetic and potential) until the Earth reaches an equilibrium state.

The Earth's atmosphere is composed of different gases, with nitrogen (N_2) and oxygen (O_2) as the dominant species. Water vapour (H_2O), which is a strong absorber of radiation at various wavelength ranges, accounts for approximately 5% of the mass of the atmosphere. Its concentration is highly variable, ranging from $0-5\%$ by volume [65]. The concentration of carbon dioxide (CO_2), which is also a strong absorber of long wave radiation in the atmosphere, is highly dependent on human activities such as deforestation and fossil fuel combustion. Both CO_2 and H_2O are relatively transparent to shortwave solar radiation but opaque in the longwave end of the spectrum. Therefore they will absorb outgoing longwave terrestrial radiation and are responsible for heating of the atmosphere. These gases are referred to as greenhouse gases.

Ozone (O_3), which is a strong absorber of shortwave radiation, is also a greenhouse gas. The creation of (O_3) first involves photodissociation of O_2 molecules into two atomic oxygens. The atomic oxygen then reacts, with the

help of a third body (usually N_2 or O_2) to conserve energy and momentum, with molecular oxygen to form O_3. The excess energy is deposited in the third body, in the form of thermal energy. On the other hand, upon absorption of ultraviolet radiation, O_3 is broken down into O_2 and atomic oxygen. The time constant for these two reactions are short (former is dependent on the abundance of N_2 & O_2 at different altitudes and varies from a few seconds at $40km$ to $\sim$ 100s at $50km$ [65]) and therefore heat is constantly deposited in the ozone-rich stratosphere. O_3 is removed either by photodissociation or the aid of catalytic chemical cycles. Candidates responsible for catalysing the destruction of O_3 includes OH, NO, Cl and Br. One of the major concerns over the last 30 years is the depletion of O_3 in the South Hemisphere. This is mainly due to the increased use of chlorofluorocarbons (CFCs), which will be dissociated into Cl atoms by UV radiation.

Due to the spectral properties of the gases in the atmosphere, the atmosphere has a temperature profile which can be categorised into four sections and is shown in figure 1.5.

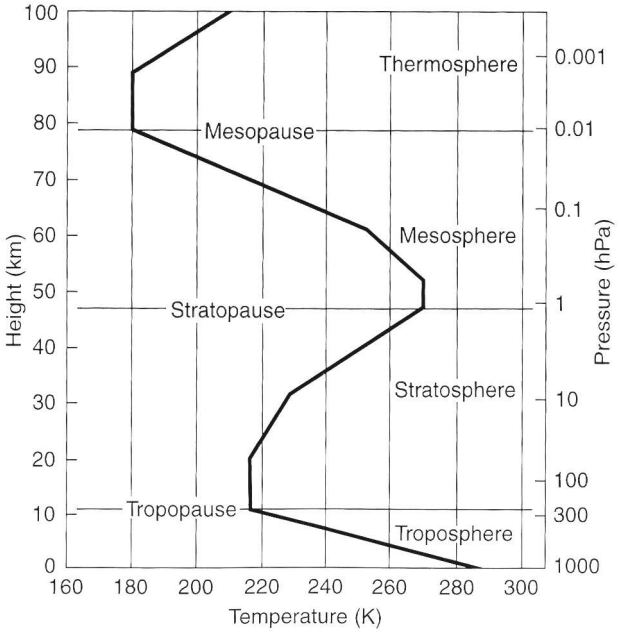


Figure 1.5.: A typical mid-latitude vertical temperature profile [65]

As air parcels ascend from the surface, they experience less pressure from the surrounding and therefore expands. The adiabatic expansion is accompanied by a drop of temperature. As a result, assuming the air parcel remains unsaturated, the temperature in the troposphere decreases with respect to altitude, at an average lapse rate of $\frac{g}{c_{pa}} K km^{-1}$, where g is the gravitational constant and c_{pa} is specific heat of air at constant pressure. In the ozone-rich stratosphere, temperature increases with height due to the absorption of ultraviolet radiation and vertical mixing is strongly inhibited. Although there are a variety of ways to define the tropopause [61], at this stage, it is sufficient to consider the altitude at which the temperature starts to invert with height as the tropopause.

Above the stratosphere, temperature decreases with altitude again and this region is known as the mesosphere. Higher up in the atmosphere lies the thermosphere, in which absorption of UV results in photodissociation of N_2 & O_2 and ionisation of atoms. As a result, the thermosphere is another region where temperature inversion is observed.

1.2.2. General Circulation

Solar radiation is a function of latitude, which peaks at the equator and decreases towards the poles (see figure 1.6). In contrast, the outgoing radiation does not directly depend on latitude and other variables such as clouds, dust, greenhouse gases and temperature become the determinant of its spatial distribution. Local radiation equilibrium would require the solar radiation to be balanced by the Earth's infrared radiation, which implies much higher temperature at the equator than at the poles. However this would not be dynamically stable and therefore heat is transported poleward, resulting in a temperature structure that is locally different from radiative equilibrium, although a global balance is established.

Excessive heating at the equator gives rise to an expansion of air, which implies vertical displacements of pressure surfaces. The equator-pole pressure gradient results in a poleward flow of air at the upper troposphere. As

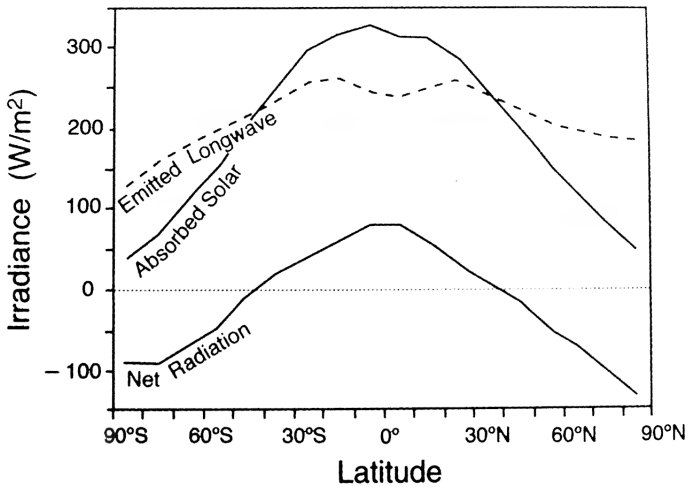


Figure 1.6.: Annual mean absorbed solar radiation, emitted long-wave radiation, and net radiation. [44]

the warm air from the equator reaches the pole it loses heat to the surroundings and sinks to the bottom, creating a high surface pressure compared to that at the equator. This drives an equatorward flow of air at the surface as a compensation to that at the upper levels. At low levels, the winds are not as strong as in the upper troposphere, due to surface friction by topography. Coriolis force requires that the upper branch of the cell to be deflected to the east while the lower branch to the west. Instead of having a purely symmetric Hadley cell that extends from the equator all the way to polar latitudes, the poleward flow of air halts at about 30° and horizontal circulations, known as the subtropical jet stream, takes over due to Earth's rotation. This type of circulation is referred to as the Hadley circulation.

The poleward flow of air from the tropics do not stop entirely at the subtropics. However, the meridional circulation becomes much weaker as it reaches middle latitudes and one would expect the poleward transport of heat and momentum is not as efficient as it is at lower latitudes. As the equator-pole temperature gradient steepens, the zonal thermal wind strengthens and at some point it becomes baroclinically unstable. Hence, baroclinic waves develop in middle latitudes.

At the tropics, surface easterlies prevail and the atmosphere gain westerly momentum from the Earth by surface friction. In contrast, westerly momentum in the atmosphere is lost to the Earth in the mid-latitudes where surface winds are directed to the east. Hence westerly momentum must be transported poleward from the tropics in order to conserve the momentum of the atmosphere. Therefore, in addition to poleward heat transfer, the baroclinic waves described previously are also responsible for maintaining the Earth's momentum budget by transporting westerly momentum poleward.

For quasi-geostrophic flow a poleward transport of momentum requires the waves to tilt in the southwest-northeast (northwest-southeast) direction in the northern (southern) hemisphere [26]. A schematic is shown in figure 1.7. At mid-latitudes the eddy transport of heat and momentum gets strong enough to drive a meridional circulation that is in opposite sense to that of the Hadley cell [26]. This 'thermally-indirect' cell is called the Ferrel cell.

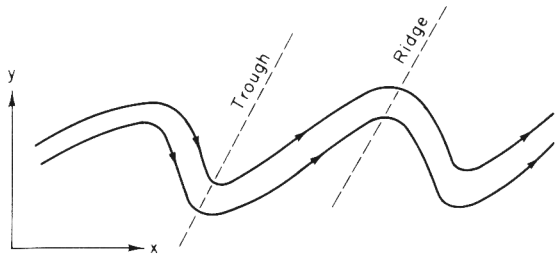


Figure 1.7.: Schematic streamlines for a positive eddy momentum flux. The x- and y-axis denotes eastward and northward directions. [26]

The mid-latitude eddies act to reduce the equator-to-pole temperature gradient in the atmosphere. In response to the transfer of westerly momentum at mid-latitudes, the Coriolis-induced easterlies at the surface becomes westerlies. Figure 1.8 shows a schematic of the form of general circulations on Earth and the locations of the jet streams.

Another powerful jet stream, known as the polar night jet exists in high-latitude stratosphere during winter seasons. During solstice the air over the winter pole is much colder than that at the tropics, and hence creating

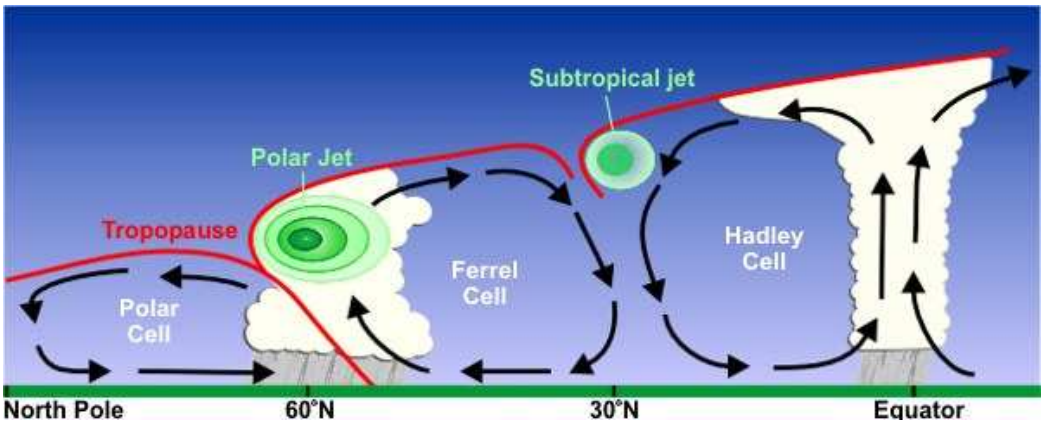


Figure 1.8.: Schematic of locations of jet streams and the general circulation pattern (Taken from NOAA National Weather Service webpage)

a considerable temperature gradient. This temperature gradient results in a substantial pressure gradient which combines with the Coriolis effects to form a jet stream. The highest wind speeds recorded are often located at the boundary of the polar night jet, which also prevents warmer air from the tropics to enter the vortex. Throughout the winter and sometimes extended into spring, the cold air in the vortex, together with other chemicals like ozone, remained trapped inside. The breakdown of this vortex can sometimes cause abrupt rise of stratospheric temperature, and is known as stratospheric sudden warming.

1.2.3. The Stratosphere-Troposphere System

ST coupling has become an active research area and has provided some understanding to climate dependance on solar variability. The traditional way of distinguishing the two from one another is by looking at the lapse rate. Referring to figure 1.5, the gradient switches sign at about 10 km as one ascends from the surface, indicating a change in chemical structure.

There are various definitions of the tropopause, which is the boundary between the troposphere and stratosphere as introduced previously. These including changes in lapse rate, potential vorticity [25] and chemical composition [4]. As one might have expected, the tropopause height depends

on the vertical distribution of O_3 in the stratosphere. It was indeed shown by Thuburn [61] that the tropopause height is sensitive to non-IR (infrared) heating, with an estimated value of a few kilometers per $Kday^{-1}$. As summarised by Shepherd [55], there are various ways in which this region affect the climate. The local minimum in temperature at the tropopause controls the amount of water vapour, which is a source of OH^-, entering the stratosphere via condensation. Since OH^- is a suitable candidate for catalysing the destruction of ozone, the freeze-drying mechanism at the tropopause has an indirect control over the abundance of ozone in the stratosphere.

Consider a column of air with temperature T. As T increases, the air expands and hence the column of air is physically thicker than cold air. In the atmosphere, excess solar heating at the tropics causes surfaces of constant pressure to tilt towards the poles. A simplified schematic is shown in figure 1.9. Since the pressure at point B is higher than that at point A, air is driven towards the poles by the pressure gradient force, which is subsequently deflected to the east by the Coriolis force. Hence, changes in latitudinal temperature gradient of the region around the tropopause can induce zonal winds anomalies. This is known as thermal wind balance.

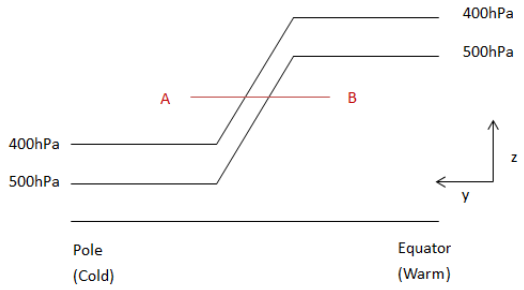


Figure 1.9.: Simplified schematic illustrating the thermal wind relationship.

One other reason why the tropopause region is important to climate is because of mixing of chemical species. As will be discussed more in detail in section 1.2.3, drag by wave from the troposphere drives an equator-to-pole circulation in the stratosphere, which determines the spatial distribution of O_3 above the tropopause.

The Troposphere

Due to excessive solar heating at the equator, convection dominates in the tropics. The consequential general circulation pattern was covered in section 1.2.2. Transport is generally faster in the troposphere and therefore timescales only vary from hours (convective processes) to days (baroclinic transport). In terms of heat budget, at lower latitudes, the Hadley circulation induces adiabatic cooling and heating at the upwelling and downwelling branch of the cell, and is balanced by radiation. Poleward of the Hadley cell, the heat budget is dominated by eddy heat transport.

The Stratosphere

The stratosphere, as the name suggests, is a stratified layer in which vertical motion of air is inhibited. As shown in figure 1.5, temperature increases with height due to UV absorption by O_3, making it a very stable place where air does not overturn due to buoyancy. Nevertheless, the air in the stratosphere do circulate, in a much slower fashion than in the troposphere, and is known as the Brewer-Dobson circulation. A schematic of the Brewer-Dobson circulation is shown in figure 1.10. This circulation is driven by planetary waves in the troposphere below, and involves upwelling of dry air from the troposphere at the tropics, and meridional transport to middle & polar latitudes where air descends back into the troposphere. Apart from a change of sign in temperature lapse rate, the buoyancy frequency also changes abruptly across the tropopause. The buoyancy frequency is one of the dominant contributors of confining planetary waves in the troposphere at high latitudes [8]. In other words, at high latitudes, the distribution of O_3 will affect the propagation of tropospheric waves into the lower stratosphere, and hence plays an important role in the stratosphere-troposphere coupling.

Regarding timescales, chemicals generally have long lifetime in the stratosphere. For example, O_3-destroying CFCs, which originate from the troposphere, accumulate in the stratosphere due to the inhibited vertical motion and slow meridional transport.

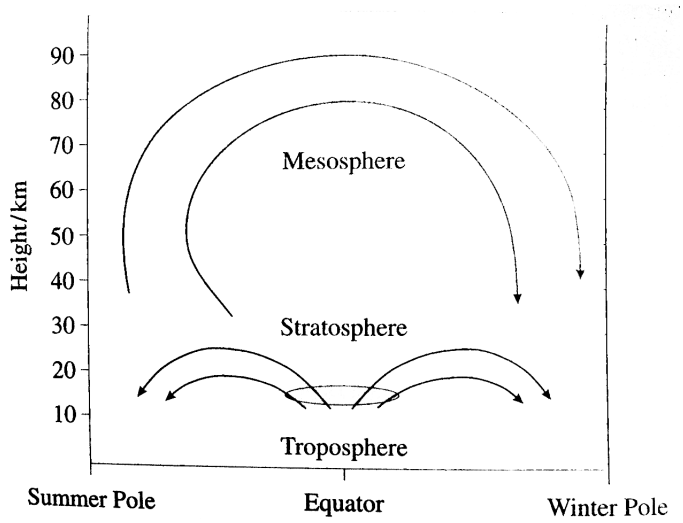


Figure 1.10.: Schematic of Brewer-Dobson circulation (Bottom arrows) and the solstitial middle atmosphere circulation (Top arrows) [1]

1.2.4. Equation of motion

The equations of motion of the atmosphere can be deduced from Newton's second of law for a unit mass,

$$\frac{d\vec{U_A}}{dt} = \sum \vec{F} \tag{1.2}$$

which states that the rate of change of its absolute velocity $\vec{U_A}$ as viewed from an inertial frame is equal to the sum of forces acting on it.

If one assumes the only forces acting on the atmosphere are the pressure gradient force, gravity and friction, equation 1.2 could be rewritten as:

$$\frac{d\vec{U_r}}{dt} = -2\vec{\Omega} \times \vec{U_r} - \frac{1}{\rho_a}\nabla p + g + \vec{F}_{Friction} \tag{1.3}$$

where $\vec{U_r}$ is the velocity measured in the rotating frame, ρ_a is the density of air, p is the pressure, g is the sum of gravitational force & centrifugal force $\Omega^2\vec{R}$ and $\vec{F}_{Friction}$ is the frictional force (see Appendix A.1 for derivation).

Since we are interested in dynamics on the Earth, which could be assumed

to be a sphere, it is convenient to adopt a spherical-pressure coordinate system in which longitude (λ), latitude (ϕ) and height above surface of Earth (z) are the primary coordinate axes. The components of $\vec{U_r}$ in the new coordinate system are defined as follows:

$$u = \vec{U}_\lambda = R\cos\phi\frac{d\lambda}{dt} \tag{1.4}$$

$$v = \vec{U}_\phi = R\frac{d\phi}{dt} \tag{1.5}$$

$$w = \vec{U}_z = \frac{dz}{dt} \tag{1.6}$$

where R is the mean radius of the Earth.

In this thesis we are interested in the change in zonal flow, particularly in mid-latitudes, in response to stratospheric ozone perturbation. Therefore, following the derivation as described in [26], we apply the above coordinate transformation to equation 1.3 and expanding only the λ component, which yields,

$$\frac{du}{dt} = \frac{\tan\phi}{R}uv - \frac{uw}{R} + fv - f'w - \frac{1}{\rho_a}\frac{\partial p}{R\cos\phi\partial\lambda} + F_\lambda \tag{1.7}$$

where $f = 2\Omega\sin\phi$, $f' = 2\Omega\cos\phi$ and F_λ is the frictional force in zonal direction.

Terms	$\frac{du}{dt}$	$\frac{\tan\phi}{R}uv$	$\frac{uw}{R}$	fv	$f'w$	$\frac{1}{\rho_a}\frac{\partial p}{R\cos\phi\partial\lambda}$
Magnitude in ms^{-2}	10^{-4}	10^{-5}	10^{-8}	10^{-3}	10^{-6}	10^{-3}

Table 1.1.: Scale analysis of the zonal momentum equation

Table 1.1 shows the typical magnitude of the terms involved in the zonal momentum equation for the atmosphere. For general circulation studies, we apply a threshold of $10^{-5}ms^{-2}$ and drop the smaller terms, namely $\frac{uw}{R}$ and $f'w$. Hence equation 1.7 becomes,

$$\frac{du}{dt} = \frac{\tan\phi}{R}uv + fv - \frac{1}{\rho_a}\frac{\partial p}{R\cos\phi\partial\lambda} + F_{Friction} \tag{1.8}$$

where

$$\frac{d}{dt} = \frac{\partial}{\partial t} + u\frac{\partial}{R\cos\phi\partial\lambda} + v\frac{\partial}{R\partial\phi} + \omega\frac{\partial}{\partial p} \tag{1.9}$$

and $\omega = \frac{dp}{dt}$.

Using the continuity equation in spherical-pressure coordinate, i.e.,

$$\frac{\partial u}{R\cos\phi\partial\lambda} + \frac{\partial v\cos\phi}{R\cos\phi\partial\phi} + \frac{\partial\omega}{\partial p} = 0 \tag{1.10}$$

we can write equation 1.8 in 'flux form' which is more convenient for analysis on eddy momentum fluxes. Adding $u\times$(1.10) to (1.8) yields,

$$\begin{aligned}&\frac{\partial u}{\partial t} + \frac{u\partial u}{R\cos\phi\partial\phi} + \frac{v\partial u}{R\partial\phi} + \frac{\omega\partial u}{\partial p} + u\left[\frac{\partial u}{R\cos\phi\partial\lambda} + \frac{\partial v\cos\phi}{R\cos\phi\partial\phi} + \frac{\partial\omega}{\partial p}\right]\\ &= \tan\phi\frac{uv}{R} + fv - \frac{g\partial z}{R\cos\phi\partial\lambda} + F_\lambda\end{aligned} \tag{1.11}$$

Differentiating the term $\frac{\partial v\cos\phi}{R\cos\phi\partial\phi}$ by chain rule and collecting terms,

$$\begin{aligned}&\frac{\partial u}{\partial t} + \frac{2u\partial u}{R\cos\phi\partial\lambda} + \frac{\omega\partial u}{\partial p} + \frac{u\partial\omega}{\partial p} + \frac{u\cos\phi\partial v}{R\cos\phi\partial\phi} - \frac{2uv\sin\phi}{R\cos\phi} + \frac{v\partial u}{R\partial\phi}\\ &= fv - \frac{g\partial z}{R\cos\phi\partial\lambda} + F_\lambda\end{aligned} \tag{1.12}$$

By inspection the two terms containing ω in equation 1.12 simplifies to a single term $\frac{\partial u\omega}{\partial p}$. Together with factorisation of the 3rd, 4th and 5th term on the left hand side we have,

$$\begin{aligned}&\frac{\partial u}{\partial t} + \frac{2u\partial u}{R\cos\phi\partial\lambda} + \frac{\partial u\omega}{\partial p} + \frac{1}{R\cos^2\phi}\left[\frac{u\cos^2\phi\partial v}{\partial\phi} - 2uv\sin\phi\cos\phi + \frac{v\cos^2\phi\partial u}{\partial\phi}\right]\\ &= fv - \frac{g\partial z}{R\cos\phi\partial\lambda} + F_\lambda\end{aligned} \tag{1.13}$$

Taking note that the terms in the square bracket simplifies to $\frac{1}{R\cos^2\phi}\frac{\partial uv\cos^2\phi}{\partial\phi}$, the zonal momentum equation can be written in its 'flux form', as shown in

equation 1.14.

$$\frac{\partial u}{\partial t}+\frac{2u\partial u}{R\cos\phi\partial\lambda}+\frac{1}{R\cos^2\phi}\frac{\partial uv\cos^2\phi}{\partial\phi}+\frac{\partial u\omega}{\partial p}=fv-\frac{g\partial z}{R\cos\phi\partial\lambda}+F_\lambda \quad (1.14)$$

Fields such as wind velocity are not necessarily uniform in space. As we are most interested in the changes in location and magnitude of the mid-latitude jetstream in response to ozone forcing, it is useful to breakdown the wind velocities u, v and ω into their zonal-mean and eddy components, for example in the case of u,

$$u=[u]+u^* \quad (1.15)$$

and similar expressions for v and ω. [ ] denotes the zonal average operator such that $[A]=\frac{1}{2\pi}\int_0^{2\pi}Ad\lambda$ and * represents the departure from its zonal mean. It follows that $[A^*]=0$ and $[[A]]=[A]$.

Now apply the expansion as in equation 1.15 to equation 1.14 and take the zonal average again so that all the terms involving $\frac{\partial}{\partial\lambda}$ vanishes,

$$\begin{aligned}&\frac{\partial[u]}{\partial t}+\frac{1}{R\cos^2\phi}\frac{\partial\big[([u]+u^*)([v]+v^*)\big]\cos^2\phi}{\partial\phi}+\frac{\partial\big[([u]+u^*)([\omega]+\omega^*)\big]}{\partial p}\\&=f[v]+[F_\lambda]\end{aligned} \quad (1.16)$$

and expanding and rearranging the terms in equation 1.16,

$$\begin{aligned}\frac{\partial[u]}{\partial t}=&-\frac{1}{R\cos^2\phi}\frac{\partial[u][v]\cos^2\phi}{\partial\phi}-\frac{\partial[u][\omega]}{\partial p}-\frac{1}{R\cos^2\phi}\frac{\partial[u^*v^*]\cos^2\phi}{\partial\phi}-\frac{\partial[u^*\omega^*]}{\partial p}\\&+f[v]+[F_\lambda]\end{aligned} \quad (1.17)$$

Finally, making the assumption that terms involving ω are small and can be neglected, equation 1.17 becomes,

$$\frac{\partial[u]}{\partial t}=-\frac{1}{R\cos^2\phi}\frac{\partial[u][v]\cos^2\phi}{\partial\phi}-\frac{1}{R\cos^2\phi}\frac{\partial[u^*v^*]\cos^2\phi}{\partial\phi}+f[v]+[F_\lambda] \quad (1.18)$$

The first and second terms represent contributions to the acceleration of zonal-mean zonal wind field by zonal mean flow and stationary eddies. In

chapter 4, these terms will be analysed in an attempt to diagnose the change in zonal wind velocity upon ozone forcing.

1.2.5. Energy Budget

Consider a parcel of air of unit mass so that $\rho V = 1$, where ρ and V is the density and the volume of the parcel respectively. The first law of thermodynamics states that the change in internal energy dU of the air parcel is related to the difference of amount of heat dQ brought into the system and the work done by the parcel on its surrounding by expansion, as shown in equation 1.19.

$$dU = dQ - dW \tag{1.19}$$

where

$$dU = c_{va} dT \tag{1.20}$$

$$dW = pdV \tag{1.21}$$

Here dT and dV is the change of temperature and volume of the parcel respectively. c_{va} is the specific heat of air at constant volume and p is the pressure at which the parcel undergoes expansion. Substituting equations 1.20 and 1.21, equation 1.19 becomes

$$dQ = c_{va} dT + pdV \tag{1.22}$$

Recalling that $\rho_a V = 1$, a change of variable in equation 1.22 yields

$$dQ = c_{va} dT - \frac{p}{\rho^2} d\rho \tag{1.23}$$

Differentiating the ideal gas law, as shown in equation 1.24,

$$p = \rho R_a T \tag{1.24}$$

gives

$$dp = R_a T d\rho + \rho R_a dT \tag{1.25}$$

where R_a is the specific gas constant of air and other symbols have previously been defined. By re-writting equation 1.25, we get

$$d\rho = \frac{dp - \rho R_a dT}{R_a T} \tag{1.26}$$

Substituting equation 1.26 back into 1.23 yields equation 1.27,

$$dQ = c_{pa} dT - \frac{dp}{\rho} \tag{1.27}$$

where $c_{pa} = R_a + c_{va}$ and is the specific heat of air under constant pressure.

In order to convert equation 1.27 to a more convenient form, we make use of the equation of hydrostatic balance (for derivation see Appendix A.2):

$$\frac{dp(z)}{dz} = -\rho g \tag{1.28}$$

Substitute equation 1.28 into 1.27, and writing the latent heat involved in evaporation and precipitation of water as $dQ = -L_v dq$, equation 1.27 becomes [44],

$$d(c_{pa}T + gz + L_v q) = 0 \tag{1.29}$$

or, when integrated over a fixed volume $dx \times dy \times dz$,

$$H_a = \iiint \rho_a \big(c_{pa}T + gz + L_v q\big) dx dy dz \tag{1.30}$$

where ρ_a is the density of air, c_{pa} is specific heat of air at constant volume, T is atmospheric temperature, g is gravitational constant, z is height from some reference level, L_v is the latent heat of vaporisation, q is the water vapour mixing ratio in air. H_a is the moist static energy of the atmosphere and is an useful quantity as it allows one to monitor the amount of energy present at a particular volume of the atmosphere.

The three terms on the right hand side of equation 1.30 represent internal energy, potential energy and latent heat respectively. The magnitude of kinetic energy is small compared to these three terms and is usually neglected when considering the heat budget.

1.3. Ocean

1.3.1. General Circulation

The ocean plays an equally important role in characterising the Earth's climate. Unlike the atmosphere, water is incompressible, has a low albedo and is bounded by continents, which allows unique features to be observed in the ocean. For example, the latter gives rise to east-west asymmetrical subtropical gyres in which intense boundary currents are observed at the west rather than the east side of the gyre.

The circulation in the ocean is mainly driven by two processes. The current at the surface layer is driven by the surface windstress and its curl, which impart momentum and vorticity to the ocean. The circulation below is forced by buoyancy loss at polar latitudes, caused by changes in sea water temperature and salinity.

Wind-driven circulation

The surface layer, known as the Ekman layer, is usually 50-100 meters deep. It is in direct contact with the atmosphere and is therefore more responsive to atmospheric forcing than the interior of the ocean. The horizontal transport of mass, is given by equation (1.31)

$$\vec{m}_{ek} = \frac{\vec{\tau} \times \hat{z}}{f} \tag{1.31}$$

where $\vec{\tau}$ is the surface wind stress in Nm^{-2}, f is the Coriolis parameter, $\hat{z}$ is a unit vector pointing vertically upwards. $\vec{m}_{ek}$ is the lateral transport mass transport given by (1.32) where ρ is the density of the layer, $\vec{U}_{ek}$ is the wind-driven Ekman current and D is the depth of the layer over which turbulence transfers momentum downward.

$$\vec{m}_{ek} = \int_{-D}^{0} \rho \vec{U}_{ek} dz \tag{1.32}$$

Equation 1.31 shows that a surface wind stress will drive a current in the ocean and its direction will always point to the right of the surface wind field. Although the magnitude of the wind-driven current is small compared

to that of the wind in the atmosphere ($\approx 10 cms^{-1}$), it plays an important role in meridional currents and has a significant impact to SST and sea surface height. Consider an ocean in the Northern Hemisphere where there is a horizontal wind shear over its surface. Equation 1.31 states that the wind-induced transport of mass in the ocean will always be to the right and at right angle of the surface stress. It follows that there will either be a convergence or divergence of water, depending on the orientation of the wind shear. Note that by neglecting evaporation and precipitation, the mass flux flowing across the surface is zero which means that water mass cannot escape into the atmosphere. On the other hand, sea water is incompressible and therefore water cannot accumulate (deplete) at the site of convergence (divergence). As a result, depending on the situation, water is either forced down into or pumped up from the interior of the ocean. This is known as Ekman pumping and figure 1.11 shows the meridional positions of upwelling and downwelling of sea water and their relations to the direction of the surface winds.

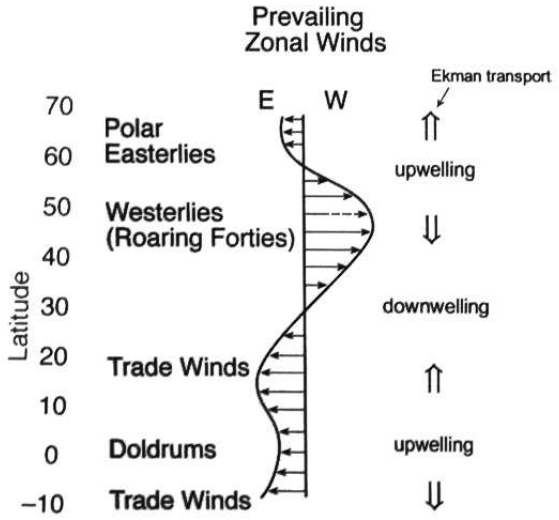


Figure 1.11.: Schematic showing relative positions of surface winds and Ekman transport [44]

Thermohaline circulation

Unlike the wind-driven circulation, circulation below the mixed layer, is driven by density gradients. Since sea water density is a function temperature and salinity, this type of circulation is known as the thermohaline circulation. The changes in sea temperature and salinity, can be initiated from surface conditions anomaly. For instance, a strong windstress anomaly over the ocean will induce a higher rate of evaporation. Hence, more ocean heat content is lost to the atmosphere by latent heat flux and sea water becomes colder and denser. On the other hand, sea water at the poles are more saline than that at the tropics due to lack of rainfall. When ocean water gets sufficiently dense, it sinks to the bottom of the ocean. In contrast to wind-driven circulations, thermohaline circulation vary very slowly and its time scale is of order of hundreds of years, which makes it difficult to measure and monitor. As a result, the thermohaline circulation is still poorly understood. On the other hand, measurement shows that the return of deep water does not necessarily occur at the warmer part of the ocean as one would expect [62]. In fact, studies suggest that the upwelling of deep water could be partly wind-driven [62, 72].

Although both wind-driven and buoyancy-driven circulations play an important role in real world scenario, it is found that the thermohaline circulation is absent in an aquaplanet model and the meridional overturning circulation in the ocean is mainly wind-driven [42].

1.3.2. Energy Budget

The ocean is a major sink of energy due to its enormous heat capacity. As in the atmosphere, kinetic energy is neglected in the energy budget of ocean. Following the procedures as described in [66], the internal energy of the ocean U_o can be represented by a set of thermodynamic coordinates (T, S, p), where T is temperature, S is salinity and p is pressure. We can the write the derivative of U_o as,

$$dU_o = \left(\frac{\partial U_o}{\partial T}\right)_{S,p} dT + \left(\frac{\partial U_o}{\partial S}\right)_{T,p} dS + \left(\frac{\partial U_o}{\partial p}\right)_{T,S} dp \tag{1.33}$$

In order to further expand each of the terms equation 1.33, let us write the internal energy U_o in terms of the enthalpy H, pressure p and volume V.

$$U_o = H - pV \tag{1.34}$$

$$dU_o = dH - pdV - Vdp \tag{1.35}$$

Partial differentiation with respect to T and p gives,

$$\left(\frac{\partial U_o}{\partial T}\right)_{S,p} = \left(\frac{\partial H}{\partial T}\right)_{S,p} - p\left(\frac{\partial V}{\partial T}\right)_{S,p} = c_{pw} - p\left(\frac{\partial V}{\partial T}\right)_{S,p} \tag{1.36}$$

$$\left(\frac{\partial U_o}{\partial p}\right)_{T,S} = \left(\frac{\partial H}{\partial p}\right)_{T,S} - p\left(\frac{\partial V}{\partial p}\right)_{T,S} - V \tag{1.37}$$

where c_{pw} is the specific heat capacity of sea water. To further simplify equation 1.37, let us consider the second law of thermodynamics, which states that the entropy of any system is given by,

$$d\eta = \frac{dQ}{T} \tag{1.38}$$

where dQ is the transfer of heat into the system. According to the first law of thermodynamics, a change in internal energy dU of a system is caused by a sum of heat dQ into the system and work done dW by the system, i.e.,

$$dU_o = dQ - dW = dQ - pdV \tag{1.39}$$

where dV is the change of volume of the system. Substituting equation 1.35 into equation 1.39 gives,

$$dH = dQ + Vdp \tag{1.40}$$

Now substitute equation 1.40 into equation 1.38, which yields,

$$d\eta = \frac{1}{T}dH - \frac{V}{T}dp - \frac{\mu}{T}dS \tag{1.41}$$

Note the third term is added to account for the entropy change due to change in salinity and μ is the effective chemical potential for salinity. In order to write equation 1.41 in terms of our chosen set of thermodynamics coordinate (T,S,p), we expand equation 1.34 by writing out its partial derivatives and

substitute into 1.41 such that,

$$d\eta = \frac{c_{po}}{T}dT + \frac{1}{T}\left[\left(\frac{\partial H}{\partial S}\right)_{T,p} - \mu\right]dS + \frac{1}{T}\left[\left(\frac{\partial H}{\partial p}\right)_{T,S} - V\right]dp \quad (1.42)$$

where $c_{po} = \left(\frac{\partial H}{\partial T}\right)_{S,p}$.

Since $d\eta$ is an exact differential, we know that the p derivative of the coefficient of dT is equal to T derivative of the coefficient of dP. With reference to equation 1.42, we write,

$$\frac{\partial}{\partial p}\left[\frac{1}{T}\left(\frac{\partial H}{\partial T}\right)_{S,p}\right]_{T,S} = \frac{\partial}{\partial T}\left\{\frac{1}{T}\left[\left(\frac{\partial H}{\partial p}\right)_{T,S} - V\right]\right\}_{S,p} \quad (1.43)$$

Differentiating equation 1.43 using the product rule gives,

$$\frac{1}{T}\frac{\partial}{\partial p}\left[\left(\frac{\partial H}{\partial T}\right)_{S,p}\right]_{T,S} = -\frac{1}{T^2}\left[\left(\frac{\partial H}{\partial p}\right)_{T,S} - V\right] + \frac{1}{T}\frac{\partial}{\partial T}\left[\left(\frac{\partial H}{\partial p}\right)_{T,S}\right]_{S,p} - \frac{1}{T}\left(\frac{\partial V}{\partial T}\right)_{S,p} \quad (1.44)$$

The second term on the right hand side of equation 1.44 cancels with the left hand side, hence,

$$\left(\frac{\partial H}{\partial p}\right)_{T,S} = V - T\left(\frac{\partial V}{\partial T}\right)_{S,p} \quad (1.45)$$

Finally we substitute equation 1.36, 1.37 and 1.45 into 1.33 to get,

$$dU_o = \left[c_{po} - p\left(\frac{\partial V}{\partial T}\right)_{S,p}\right]dT - \left[T\left(\frac{\partial V}{\partial T}\right)_{S,p} + p\left(\frac{\partial V}{\partial p}\right)_{T,S}\right]dp + \left(\frac{\partial U}{\partial S}\right)_{T,p}dS \quad (1.46)$$

In the following we continue to follow the method as described in [66] to get an approximation of the ocean heat content, which involves integrating equation 1.46 from a reference state $U_0(T_0 = 0K, S_0 = 35psu, p_0)$ to an arbitrary state $U_1(T_1, S_1, p_1)$. The integration is a three-step-process:

1. Integrating from $(T_0, 35, p_0)$ to (T_0, S_1, p_0)

$$\int dU_o = \int_{35}^{S_1}\left(\frac{\partial U}{\partial S}\right)dS \approx \left(\frac{\partial U}{\partial S}\right)_{T,p}\Big|_{S=35}(S_1 - 35) \quad (1.47)$$

According to [66], the above approximation is valid because the $\frac{\partial U}{\partial S}_{T,p}$ varies by 7% over the typical salinity range $33 - 37psu$ [11].

2. Integrating from (T_0, S_1, p_0) to (θ_1, S_1, p_0), where θ_1 is the potential temperature with reference to the surface pressure p_0.

$$\int dU_o \approx \int_0^{\theta_1} c_{po} dT \approx \overline{c_{po}}\theta_1 \tag{1.48}$$

As noted by [66], $p\left(\frac{\partial V}{\partial T}_{S,p}\right)$ is negligible compared to c_{po} and is therefore omitted in the above approximation. In addition, as the variation of c_{po} is negligible under typical ocean conditions, c_{po} is approximated by the averaging the specific heats over the concerned temperature limits ($\overline{c_{po}}$).

3. Integrating from (θ_1, S_1, p_0) to (T_1, S_1, p_1).

$$\begin{aligned}\int dU_o = &\int_{\theta_1}^{T_1} c_{po} dT - \int_{\theta_1}^{T_1} p\left(\frac{\partial V}{\partial T}\right)_{S,p} dT \\ &- \int_{p_0}^{p_1} T\left(\frac{\partial V}{\partial T}\right)_{S,p} dp - \int_{p_0}^{p_1} p\left(\frac{\partial V}{\partial p}\right)_{T,S} dp\end{aligned} \tag{1.49}$$

Since this integration is on the adiabat in the S_1 plane, both $d\eta$ and $dS = 0$, differentiating equation 1.42 with respect to dP gives,

$$\frac{dT}{dp} = \frac{T}{c_{po}}\left(\frac{\partial V}{\partial T}\right) \tag{1.50}$$

Using equation 1.50, the first and third terms in equation 1.49 cancels each other and the rest of the terms reduces to,

$$\begin{aligned}\int dU_o &= -\int_{\theta_1}^{T_1} p\left(\frac{\partial V}{\partial T}\right)_{S,p} dT - \int_{p_0}^{p_1} p\left(\frac{\partial V}{\partial p}\right)_{T,S} dp \\ &= -\int_{p_0}^{p_1} p\left[\frac{T}{c_{po}}\left(\frac{\partial V}{\partial T}\right)^2_{S,p} + \left(\frac{\partial V}{\partial p}\right)_{T,S}\right] dp\end{aligned} \tag{1.51}$$

The first term on the right hand side of equation 1.51 is only 2% of the second [66] and can be neglected. Hence, equation 1.51 reduces to,

$$\int dU_o = -\int_{p_0}^{p_1} p\left(\frac{\partial V}{\partial p}\right)_{T,S} dp \tag{1.52}$$

Combining the results from the above integration steps, we have an approximate expression for the internal energy of the ocean, related to that of the chosen reference state as mentioned earlier.

$$U_{o1} - U_{o0} \approx \overline{c_{po}}\theta_1 + \left(\frac{\partial U}{\partial S}\right)_{T,p}(S_1 - 35) - \int_{p_0}^{p_1} p\left(\frac{\partial V}{\partial p}\right)_{T,S} dp \qquad (1.53)$$

Using typical values for the variables in equation 1.53, Warren [66] showed that the second and third terms are negligible compared to c_{po} (0.3% and 3% respectively). Hence, for a finite volume $dx \times dy \times dz$ of ocean, its internal energy U_o can be approximated by,

$$U_o \approx \iiint \rho_o c_{po} \theta dx dy dz \qquad (1.54)$$

where ρ_o is the density of sea water.

This concludes chapter 1 of the thesis. The rest of the chapters in this thesis are addressed as follows: The model used and the set up of the experiment will be described in chapter 2. In chapter 3 we look at changes to the meridional overturning circulation in the ocean and its consequence to the heat content structure. In chapter 4, we focus on the dynamics in the atmosphere and apply the same diagnostic on eddy momentum fluxes in the atmosphere as in HBD05. Finally, in chapter 5, the heat budget change in the atmosphere will be investigated. The difference in tropospheric temperature response between the fixed SST and fully coupled ocean case will also be highlighted. In doing so we hope to find out whether or not ocean coupling is important to the results of existing ST coupling studies.

2. Experimental Setup

2.1. Model Requirements

The aim of this experiment is to study and understand the mechanisms governing the tropospheric response to stratospheric ozone perturbation, in the presence of an interactive ocean. It is therefore beneficial to employ a simplified model to represent the Earth's climate system, while retaining some of the important aspects relevant to this study. Thus, through a set of carefully designed experiments, we aim to identify, pinpoint and explain the mechanisms and feedbacks in the atmosphere-ocean coupled system.

Models of different levels of complexity are available nowadays. They vary from simple 1-D radiative transfer models to state-of-the-art models like the HadCM3. These models are designed for different purposes and in general, it is a trade off between speed and the amount of detail represented by the model. The choice of resolution and level of complexity depends on the nature of the processes under investigation. Regional studies that involve specific small-scale processes might require a complex model running at a high enough resolution. For the purpose of this project, the model chosen must meet a number of requirements, which will be described in the following paragraphs.

Most existing ST coupling studies involve a thermal forcing in the stratosphere, which is either uniform in latitude or involves a change in equator-to-pole temperature gradient. There are many factors that could induce such a change in temperature in the stratosphere and one major cause is a change of stratospheric ozone concentration. Although not a necessity, forcing with a change of ozone as opposed to pure temperature perturbation include the effects of reduced downward shortwave in the troposphere caused by ozone absorption, which might have an impact on surface fluxes

and hence makes the study even more complete and interesting. Therefore, a model that is capable of including some important chemical species, such as greenhouse gases, is preferred.

In this study we are mostly interested in changes in large scale dynamical processes. Hence, the resolution of the model does not need to be extremely fine. On the other hand, as described in section 1.1.1, the dominant mechanism by which the stratosphere and troposphere are coupled is the transport of momentum by mid-latitude baroclinic waves, which lies in the horizontal plane and takes the form as shown in figure 1.7. Therefore, the model chosen for this study has to be 3-D and be able to account for the physics of these atmospheric waves and eddies.

In the atmosphere, orography is responsible for the generation of different features such as stationary Rossby waves and Lee waves [44]. In the ocean, orography plays an even more important role as the continents block and redirect the currents at their boundaries. In a rotating body like the Earth, these boundary conditions, together with the Coriolis effect, cause anticyclonic flow in the NH and cyclonic flow in the SH. This change of ocean circulation imply redistribution of heat and hence affects spatial structure of SST. This is of particular importance in our experiment, which has one of its main focuses on air-sea interactions. Considering the above complications that may arise from orography, it is ideal to simplify the Earth so that feedbacks from both the troposphere and the ocean can be highlighted. As will be discussed in more detail in section 2.4, the Earth will be modelled as an aquaplanet where there is no topography except for polar regions.

It is logical to look for a model that has a demonstrated record related to ST coupling studies, which makes it easier to diagnose the impacts of new elements in the new experiment as opposed to existing ST coupling studies. It also ensures that the specification and level complexity of the model is suitable for the project.

In summary, the model for this project should meet the following basic requirements - it needs to be a 3-D primitive equation atmosphere-ocean model and have the physics of radiative transfer built in; both the ocean

and atmosphere are fully interactive and does not rely on prescribed surface fields, such as SST, wind and heat fluxes; is reliable and has a demonstrated record in relevant ST coupling studies. The optional requirements are - it is flexible so that the topography is easily re-configured for further experiments; and takes into account effect of greenhouse gases in its radiation scheme. In the latter case, considering the trade off between computational runtime and level of complexity of the model, interactive chemistry is not a necessity.

2.2. Description of FORTE

The model used in this study is the Fast Ocean, Rapid Troposphere Experiment (FORTE) [58] and it meets all the requirements as described in section 2.1. It is built by the National Oceanography Center and is based upon two existing models, Intermediate General Circulation Model (IGCM3) as its atmospheric part, and Modular Ocean Model, Array Version (MOMA) as its ocean component. The philosophy behind how FORTE works is simple - both IGCM3 and MOMA are run simultaneously and at the end of each model day, they exchange information such as SST, surface wind fields, surface heat fluxes and fresh water fluxes. However, as these models were never designed to work together interactively, there are fundamental differences that had to be taken care of when FORTE was developed. For example, IGCM3 is a spectral model while MOMA uses a finite grid such that special treatment has to be made to ensure conservation of energy and mass when information are exchanged at the end of each cycle. The component responsible for this is the Ocean Atmosphere Sea Ice Soil (OASIS) coupler. Each of the three components of FORTE will be discussed in more detail separately in the following sections.

Regarding the purpose of this study, one approach to identify and highlight the importance of ocean feedbacks to ST coupling is to run an atmosphere-ocean coupled model repeatedly, with a specific element of interest (e.g. SST) taken out each time and compared with the control run. The computational expense of full complexity models implies that it would take a

very long time for a study of this kind to complete. Moreover, most of these studies utilise the use of idealised configurations, such as modelling the Earth as an aquaplanet where there is no continents, or flat continents so that the anticipated signal is clearer. The climate under these configurations are usually specific to the study and is not available elsewhere. As a result, in most cases, idealised studies require the user to spin up their models from rest to equilibrium, so that the study is self-contained. Again, speed is essential in the spin-up process which makes models of intermediate complexity like FORTE suitable for the job.

Despite a climate model of intermediate complexity, FORTE is fast compared to state-of-the-art models like the HadCM3 and therefore serves as an ideal platform for testing theories on how the Earth's climate system works. FORTE has been previously used and configured to study various aspects of Earth's climate system and proves to be a useful tool in understanding not only climate system nowadays but also in the past, long before human existed. For instance, Smith et al. [59] simulated the climate between the Paleozoic and Mesozoic eras by applying an idealised Pangean configuration to FORTE. The idea was to investigate the impact of ocean circulation has on climate. It turns out that the MOC is hemispherically symmetrical as one would expect but has a strength of $100Sv$ ($1Sv = 10^6 m^3 s^{-1}$). The climate was significantly warmer than that of today, with an extreme seasonal cycle over the supercontinient ranging from -28^oC to 50^oC. Similar studies are found in another paper by Smith et al. [60], in which three different scenarios, namely the 'Waterworld', 'Ridgeworld' and 'Drakeworld' are considered (see figure 2.1 for an illustration of these setups). Although the extreme settings used in these studies are not necessarily applicable to observations nowadays, these studies took advantage of FORTE and provides an important insight on how ocean circulation might affect the global climate. The capability of FORTE is not limited to highly idealised experiments. FORTE is also capable of adopting realistic topography to justify the importance of the roles played by the atmosphere and the ocean to specific forcing. Using a realistic topography for both land and bottom of the ocean, Blaker et al [5] applied a salinity anomaly at high latitudes in the Southern Ocean, which triggers a SST response both at the tropics and in the Northern Hemisphere. The experiment was then repeated with a non-

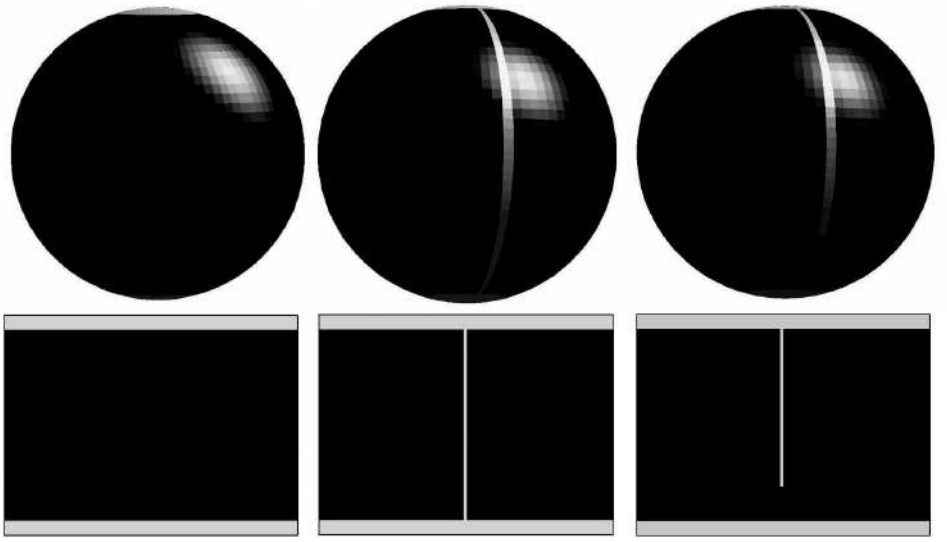


Figure 2.1.: Schematics of Waterworld (Left), Ridgeworld (Middle) and Drakeworld (Right). Bottom row shows the plain view of each setup. Black denotes sea surface and grey denotes land. Both the seafloor and land are uniformly flat. [60]

interactive slab ocean. In the case where the ocean dynamics is removed, the signal found in the Northern Hemisphere is similar to that fully coupled case while the tropical response is absent. It is suggested that the ocean is responsible for the equatorial SST response in response to this particular forcing while atmospheric processes plays a dominant role of extending the effects of the forcing to the other hemisphere. In this thesis, we will apply a similar approach of disabling the dynamics of the ocean, in an idealised setup however, to differentiate the parts played by the atmosphere and the ocean in an ozone perturbation experiment.

2.2.1. Atmospheric Component - IGCM3

The atmospheric component of FORTE is the version 3 of the Intermediate General Circulation Model (IGCM3) [12] from the University of Reading. It is a three-dimensional primitive equation spectral model that is based on the dynamical core of Hoskins and Simmons [27]. It has a multi-band radiation scheme that is capable of taking the effects of water vapour, CO_2 and O_3 into account. However, IGCM3 does not have interactive chemistry

built-in and therefore both CO_2 and O_3 need to be prescribed.

As described earlier IGCM3 does not run using a mesh of discrete grid points like MOMA. Instead, IGCM3 uses a spectral representation in the horizontal such that the variables (following Hoskins and Simmons [27], the equations of motion are formulated by the divergence D, vorticity ζ, deviation of temperature from the global mean at a specific level $T^{\dagger}$, geopotential ϕ and the natural logarithm of the surface pressure $\ln p_s$) that define motions at each level of the atmosphere are represented by a truncated series of spherical harmonics. The resolution of the atmospheric component of FORTE is hence determined by the total number of terms in the series. The longer the series, the better the model can resolve and hence the finer the resolution is. In IGCM3, a triangular truncation scheme is used such that the resolution is the same in both zonal and meridional directions [58].

The advantage of a spectral model is that they naturally give a better representation of the atmospheric waves than finite differencing models. In addition, they are more computationally efficient when dealing with linear equations. However, considering the fact that there are non-linear advective terms in the equations of motion, a purely spectral approach is not practical as it would involve a set of sophisticated relations to be added in order to account for the interactions between the different modes [58]. As an alternative solution, at each timestep, the spectral solutions to the linear part of the equations of motion are first computed in IGCM3, which are subsequently transformed into grid point space. The model then works out the contributions from non-linear terms in grid point space. Finally, the summation of the two is transformed back into spectral space before moving on to the next timestep.

Like other spectral models, the equations of motion in IGCM3 are written in terms of the divergence D and vorticity ζ instead of the horizontal wind components u and v. The above sets of formulation are related by,

$$\zeta = \frac{1}{R\cos\phi}\Big(\frac{\partial v}{\partial \lambda} - \frac{\partial}{\partial \phi}(u\cos\phi)\Big) \tag{2.1}$$

$$D = \frac{1}{R\cos\phi}\Big(\frac{\partial u}{\partial \lambda} + \frac{\partial}{\partial \phi}(v\cos\phi)\Big) \tag{2.2}$$

where λ & ϕ are the longitudes & latitudes as before and R is the radius of the Earth.

For the work described in this thesis, IGCM3 is run at a horizontal resolution of T42 (i.e. triangular spectral truncation at wavenumber 42) which is equivalent to approximately $2.8^0 \times 2.8^0$ in grid point space. There are 15 levels in the model, which are carefully chosen so that tropospheric response to stratospheric ozone perturbation is well-represented. The specified σ-levels ($\sigma = \frac{p}{p_s}$, where p is a specific pressure level and p_s denotes the surface pressure) are 0.0179, 0.0577, 0.1050, 0.1570, 0.2077, 0.2526, 0.2923, 0.3315, 0.3759, 0.4325, 0.5114, 0.6220, 0.7558, 0.8844, 0.9717 respectively.

Atmospheric phenomenons span over a wide range of both time and spatial scales. In climate modelling, the choice of the model's resolution restricts certain small-scale physical processes from being resolved. Running a model at a resolution fine enough to include every atmospheric processes is computationally expensive and is therefore not practical. Despite the fact that many of the physical processes operate on a much smaller scale than that of the general circulation, these are of a great importance to various aspects. For instance, the cumulus convection affects the general circulation through latent heat release and also vertical transport of momentum, heat & moisture [48]. In addition, it also has an influence on the radiation budget. Hence, the effects of the processes not resolved by the model also needs to be included in order to give a true representation of the atmosphere.

Regarding this, the clouds in FORTE are parametrised using a simplified version of the Slingo scheme [57], in which five different types of cloud are allowed - low ($\sigma > 0.7$), middle ($0.7 > \sigma > 0.35$), high ($0.35 > \sigma > 0.12$), shallow and deep convective clouds. In the case of low, middle and high clouds, their respective fractional cloud covers $C_{Low,Mid,High}$ are determined by relative humidity RH and is given by equation 2.3.

$$C_{Low,Mid,High} = ((RH - 0.8)/0.2)^2 \tag{2.3}$$

The abundance of the deep convective clouds C_{Deep} depends on the precipitation rate,

$$C_{Deep} = 0.245 + 0.125 \ln R_{Prep} \tag{2.4}$$

where R_{Prep} is the time-averaged precipitation rate in mm/day. Shallow convective clouds do not precipitate in IGCM3 and therefore a simplified version of the Slingo scheme is adopted such that the fraction of shallow convective cloud cover $C_{Shallow}$ is set to an average value of 0.3 at all times. In addition, all clouds are assumed to have a fixed effective radius of $5\mu m$ to help adjusting the net SW at the TOA [49].

The shortwave radiation scheme of FORTE follows that of Morcrette [45] which covers two wavelength bands ($0.25 - 0.68\mu m$ and $0.68 - 4.00\mu m$). For the longwave, the Reading Wide Band Model (RWBM), which includes six spectral bands, is used. RWBM is based on a series of pre-computed transmittance tables and includes the effect of ozone, water vapour and carbon dioxide. It is about three times faster than the Morcrette LW scheme [49]. Ozone is prescribed from a monthly-averaged climatology. In contrast, while IGCM3 allows the water vapour profile to be prescribed like ozone, the alternate option of settings water vapour as a fully diagnostic variable (i.e. interactive) is taken in FORTE. Carbon dioxide is set to a uniform concentration of 358 $ppmv$ (parts per million by volume) throughout the atmosphere. Other absorbers such as CH_4,N_2O and halocarbon is switched off for faster computing time.

The cloud scheme of the RWBM follows the method of [9], which states that the transmittance T_r^{Cloudy} of a cloudy sky is given by,

$$T_r^{Cloudy} = (1 - A_C)e^{-1.66\tau_A} + A_C e^{-1.66(\tau_A + \tau_C)} \tag{2.5}$$

where A_C is the fractional cloud cover, τ_A and τ_C are the optical depth of the atmosphere and cloud respectively. By rewriting $1 - e^{-1.66\tau_C}$ as the cloud emissivity ϵ and $e^{-1.66\tau_A}$ as the clear sky transmittance T_r^{Clear}, equation 2.5 becomes,

$$T_r^{Cloudy} = (1 - \epsilon A_C)T_r^{Clear} = CT_r^{Clear} \tag{2.6}$$

In order to account for multiple cloud layers with random overlapping (a maximum of three cloud layers plus a deep convective cloud is allowed in the scheme), the parameter C in equation 2.6 is written as the product of all cloud layers,

$$C = \prod_i C_i \tag{2.7}$$

The cloud emissivity ϵ in equation 2.6 is determined by the liquid water path (LWP), as described by [51].

$$\epsilon = \begin{cases} (1 - e^{-0.1LWP})/(1 - e^{-2.5}) & \text{if } LWP \leq 25gm^{-2} \\ 1 & \text{if } LWP > 25gm^{-2} \end{cases} \tag{2.8}$$

Equations 2.5-2.8 is implemented in the subroutine CLDTRAN in IGCM3. The impact of CLDTRAN regarding this study will be described in section 4.3.4.

2.2.2. Ocean Component - MOMA

The ocean model is the array version of the Modular Ocean Model (MOMA)[67], which is based on the code developed at the Geophysical Fluid Dynamics Laboratory (GFDL). It is a three-dimensional primitive equation model in which the state of the ocean is described by its potential temperature, velocity, salinity, pressure and density. In order to improve model efficiency three assumptions are made in the formulation of the equations of the model [6]. Firstly, ocean is incompressible such that the continuity equation in Cartesian coordinate reduces to,

$$\nabla \cdot h\vec{U}_o + \frac{\partial h\vec{w_o}}{\partial z} = -\frac{\partial h}{\partial t} \tag{2.9}$$

where h is the height of the water column, $\vec{U_o}$ and $\vec{w_o}$ are the horizontal and vertical components of the ocean current respectively. Secondly, it is assumed that the vertical motions are negligible in the ocean and terms involving $\vec{w_o}$ are neglected in the vertical momentum equation. The third assumption is the Boussinesq approximation, which states that the small changes in density can be neglected except the case when gravity is also involved.

Unlike the IGCM3, MOMA is a finite difference grid model and all the calculations are carried out in grid point space under the Arakawa B grid scheme - sea potential temperature, salinity, and vertical velocity are calculated on one grid while horizontal velocities are evaluated on a different one. In the horizontal, MOMA runs at a slightly finer resolution than IGCM3 in this study. The size of each grid box size is $2^0 \times 2^0$. There are 15 depth levels and are chosen to be: $10m$, $43m$, $101m$, $185m$, $305m$, $472m$, $695m$, $987m$, $1355m$, $1809m$, $2350m$, $2977m$, $3683m$, $4454m$, $5272m$.

As opposed to early versions of the model which was constrained by computing power and hence forced to use a rigid-lid scheme, the current version of MOMA has a free surface formulation [32]. As a non-eddy-resolving model, mesoscale eddy mixing on isopycnal surfaces is parametrised following the method of [15].

The model has a long history which originates from the pioneer work by Kirk Bryan back in 1960's. Improvements have been made ever since and nowadays MOMA is used for studying ocean circulation over a broad range of space- and time-scales. Despite MOMA's capability of simulating real world observations, it is highly flexible and can be easily configured to handle highly idealised experiments.

2.2.3. Coupler - OASIS

The atmospheric and ocean components of FORTE are coupled together via the OASIS coupler, which is the acronym of Ocean Atmosphere Sea Ice Soil. It was built at the Center Europeen et de Formation Avancee en Calcul Scientifique (CERFACS) and is specifically designed to allow information to be exchanged between component models that are of different grid size, without the need of making substantial alternations to each of the models.

The way IGCM3 and MOMA are coupled together is by exchanging boundary information, instead of reading from prescribed fields from as they do when run in standalone mode. The fundamental idea is that for each time step, both IGCM3 and MOMA collect and store boundary data of various fields. At the end of each model day, the accumulated data is averaged and

fed into the other half of the model. IGCM3 takes the accumulated SST data from MOMA, and in return, provide boundary information such as wind stresses, radiative, sensible & latent heat fluxes and fresh water fluxes to the ocean component. These are then accepted as the new boundary condition for next model day.

Apart from the difference in grid size there are other issues to be considered. For instance, MOMA has no sea-ice model built-in and coupling to IGCM3 results in unphysical sea water temperature at polar regions. A sea-ice parametrisation is introduced in which sea-ice forms whenever sea temperature drops below 2^o [58]. On the other hand, when coupled, the assumption of the ocean as a infinitely large fresh water reservoir by IGCM3 is no longer valid as fresh water flux changes the salinity which would alter the thermohaline circulation. A runoff scheme which transports fresh water to suitable ocean basins was introduced to solve the problem [58].

2.3. Hardware Specification

In this project, FORTE is run on a Linux machine (version 2.6.9-42.0.3), running with two Intel(R) Xeon(R) Dual Core CPU 5160, each at 3.00GHz. The compiler is the GCC compiler (version 3.4.6 20060404). With the resolution as mentioned in section 2.2, it takes this machine around 10 hours for a 5-year model run. This translates to less than four months for the model to reach equilibrium.

2.4. Model Setup

As mentioned previously, the primary objective is to study the stratosphere-troposphere dynamics in an atmosphere-ocean coupled model. In a complex situation like the Earth's climate system, it is sometimes difficult to study and understand a specific physical process in the existence of many other interactions that are unimportant to the study but might dim the desired signal. For this purpose, it is best to simplify the problem and to eliminate some of the processes that we are not currently interested in. This is achieved by omitting the orography so that there are no large-scale zonally asymmetrical forcings. In addition, this is analogous to the setup in

both HBD05 and SBH09, which allows easy comparison of the results in this study to those mentioned. It is important to bear in mind that the experiments described in this thesis are by no means realistic and they are not meant to simulate and reconstruct real world observations.

In this project, the Earth is modelled as an aquaplanet, where there is no land except for latitudes higher than 82^o. This is to minimise the possible computational constraints caused by convergence of meridians at the poles. This is a similar setup as the 'Waterworld' in [60]. The albedo of polar islands is set to 0.77 while the ocean has an albedo of 0.10. Initially,

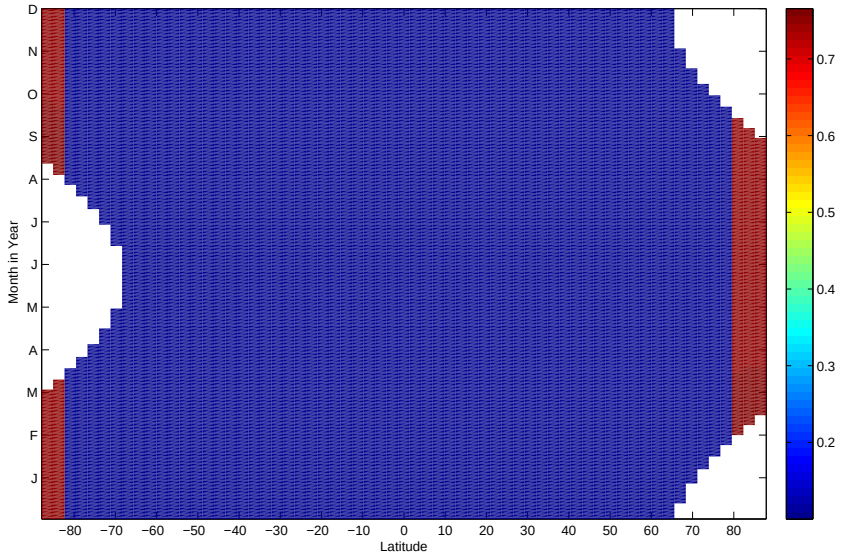


Figure 2.2.: Time-latitude plot of surface albedo at year 1020 (close equilibrium). White areas indicate the latitudes where there is no incident solar radiation around solstice.

both the atmosphere and the ocean are given a standard temperature profile, with the wind and current fields set to zero. As mentioned in section 2.1, O_3 is prescribed from climatology. The model is left to run for 1020 model years. The model is then configured to output at the end of every model day, rather than exporting data monthly as it previously did, and ran for a further 15 years. This is to allow time-varying eddies to be diagnosed

(see section 4.3). The data presented in this thesis is taken from the last 15 years of model run. This is the control of the experiment.

Model year 1020 is also the time when the experiment then branches into different scenarios to suit the aim of the project. In experiment $x5O_3$, after the model has reached equilibrium (i.e. year 1020), an ozone forcing of five times its original value is applied. As in the control, the model is then left to run for 15 years with daily output. The forcing is left on throughout the 15-year run. The perturbation is chosen to be uniform in latitude and follows the shape of the aquaplanet tropopause (i.e. only stratospheric ozone is perturbed). Figure 2.3 illustrates the distribution of the original ozone profile and the location of the applied ozone perturbation. This is expected to induce a temperature increase in the stratosphere that is non-uniform in latitude by enhanced ozone absorption.

In order to investigate the role of an interactive ocean plays in an ozone perturbation experiment as described above, one has to isolate it from the atmosphere. As IGCM3 was originally designed to run with a slab ocean in which no ocean dynamics is involved, one way of achieving this is to replace FORTE with the stand-alone version of IGCM3 after the model has reached its equilibrium. The advantage is that, with one less component to run simultaneously, even though FORTE is run on a dual-core machine in this experiment, FORTE should benefit from a slight speed gain. On the other hand, the standalone version of IGCM3 is designed to meet our purpose of de-coupling the ocean. IGCM3 is the atmospheric component of FORTE and in theory, there should be no discrepancies apart from the ocean coupling.

It is worth noting though, minor changes as described in section 2.2.3 were made to both IGCM3 and MOMA so that they could be coupled to each other. These include the sea-ice parametrisation and the run-off scheme. Even though the discrepancies between the standalone and ocean-coupled version of IGCM3 might not cause a significant problem in the case of an aquaplanet, where there is little land cover, it is worth making every effort to avoid these unnecessary uncertainties.

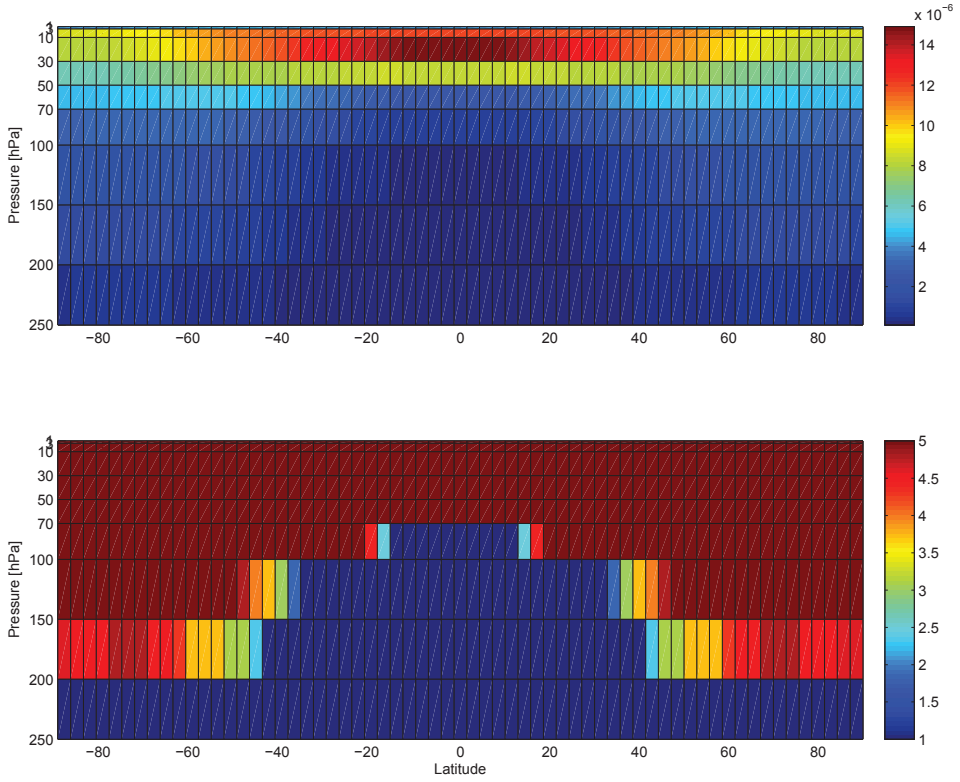


Figure 2.3.: Time-averaged zonal mean ozone profile near the tropopause in parts per million (ppm) (top). Ratio of the applied annual mean ozone perturbation at year 1020 and its original value (bottom). Note that the prescribed ozone has a seasonal cycle and hence the boundary of the perturbation is not exactly 5 times its original value when averaged annually.

The way the ocean feeds back on to the atmosphere, is via changes in the SST. A simple and straightforward way to stop the two components from interacting is by controlling the SST data that is read into IGCM3 at the time IGCM3 and MOMA exchanges information. Experiment $x5O_{3FSST}$ is exactly the same as $x5O_3$ except that from the time the ozone perturbation is applied, the SST field is read from an external data file instead of taking what MOMA provides. The file contains the SST taken from the year before the ozone forcing is applied and has a full seasonal cycle.

In other words, both IGCM3 and MOMA do their calculations as they would normally and at the end of each model days, MOMA reads the necessary data from the atmospheric component while IGCM3 ignores the SST input from MOMA and reads from an external file instead. This renders the calculation done by MOMA irrelevant and is effectively secluding the ocean dynamics from the system. This is more of a 'one-way' isolation. It also implies that the ocean becomes an energy reservoir of infinite capacity. Suppose that there is an increase in downward radiative flux at the surface, while the ocean is aware it there will not be any SST feedback that is noticeable by the atmosphere.

The only disadvantage of fixing the SST is the inefficient use of processor. The calculations done by the ocean component are completely ignored and the computing power could be better invested in speeding up IGCM3. Nevertheless, given that the model only needs to run under such condition for 15 model years (approximately 1.5 days computer run time) and the multitasking capability of the dual core processor used, this is acceptable. The advantage is that this method needs the minimum amount of procedures that would achieve what is required. It also eliminates the possible technical difficulties of completely detaching OASIS and MOMA from FORTE. In addition, this method allows one to study the response of the ocean in the absence of ocean feedbacks.

2.5. Aquaplanet Climatology

In this section, an overview of the climatology of the aquaplanet will be presented. Despite increasing popularity, aquaplanet experiments are not the

most common experiments in climate research studies. Therefore, the aim of this section is to give the reader a 'feeling' of what an aquaplanet should look like. Even though FORTE has previously been used in aquaplanet-based experiments [58, 59, 60], depending on the configurations (e.g. horizontal and vertical resolutions, the chosen model levels, and the supplied climatology profiles), the results might be similar but not identical to this study.

As described before, FORTE is an AOGCM of intermediate complexity, which is intended to fill the gap between simple radiation-balancing models and fully coupled state-of-the-art models. In this study, FORTE is configured to run an aquaplanet experiment which is highly idealised. Therefore, the climatology is expected to be different, in many ways, to real world observations. It is also important for the reader to bear in mind that this project does not aim to simulate the full climate of the real world but to study specific mechanisms both in the atmosphere and the ocean. Although the results presented as follows resembles some of the key features as observed in reality, they are still different in many ways, which will be discussed in the following subsections.

2.5.1. Atmosphere

Air temperature

To discuss the temperature structure of the atmosphere, a zonal mean of air temperature for the control run is shown on the top panel of figure 2.4. Its zonal mean cross sections under JJA and DJF conditions are shown on the bottom panels. One of the most noticeable features of an aquaplanet is its warm temperature, compared to other standard temperature profiles (e.g. figure 2.5). The surface air temperature varies from a maximum of 25^oC at the tropics to a minimum of 7^oC at the poles. Note there is a local minimum centered at the equator at the surface. As we shall see later in section 2.5.2, this is due to the upwelling of cold water in the ocean in that region.

As one would have expected, figure 2.4 shows a rapid decrease of temperature with altitude in the troposphere. For instance, the difference in temperature between the surface and the thermal tropopause is 105^oC at

the equator. Above the thermal tropopause, the temperature increases with respect to height due to absorption of UV by ozone and applies to all latitudes in the summer hemisphere. However, in terms of annual mean, the lower stratosphere is isothermal at polar latitudes.

Regarding seasonal variation, although there are occasions in which polar surface air temperature drops below 0^oC (not shown), they do not occur frequent enough to show up in the zonal average in the DJF and JJA plots.

Precipitation

The rainfall distribution of an aquaplanet is distinct. Figure 2.6 shows the global distribution of precipitation rate of the aquaplanet control run, in units of $mmday^{-1}$. As there are no continents except for the polar caps, it follows that the rainfall exhibit a banded structure in the zonal direction, as opposed to local maximas and minimas over sea and land and along a latitude circle in reality. There are two ITCZs (Intertropical Convergence Zone), located at 10^oN and 10^oS. This is due to the fact that air temperature near the surface is colder at the equator than that at subtropical altitudes, which allows air in this region to carry less water vapour.

The global mean rainfall in the aquaplanet is $3.89mmday^{-1}$, which is 45% higher than real world observation [73]. In addition to the warmer tropospheric temperature as shown in section 2.5.1, the majority of aquaplanet is covered by sea water. These factors allow more water vapour content in the air, and hence the enhanced rainfall.

Wind

The zonal mean zonal and meridional wind fields are plotted on figure 2.7. The jet-stream is centered at 35^o in latitude at the $150hPa$ pressure level. Despite locating higher up than the observed in real world scenarios, the jet-streams in the aquaplanet have a peak magnitude of $25ms^{-1}$, which is also slightly weaker (see figure 2.8).

The most astonishing feature in an aquaplanet is the unusually strong east-

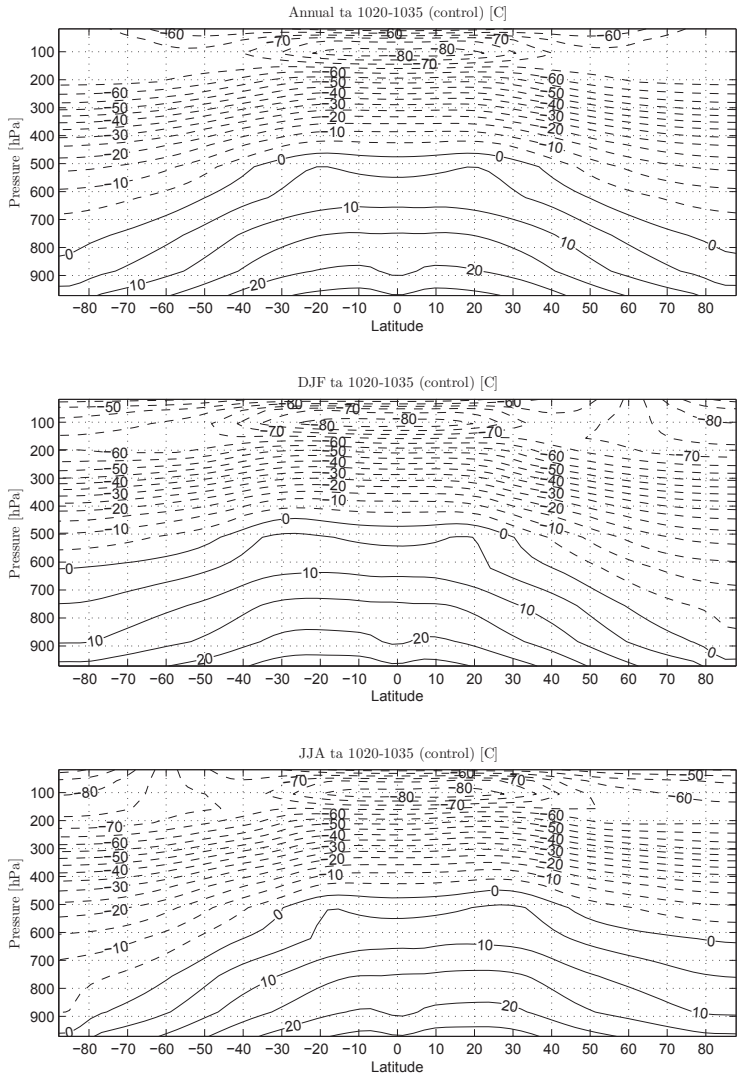


Figure 2.4.: Zonal mean air temperature (control) for annual-mean (top), DJF (middle) and JJA (bottom) conditions. Data averaged over years 1020-1035 [^oC]. Contour interval = 5^oC.

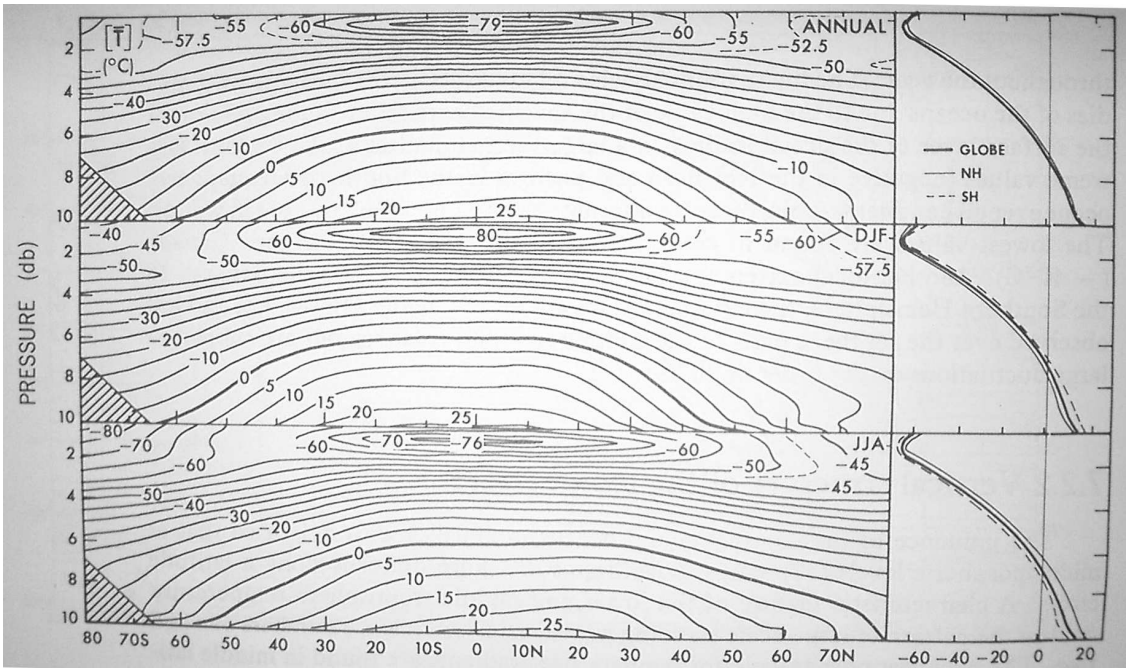


Figure 2.5.: Zonal mean cross sections of air temperature (control) for annual-mean (top), DJF (middle) and JJA (bottom) conditions in ^oC [48]

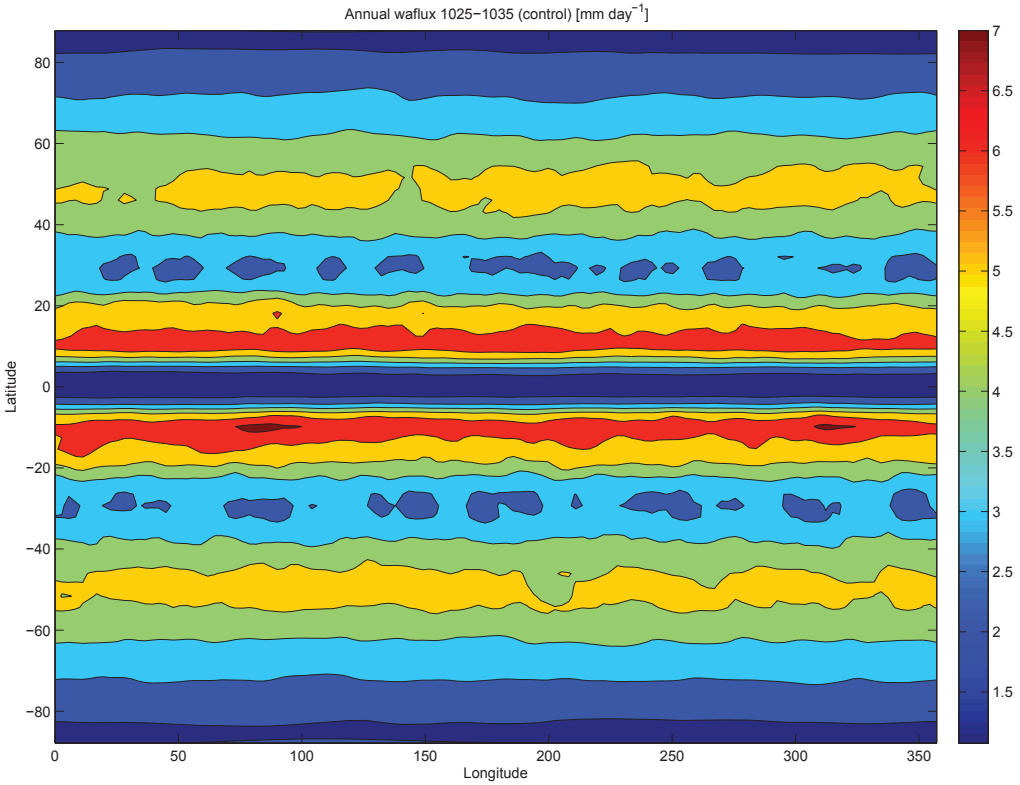


Figure 2.6.: Annual mean precipitation (control), averaged over years 1020-1035 $[mmday^{-1}]$.

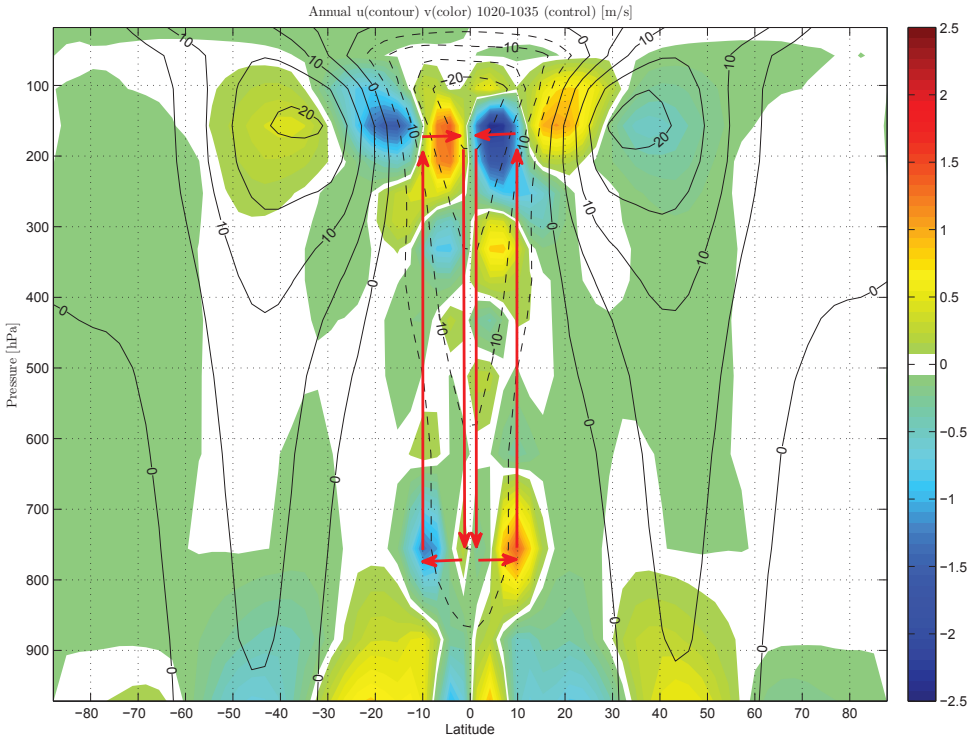


Figure 2.7.: Zonal mean zonal(contour) and meridional(meridional) wind field (control), averaged over years 1020-1035 $[ms^{-1}]$. Contour intervals are $5ms^{-1}$ for the zonal plot and $0.1ms^{-1}$ for the meridional plot.

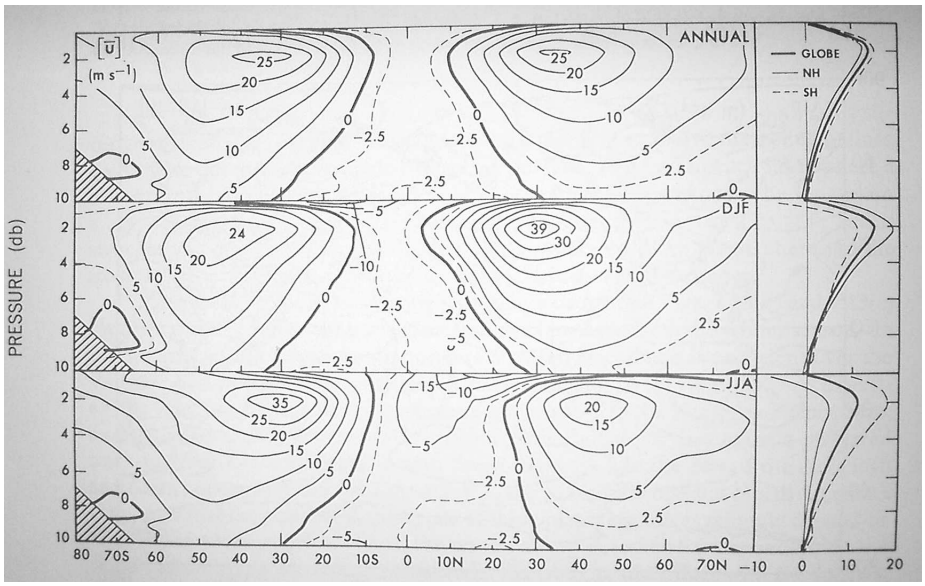


Figure 2.8.: Zonal mean cross sections of zonal wind (control) for annual-mean (top), DJF (middle) and JJA (bottom) conditions in ms^{-1}. Vertical profiles of hemispheric and global mean values are shown on the right. [48]

erly wind centered at the equator. It is wedged between the jet-streams and extends from the surface all the way up to the lower stratosphere. Its peak magnitude comparable to that of the jet-streams and is located roughly at the same level.

The observed equatorial easterly wind in the aquaplanet could be explained by looking at its annual mean meridional wind field. Referring to the colored contour plot in figure 2.7, just below the $150hPa$ pressure level, there is strong equatorward flow of air originating from 10^o in latitude in both hemispheres. On the other hand, in the meridional direction, surface air is directed poleward. These opposing flows of air form an anticlockwise (clockwise) meridional circulation over the tropics of the Northern Hemisphere (Southern Hemisphere), and is found to oppose the Hadley cell as described in section 1.2.2. The direction of this 'inverted' cell is illustrated by the overlaying red arrows in figure 2.7.

Referring to figures 2.4 and 2.6, there is a local minimum of surface temperature and humidity at the tropics and is centered on the equator. This is due to the cold tongue in the ocean at the equator, which will be discussed in section 2.5.2. The low level of rainfall at the equator indicates that there is no upward flow of air and therefore equatorial air in this aquaplanet is not moist. In contrast, poleward of the equatorial cold tongue, there is a warm region which encourage convection of air. In an aquaplanet, surface air are moist at most latitudes and hence maximum (minimum) water vapour content in the air provides locates the latitudes where upwelling (downwelling) of air occurs. The equatorial cold tongue also explains why the ITCZ in this aquaplanet in not centered at the equator.

As equatorial surface air in the aquaplanet ascends, although at slightly different latitudes as in the real world, moisture and heat are carried up in the atmosphere. As they ascend, heat is transported to the surrounding cold regions to reach radiative equilibrium. In the case of an aquaplanet, heat is transported both poleward and equatorward. The poleward flow of air resembles the Hadley cell, while the equatorward branch from each hemisphere meets and returns down to the surface at the equator. A plot of the zonal mean cross section of the mass stream function is shown in figure

2.9. It can be observed that the Hadley cell is narrower than expected (as shown in figure 2.10). It is squeezed between the 'inverted' cell & the Ferrel cell and is located between $10^o - 30^o$ in latitude. In terms of meridional cell width, the Ferrel cell and polar cell are not significantly affected by the 'inverted' cell.

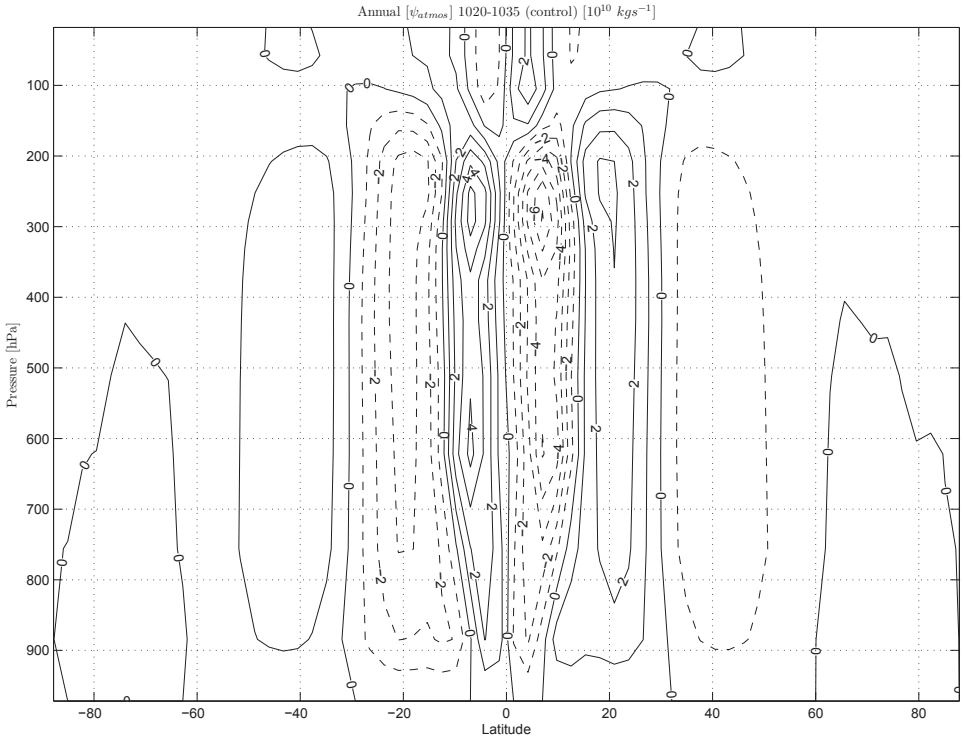


Figure 2.9.: Zonal mean cross sections of the mass stream function, averaged over years 1020-1035 [$10kgs^{-1}$]. Contour intervals are $10kgs^{-1}$. Solid (dotted) lines shown clockwise (anticlockwise) circulation.

Regarding the unusually strong easterly at the equator, note the direction of the upper branch of the 'inverted' cell. Expanding the first term on the right hand side of equation 1.3, which represents acceleration due to Coriolis force,

$$-2\vec{\Omega} \times \vec{U_r} = 2\Omega \begin{pmatrix} vsin\phi - wcos\phi \\ -usin\phi \\ ucos\phi \end{pmatrix} \tag{2.10}$$

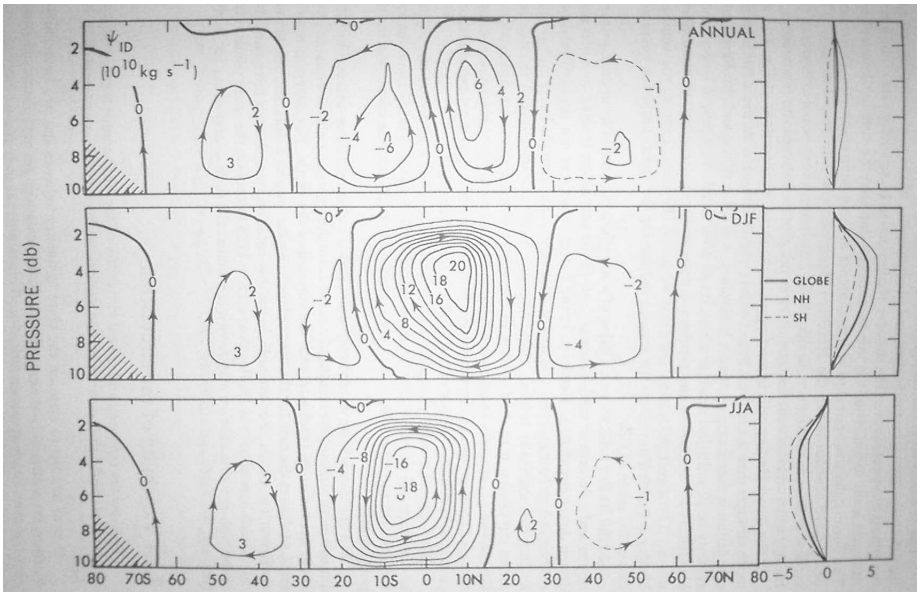


Figure 2.10.: Zonal mean cross sections of the mass stream function in $10^{10} kgs^{-1}$ for annual, DJF, and JJA mean conditions. Vertical profiles of the hemispheric and global mean values are shown on the right [48].

and assuming that vertical motion is small enough to be neglected, equation 2.10 reduces to to a horizontal plane equation, as shown in equation 2.11

$$\begin{pmatrix} \frac{du}{dt} \\ \frac{dv}{dt} \end{pmatrix}_{Coriolis} = \begin{pmatrix} v \\ -u \end{pmatrix} f \tag{2.11}$$

Using equation 2.11, it follows that the upper branch of the 'inverted' cell, which is flowing equatorward, would accelerate zonal wind in the westward direction. This results in the unusually strong easterlies at the tropics.

TOA Radiation

A time series of the net radiation at the TOA for the control run is shown in figure 2.11. The top diagram of figure 2.11 shows that the net radiation flux entering the aquaplanet's system oscillates around zero with an amplitude of $10 W m^{-2}$. Due to the Earth's elliptical orbit around the sun, the net TOA radiative flux is modulated and has a period of 360 days. This is supported by fact that the incoming shortwave radiation varies the greatest with time, compared to the other components. The reflected shortwave received at the TOA shows a similar cycle, as would have been expected. The net TOA radiation averaged over the last 15 years of control run (year 1020-1035) is 0.110 $W m^{-2}$, which shows that by year 1035 the aquaplanet is close but not exactly at its equilibrium. The planetary SW albedo is 0.307.

2.5.2. Ocean

Surface currents

The lack of continent in an aquaplanet implies there is no zonal pressure gradient in the ocean. Hence, the current flow in the aquaplanet is zonally symmetrical and no gyre is observed. A vector plot of the surface current is shown in figure 2.12. At the surface, the peak magnitude of westward zonal currents is found to be $3.43 m s^{-1}$ (westward) at the tropics. In the subtropics, the speed of westward flowing water only goes up to $0.41 m s^{-1}$.

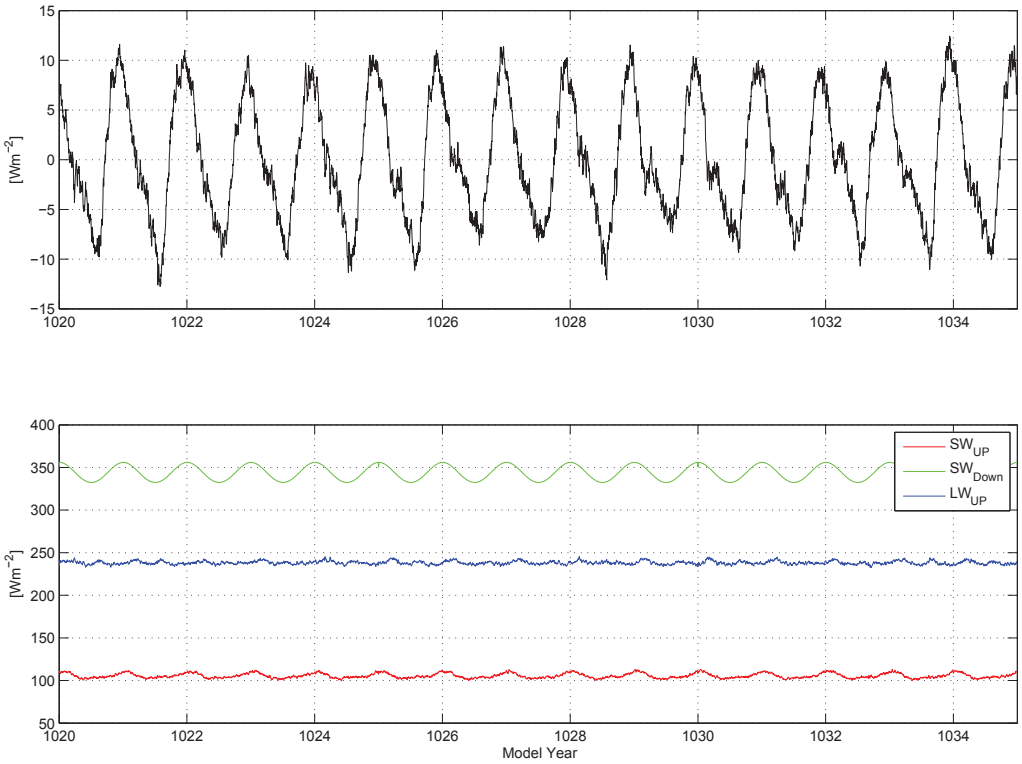


Figure 2.11.: Time series of TOA net radiation (top) and its components (bottom), in Wm^{-2} in the control run. SW and LW denotes shortwave and longwave radiation respectively. The direction is indicated in the subscript in each legend entry.

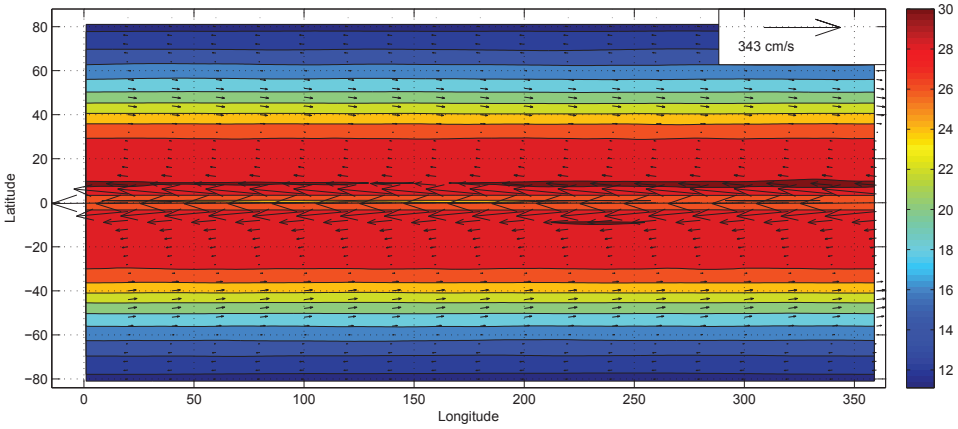


Figure 2.12.: Annual mean SST $[^oC]$ and surface currents $[cms^{-1}]$ (control), averaged over years 1020-1035.

Meridional Overturning Circulation

The meridional overturning circulation (MOC) of the aquaplanet control run consists of 3 cells in each hemisphere, as shown in figure 2.13. The structure of the MOC is found to be the same as in [58]. Each of the three cells have a meridional width of 30^o, and extends from the surface all the way down to the bottom of ocean. The locations of these cells coincide with the direction of the zonal wind stress as shown later in figure 3.1, which suggests they are wind-driven. Hence, except in the deep tropics, the MOC as shown in figure 2.13 is a 'mirror' image of the meridional circulation in the atmosphere. The tropical cell is much stronger than the mid-latitude and polar cells and has a peak overturning strength of $100Sv$. Referring to equation 1.31, the wind driven mass transport $\vec{m}_{ek}$ is inversely proportional to the Coriolis parameter f, and hence $sin\phi$. Therefore, despite the weaker surface wind stress compared to that at mid-latitudes (figure 3.1), the MOC is the strongest at equatorial latitudes.

The reason why the MOC in this aquaplanet consists only of deep-reaching Ekman cells has been explained in [58]. In an aquaplanet, there is no continent which implies there is no zonal pressure gradient that supports zonally asymmetrical flow. This is evident as it has been shown in figure 2.12 that there is no gyres. Hence, the surface wind stress and bottom friction

becomes the only dominant factors in driving the MOC. In the design of FORTE, artificial viscosity is deliberately added so that the model will yield a stable solution under the finite resolution adopted. According to [58], the drawback of including artificial viscosity is that it allows return flow of fluid at all depths in the model.

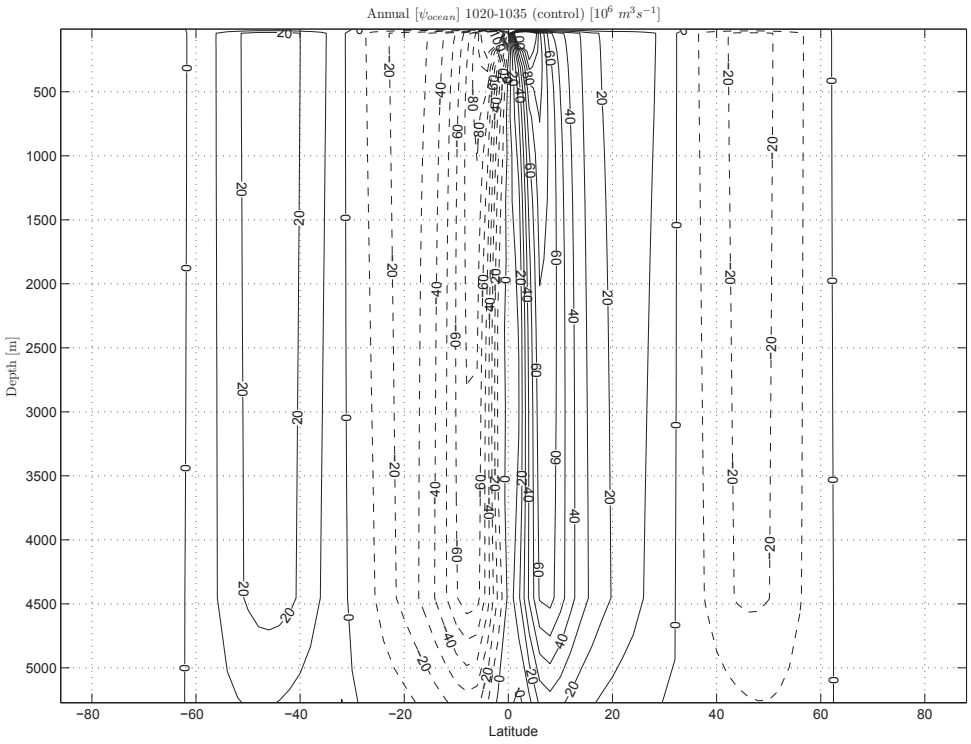


Figure 2.13.: Zonal mean meridional overturning circulation in the ocean (control), averaged over years 1020-1035 [Sv]. Contour interval = $10Sv$. Solid (dotted) line denote clockwise (anticlockwise) circulation.

Sea Potential Temperature

As would be expected by looking at atmospheric temperature, sea water temperature is also warmer than that of real world climatology. A zonal mean cross section of sea potential temperature of the first $1000m$ of the ocean is plotted in figure 2.14. The distribution of SST is zonally symmetrical as one would expect and ranges from a minimum of 9^oC at polar

latitudes to a maximum of 29^oC at 10^o in latitude. As mentioned in section 2.2.3, FORTE has no sophisticated sea-ice model built-in and assumes formation of sea ice when the sea temperature drops below -2^oC. Under this criterion, there is no sea ice formed at any time of the year. Referring to the vertical profile of sea potential temperature as shown in figure 2.15, there is no region with distinctive drop of temperature with respect to depth. Hence, there is no obvious thermocline in the aquaplanet.

The deep reaching Ekman cells as mentioned previously has an effect on the vertical temperature profile in the ocean and can be readily seen at the tropics in figure 2.14, where there is a column of cold water centred at the equator. The location of this 'cold tongue' coincides with the upward branch of the tropical Ekman cell in the ocean and this is not accidental. In contrast to real world scenarios, the Ekman cells in the control aquaplanet stretches down to the ocean floor and is able to transport heat from the surface to the bottom of ocean and vice versa. For instance, as illustrated in figure 2.13, the top branch of the tropical Ekman cell is directed poleward and therefore transports heat poleward. At 30^oN where there is a convergence of current, surface water is forced down into the depth of the ocean, and hence a change in horizontal temperature gradient at this latitude. Similarly, at the equator where there is a divergence of meridional surface flow, upwelling of cold water from the abyss occurs, and creates a cold tongue centred at the equator. The cold tongue extends to the surface and affects the SST, which also gives rise to the 'inverted' cell in the atmosphere.

2.5.3. Sea Temperature Drift

Figure 2.16 shows the time-integrated net energy flux (SW + LW + sensible + latent) at the surface into the ocean and the time series of the actual heat content change since model year 1020. It is obvious that two are in good agreement with each other and the model is not in perfect equilibrium as there is net energy going into the ocean after year 1020, with a net gain in energy of $1.8 \times 10^{23} J$ over 15 years.

Figure 2.17 shows the time series of annually averaged global mean sea potential temperature, from year 585 to 1035. It is observed that the slope

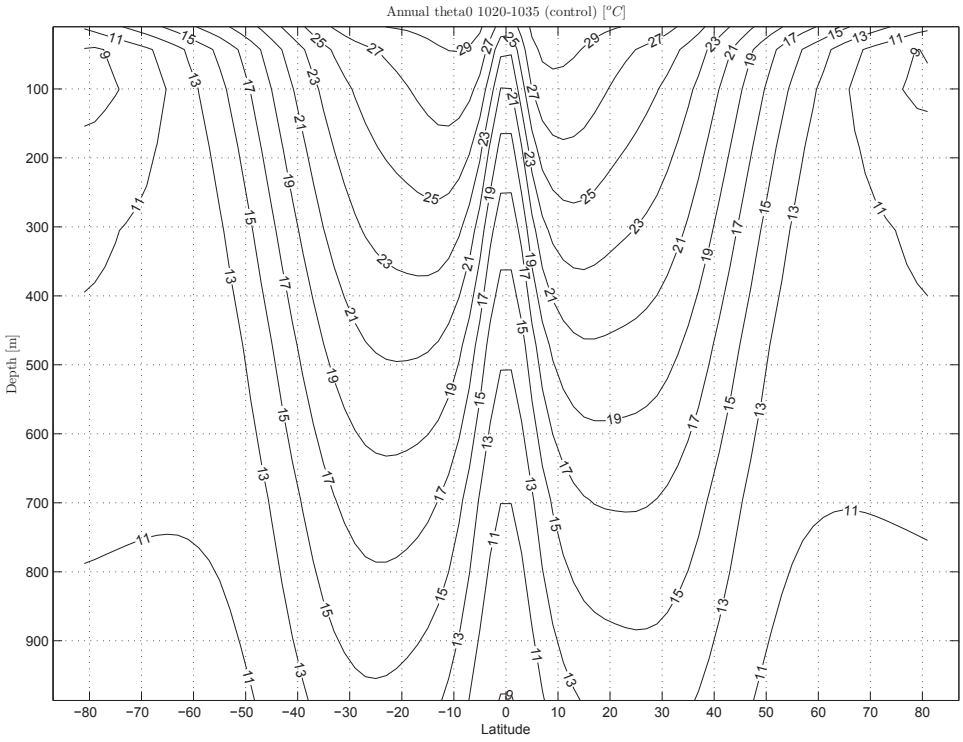


Figure 2.14.: Zonal mean sea potential temperature (control), averaged over years 1020-1035 [^oC]. Contour interval = 2^oC

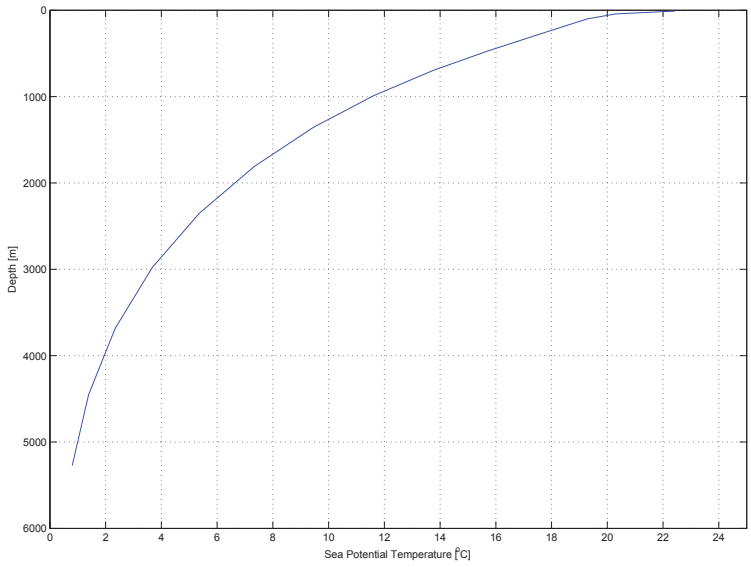


Figure 2.15.: Vertical profile of sea potential temperature (control), averaged over years 1020-1035 $[^oC]$

in figure 2.17 decreases from $0.014K$ per decade at year 585, to $0.009K$ per decade by the end of model run. Considering the time constraints on the project and that the sea temperature drift is small enough for the model to be considered to be in close equilibrium, we decide to perform the proposed ozone experiments at model year 1020.

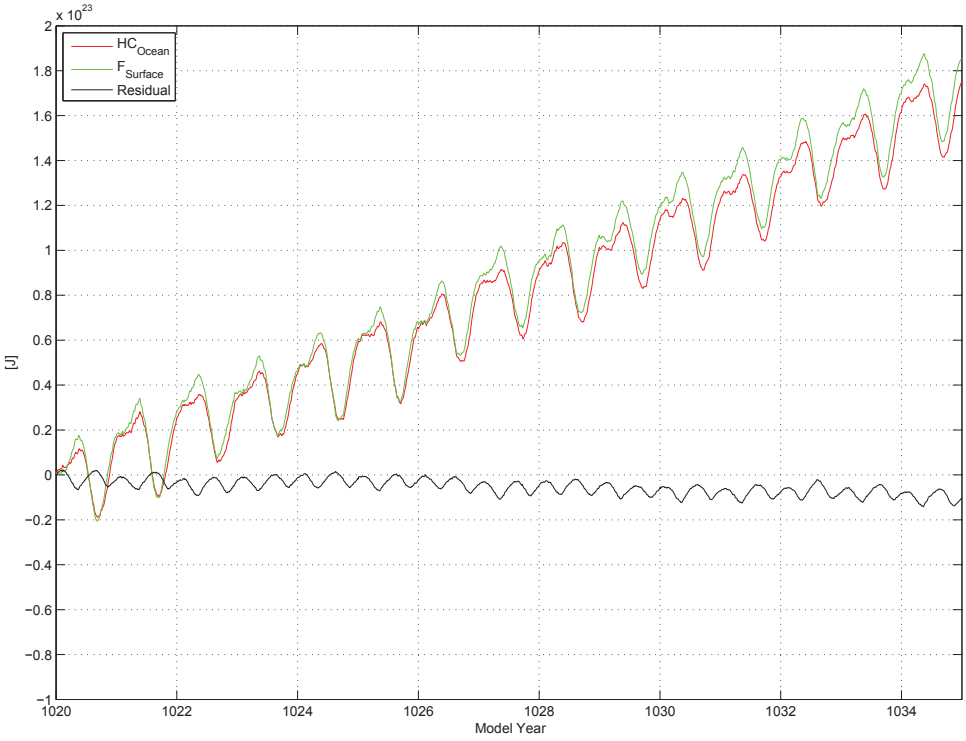


Figure 2.16.: Time-integrated net downward energy flux (radiative+sensible+latent) at the surface (green) and time series of ocean heat content change (red) since model year 1020 [J]. Black curve shows the difference between the two.

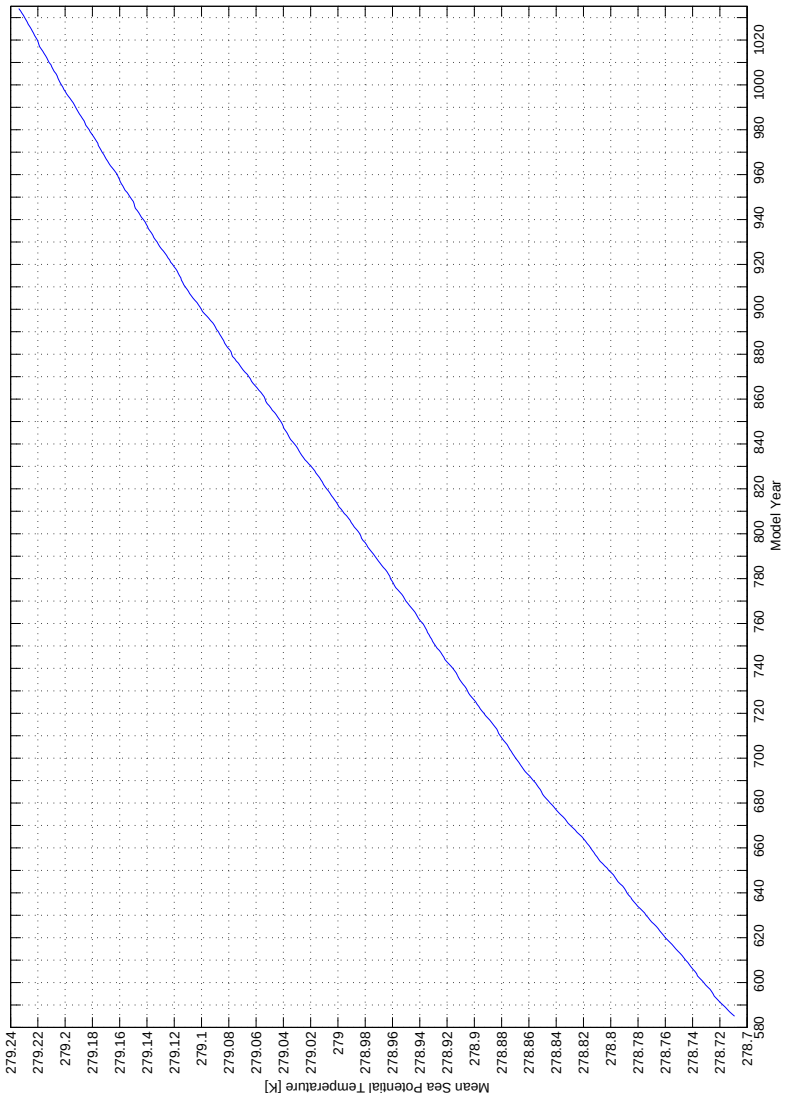


Figure 2.17.: Time series of annual mean sea potential temperature in K.

3. Results: Ocean

In this chapter we present an analysis on how the ocean reacts to surface condition changes induced by a perturbation of ozone up in the stratosphere. As described in section 2.4, starting from model year 1020, stratospheric ozone is increased by 5 times its original value, and the model is left to run for another 15 years for comparison with the control run.

The consequences of the the perturbation are expected to be on different timescales, depending on the nature of the processes. For example, the effect of reduced downward SW radiation at the surface is almost instantaneous while it takes the tropospheric jets about 40 days to adjust accordingly [56]. In contrast, majority of ocean phenomenon (except processes that occur in the surface layer such as Ekman pumping) are on much longer timescales than atmospheric ones. This is one of the reasons why the aquaplanet model has to be integrated for 15 years longer while most atmospheric processes will adapt to the perturbation relatively quickly. Even though the direct atmospheric response might be similar to that of previous ST coupling studies [50, 22, 68, 56], the end state of the atmosphere might be different due to delayed ocean feedbacks. In the case of a zonally symmetrical aquaplanet, the delay in SST response to radiative forcing could arise from thermal inertia of the ocean [29], its latitudinal dependence and energy transport mechanisms [52].

In section 2.5.2 we showed that the MOC is wind-driven and consists of Ekman cells that stretches from the surface to the bottom of the ocean. Therefore, in this chapter we focus on how the ocean circulation responds to changes to surface wind-stress, and how it might influence the SST.

3.1. Changes in Surface Conditions

3.1.1. Windstress

The zonal mean zonal wind stresses of the control and $x5O_3$ run are plotted in figure 3.1. In the control run, the trade winds at the tropics peaks at around 20^o and the mid-latitude jet stream is centerd at around 48^o. The polar easterlies reaches it maximum at around 73^o and dies off quickly above 80^o due to surface friction from polar islands. In the case of the

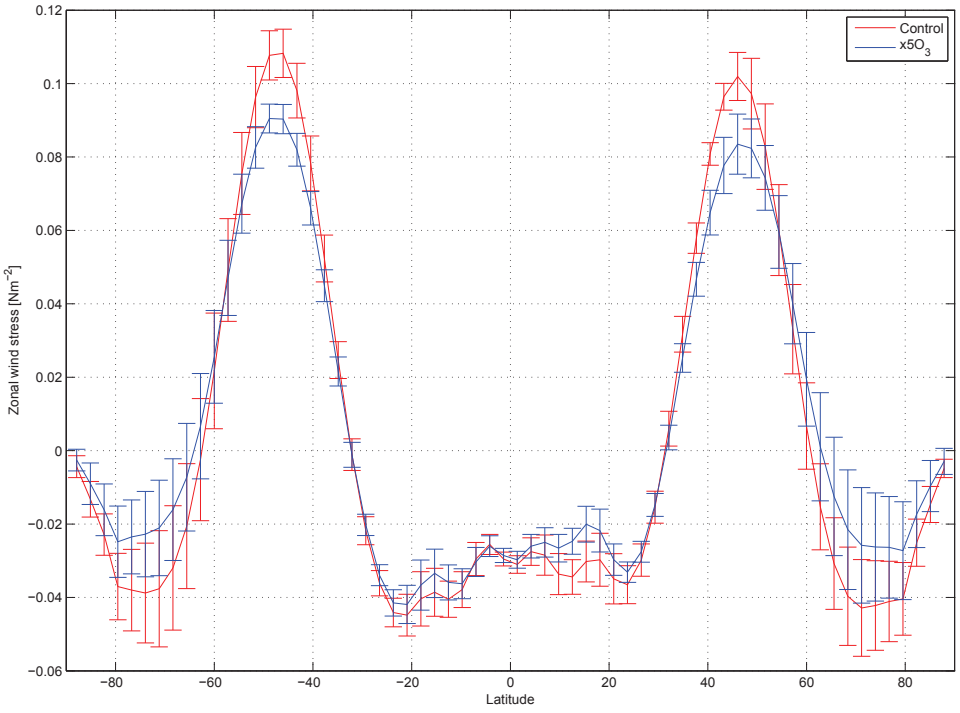


Figure 3.1.: Zonal mean zonal wind stress τ_x for the control (Red) and $x5O_3$ (Blue) run, averaged over years 1020-1035 $[Nm^{-2}]$. Errorbars show the standard deviations of the annual mean zonal wind stress for each latitude.

$x5O_3$ run, the peak surface trades & prevailing westerlies are found roughly at the same latitude. However, it is found that the poleward side of the surface westerlies has extended by 2^o while there is no significant change to its equatorward boundary. It follows that the width of the trades stay unaffected.

Regarding the strength of surface wind stress, the $x5O_3$ run has inherited the north-south asymmetry in the control run. For instance, even when averaged over 15 years, the peak surface stress at mid-latitude in the control run is $0.108Nm^{-2}$ in the SH, and is stronger than that in the NH by 5.6%. In addition to the effects of the Earth's elliptical orbit around the Sun, asymmetrical climatology profiles that were introduced in the early stage of development also account for the asymmetry (see section 4.3.4 for a discussion on this issue).

Despite the asymmetry, figure 3.1 shows that the zonal wind stress in $x5O_3$ has weakened at all latitudes. Using equation 1.31, we would expect the wind-driven Ekman transport to decrease as well. Since we are in an aquaplanet with zonally symmetrical flow in the ocean, we focus on the Ekman transport in the meridional direction.

3.1.2. Ekman Transport

For a given latitude, the poleward Ekman mass transport could be computed by multiplying equation 1.31 by the length of the corresponding latitude circle. To get the Ekman transport in Svedrup we multiply equation 1.31 by a factor of $1/\rho_o$, where ρ_o is the density of sea water. As we are only interested in meridional mass transport, we write out the y-component of the resultant equation, as shown in equation 3.1

$$\vec{v}_{ek} = -\frac{[\vec{\tau}_u]L_\lambda}{\rho_o f} \tag{3.1}$$

where $[\vec{\tau}_u]$ is the zonal mean zonal wind stress, L_λ is the length of a latitude circle in metres, f is the Coriolis parameter. $\vec{v}_{ek}$ is the total volume of water flowing across a latitude circle per unit time due to Ekman transport. The negative sign comes from the cross product expansion of equation 1.31.

In an aquaplanet where MOC is dominated by surface wind-stress and bottom friction, this quantity should be equal to the actual poleward transport of water in the surface Ekman layer. In order to test this idea we multiply

	Latitude	Control [Sv]	$x5O_3$ [Sv]	% Change
$\vec{v}_{Actual}$	10^o	52.061	42.425	-18.510
$\vec{v}_{ek}$	10^o	52.370	41.363	-21.018
$\vec{v}_{Actual}$	30^o	6.510	6.322	-2.890
$\vec{v}_{ek}$	30^o	7.362	7.062	-4.075
$\vec{v}_{Actual}$	50^o	-25.732	-21.410	-16.797
$\vec{v}_{ek}$	50^o	-22.787	-19.293	-15.335
$\vec{v}_{Actual}$	70^o	5.308	2.953	-44.374
$\vec{v}_{ek}$	70^o	3.919	2.359	-39.809

Table 3.1.: Comparison of $\vec{v}_{ek}$ and $\vec{v}_{Actual}$ at different latitudes in the NH. 3^{rd} and 4^{th} column shows their values in the control and $x5O_3$ run respectively. Positive (negative) values indicate poleward (equatorward) transport. 5^{th} column shows the % change of poleward transport after the ozone perturbation has been applied.

1.32 by $\frac{L_\lambda}{\rho_o}$ as before and extract its y-component, which gives us,

$$\vec{v}_{Actual} = \sum_{n=1}^{2} \vec{v}_o D_n L_\lambda \tag{3.2}$$

where $\vec{v}_o$ is the meridional component of the ocean current, and D_n is the depth of the n^{th} layer. Note we have replaced the integral in equation 1.32 by a summation because of the discrete levels in the model. By summing the quantity as shown in equation 3.2 for the top 2 layers of the ocean, which have been confirmed to be location of the Ekman layer in the model (not shown), we obtain the actual rate of poleward mass transport in the ocean.

Table 3.1 lists the values of $\vec{v}_{ek}$ and $\vec{v}_{Actual}$ at different latitudes. It is found that $\vec{v}_{Actual}$ and $\vec{v}_{ek}$ are almost the same at all latitudes in both runs, which also proves that Ekman transport is the only dominant mechanism in driving poleward transport at the surface layer. In our aquaplanet where the ocean MOC consists of bottom-reaching Ekman cells, the Ekman transport also governs the strength of the MOC. Let us now consider how $\vec{v}_{ek}$ responds to the applied ozone perturbation. Equation 3.1 states that the poleward Ekman transport is directly proportional to the zonal wind-stress.

Referring to figure 3.1 there is a weakening of surface winds at all latitudes and hence we expect the Ekman transport $\vec{v}_{ek}$ to slow down as well. This is indeed observed as evident in table 3.1. Regarding changes to the actual ocean mass transport $\vec{v}_{Actual}$, it is found to share the same story. In addition to a weakening of $\vec{v}_{Actual}$ everywhere in the aquaplanet, it is found that the imposed change on the actual mass transport is roughly the same as that on the Ekman transport. Despite the consistency, the strength of the change is location-dependent because of the factor $\frac{1}{f}$ in equation 3.1. For instance, the poleward mass transport in the Ekman layer is weakened by about $10Sv$ in the tropics. In contrast, at mid-latitudes Ekman transport has decreased by only $4Sv$, despite the greatest change in wind-stress as shown in figure 3.1.

3.1.3. Sea Surface Temperature

The global mean SST for both the control and $x5O_3$ run is plotted in figure 3.2. In both cases, the global mean SST is in the form of a non-uniform sinusoidal signal. As the quantity is averaged over the surface of the Earth, any internal asymmetries (e.g. cloud cover, ozone and CO_2 profiles) present in the model's climate system would have been accounted for. In fact, the non-uniform semi-annual cycle is due to the eccentricity of Earth's orbit around the sun.

The bottom panel of figure 3.2 shows the change in global mean SST with respect to time, after the ozone perturbation has been applied. It is found that surface layer in the $x5O_3$ run will be warmer than the control run by $0.4K$ at the end of year 1035. However, the rate of increase of SST is not linear over all 15 years. For instance, there is no clear sign of increase in global mean SST in the $x5O_3$ run until year 1024 from which there is a more noticeable increase of SST with respect to time. This is analogous to many previous double CO_2 experiments (e.g. [29, 52, 7]) where it takes years for the SST response to become notable. The actual length of the lag varies but is generally found to be on the order of years. Regarding the mechanisms responsible for the observed trend in our experiment, surface radiative effects are almost instantaneous and are out of the question. Considering the timescale involved, it is reasonable to assume the ocean plays a significant

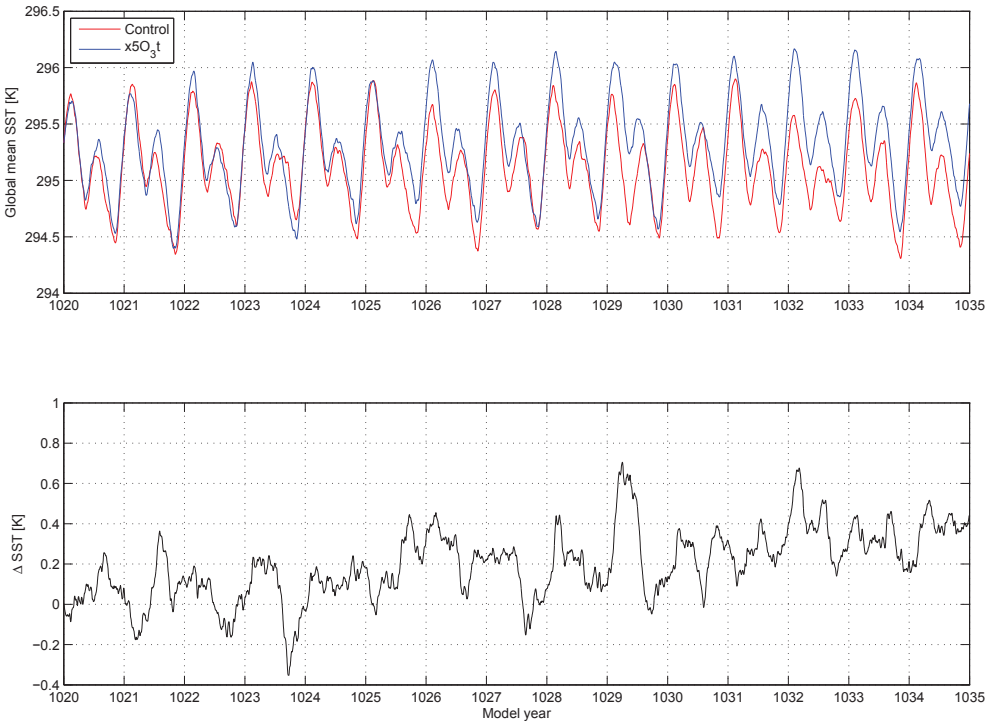


Figure 3.2.: Top: Time series of global mean SST for the control (red) and $x5O_3$ (blue) run, averaged over years 1020-1035 $[K]$. Bottom: Global mean SST anomalies ($x5O_3$-Control) $[K]$.

role in the increase in SST. In the following sections we will testify this is indeed the case.

3.2. Meridional Overturning Circulation

In section 2.5.2 we came across the idea that the MOC of our aquaplanet consists of deep-reaching Ekman cells, which are predominantly wind-driven. In section 3.1.1 and 3.1.2 we learnt that the surface wind-stress has weakened in response to an increase of ozone concentration in the stratosphere, which will also slow down the Ekman transport at the topmost layer of the ocean. Combining these findings and using simple continuity arguments, we expect the Ekman cells to weaken as well.

Figure 3.3 shows the change in MOC strength after the stratospheric ozone has been increased to 5 times its original value. A positive (negative) value indicates strengthening (weakening) of an Ekman cell that was originally flowing clockwise in the control run and weakening (strengthening) if it was overturning in the other direction. For instance, referring to figure 2.13, the tropical Ekman cell in the control run is anticyclonic in the Northern Hemisphere. A negative value in the corresponding latitude band in figure 3.3 suggests that the tropical MOC is weakening.

In fact, it is found that all of the six Ekman cells, depending on their locations, have weakened by about $10 - 30\%$ in response to an increase in stratospheric ozone. This is not a surprising result. In section 3.1.1 we confirmed surface poleward transport correspond to the magnitude of wind-driven Ekman transport, in which both of them have reduced in strength in the $x5O_3$ run. In an aquaplanet where the MOC is dominated by bottom-reaching Ekman cells, the return flow at the bottom branch of each Ekman cell must mirror the change the surface layer experiences. Otherwise, water will accumulate at the sites of divergence where Ekman pumping occurs, and is physically not possible.

In addition to weakening, there is also slight relocation of the cells. For instance, at 62^oN in figure 2.13 where the zero line is located, there is a divergence at the surface and deep water is sucked up to the surface by Ek-

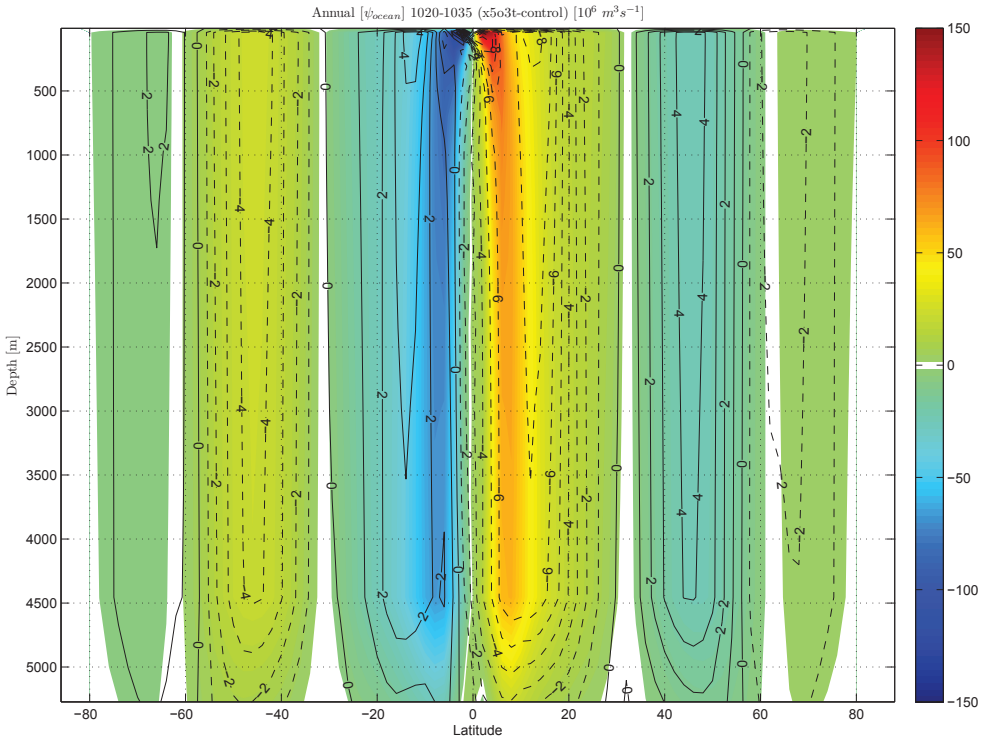


Figure 3.3.: Contour: MOC anomalies ($x5O_3$-Control), averaged over years 1020-1035 $[Sv]$. Contour interval $= 1Sv$. Control MOC is shown in color for reference.

man pumping. In the ΔMOC plot (figure 3.3) a zero line occurs at 56^oN, indicating there is the poleward side of the mid-latitude Ekman cell is extending towards the pole. This is in good agreement with the expansion of mid-latitude surface westerlies as described in section 3.1.1.

The change in MOC at mid-latitude and in response to increased ozone seems reasonably symmetrical over the hemispheres. In contrast, there is noticeable difference when the tropical Ekman cells are concerned. It is found that the surface flow in the tropical cell has weakened by $8Sv$ in the NH and only by $4Sv$ in the SH. In addition, the zero line in figure 3.3 does not overlap with the equator, and suggests that the equatorward-end of the tropical cell in the SH is strengthening and expanding across the equator. This is not expected as the only difference between the control and $x5O_3$ runs is the concentration of stratospheric ozone as shown in figure 2.3.

Nevertheless, the idea of weakened MOC due to reduced wind-stress at all latitudes in our aquaplanet is still valid and in the following we are going to explore the effects of decreased MOC to sea potential temperature.

3.3. Sea Potential Temperature

3.3.1. Global Mean

Figure 3.4 shows the global mean sea potential temperature as a function of time. In the control case, we observe a linear increase of $0.009K$ per decade, modulated with an annual cycle. This implies the aquaplanet is close but not exactly at its equilibrium. In contrast, the rate of increase in sea potential temperature in the $x5O_3$ is faster and is not as linear. The global mean sea potential temperature in the $x5O_3$ run is higher than that of the control run at the end of year 1035.

The bottom panel of figure 3.4 shows that during the first 180 days after the ozone is perturbed, the mean sea potential temperature, or equivalently, the heat content of the ocean is actually less than that of the control run. At the beginning of year 1020, the injection of ozone into the stratosphere implies increased ozone absorption of UV radiation. Hence, one expects a

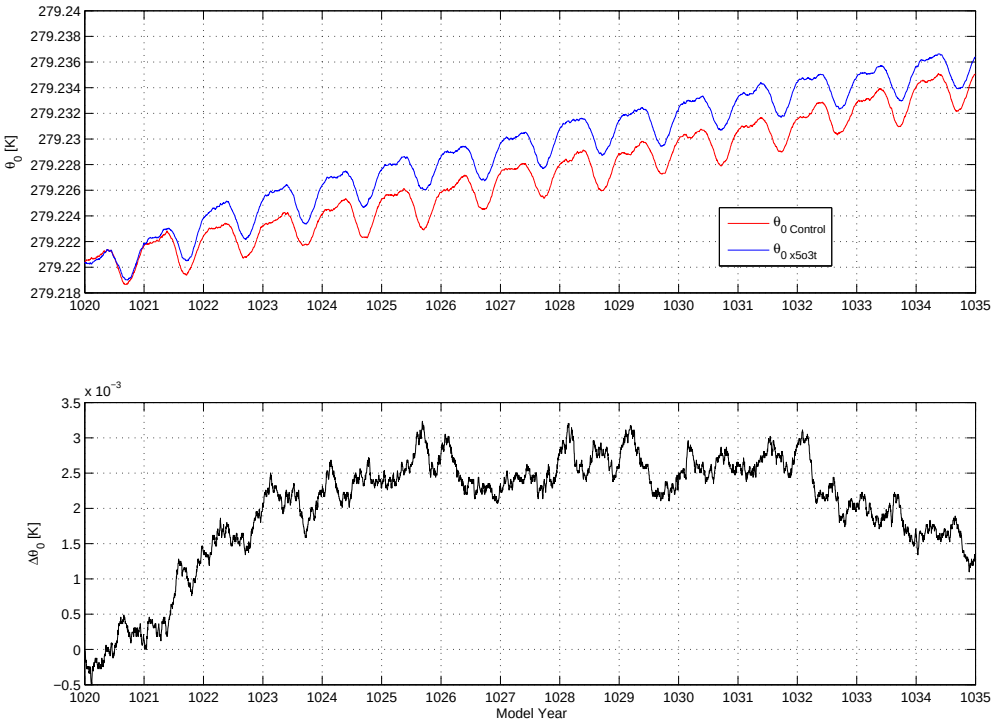


Figure 3.4.: Top panel: Global mean sea potential temperature for the control (red) and $x5O_3$ (blue) runs $[K]$. Bottom panel: Global mean sea potential temperature anomalies ($x5O_3$-Control)

reduction in SW and an enhanced LW flux from the stratosphere reaching the surface. During this period, it turns out that downward SW anomaly is $-7.567 W m^{-2}$ while the downward LW from enhanced ozone heating has only increased by $1.008 W m^{-2}$. Although this is partly balanced by the diminished upward latent heat flux due to the weakened wind stress, the net energy flux anomaly (SW + LW + sensible + latent) at the surface is still dominated by the SW and is found to be $-0.239 W m^{-2}$ when averaged over the first 180 days. This is equivalent to a drop of $0.0015 K$ in mean sea potential temperature and agrees well with figure 3.4 despite the low signal to noise ratio at the beginning of the experiment. As the anomalies develop with time, the signal to noise ratio increases to a maximum of $2 dB$, which indicates that the observed trend is significant. The global mean sea potential temperature continues to increase until year 1030, where the trend begins to go the opposite way. From the aspect of the ocean, this suggests a net loss of energy by the system at the TOA. For a detailed discussion, see sections 5.3.1 and 5.4.

Compared with the change in SST (figure 3.2), the fluctuation of the global mean sea potential temperature is smaller because the majority of ocean is isolated from the rapid-changing surface conditions. Regarding the magnitude of increase in temperature, the global mean is smaller that of the SST, by a factor of 100, due to the enormous heat capacity of the ocean.

3.3.2. Meridional and Vertical Structure

A zonal mean cross section of the sea potential temperature anomaly in the $x5O_3$ run is plotted in figure 3.5. Regarding SST changes, there is a rise of temperature at almost all latitude but poleward of 54^o. The time-averaged net downward heat flux anomaly over $55^o - 80^^o$ is found to be $-0.458 W m^{-2}$. Since the magnitude of MOC anomalies is small at these latitudes (figure 3.3), surface flux anomalies dominate and hence the observed cooling of the top $100 m$ of ocean.

The sea potential temperature anomaly peaks near the equator as would

been expected, with a peak magnitude of $0.575K$. Similar to the surface wind-stress anomalies, the tropical SST response is asymmetrical about the equator, with a slightly stronger increase in sea potential temperature in the NH than the SH.

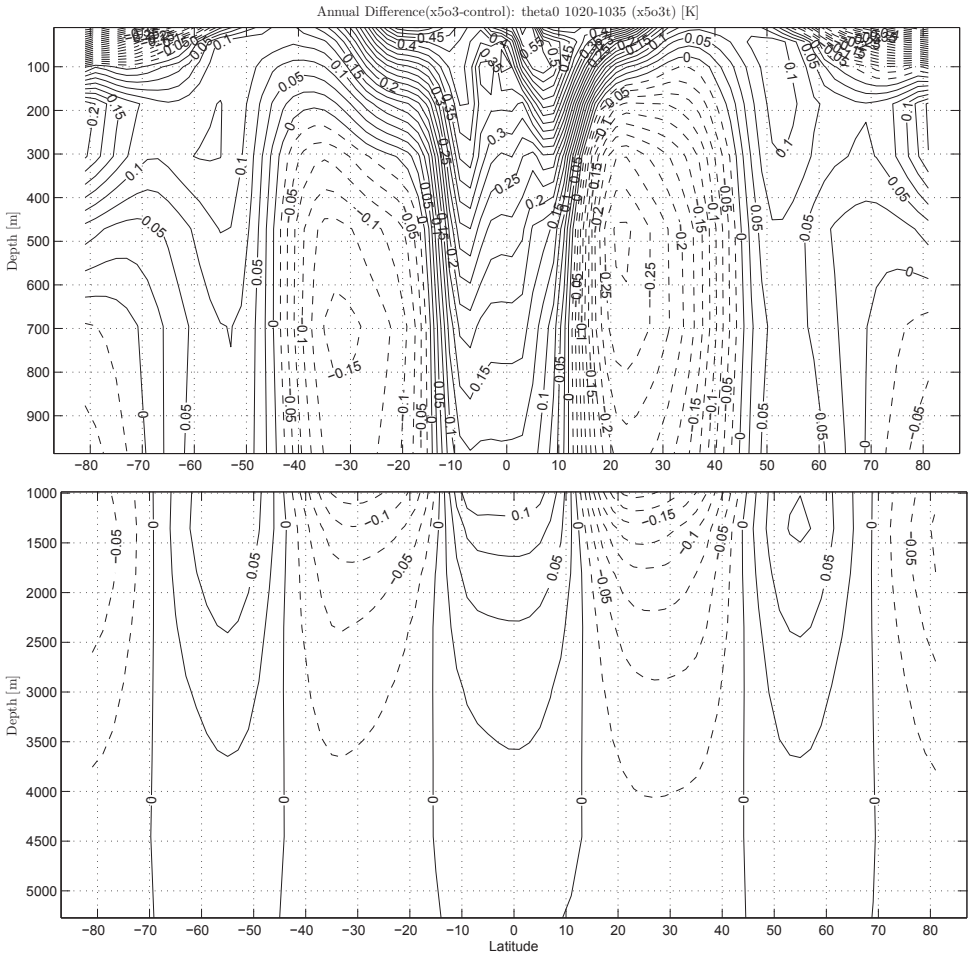


Figure 3.5.: Change in sea potential temperature for 0-1000m(top panel) and 1000-5000m (bottom panel), averaged over years 1020-1035 $[^oC]$. Contour interval = 0.025^oC.

Below the surface layer, the change in temperature shows a banded structure. The location of these bands of increasing (decreasing) temperatures coincide with the site of upwelling (downwelling) of water (see figure 2.13). For instance, at the equator where cold water from below the surface layer is

sucked up via Ekman pumping, there is an increase of sea potential temperature. Similarly, there is a decrease in temperature centered at the latitude (30^o) where the tropical and mid-latitude Ekman cells meet.

The observed changes to sea potential temperature is in fact not a coincidence but a direct consequence of the weakening of the MOC. In section 3.2 it is found that the all the Ekman cells have reduced in strength in response to weakened surface wind-stress. As a result, there is less exchange of heat between the surface and bottom of ocean by advection of water and hence the observed thermal structure. In section 3.4.2, we are going to show that this is indeed the case.

3.4. Redistribution of Ocean Heat Content

Despite the slight net warming of the ocean, we have illustrated that there is a temperature drop at various latitudes and depths due to weakening of the MOC. In this section we will focus on the redistribution of heat within the ocean and its mechanism.

3.4.1. Changes to Vertical Structure

We start by using equation 1.54 and integrate over the surface of the aquaplanet to obtain the global ocean heat content for each ocean layer in the model. Note that the variation of the total area with depth is neglected in the evaluation of equation 1.54 as the full depth of the ocean is only 0.09% of the radius of the Earth. The global ocean heat content for both the control and $x5O_3$ run are computed separately and their difference is plotted as a function of time in figure 3.6. Regarding the vertical structure of the ocean heat content, it is observed that the change is in the form of a dipole, which suggests heat transfer from the bottom of the ocean to the surface.

Warming is found to occur only at the top $200m$ of water in the first 180 days since the applied ozone perturbation, which then extends to a maximum depth of $550m$. After four years, the boundary of the dipole is observed to retract towards the surface, and reaches the $400m$ level at the end of the simulation. Even though there is a net increase in global mean sea potential

temperature, warming only applies to top layers of the model but not to water below. The main site of heat content loss is found to centerd at $900m$.

3.4.2. Mechanism

In section 3.3.2 we made the hypothesis that the change in sea potential temperature at different latitudes and depths is due to the weakening of the Ekman cells, based on the fact that the location of maximum warming (cooling) coincide with the site of upwelling (downwelling) of water. To prove this is indeed the case we need to compute the change of heat content of a layer of water due to vertical advection.

Consider a slab ocean with area ($\delta x \times \delta y$) as shown in figure 3.7. It is bounded by the n^{th} and $(n+1)^{th}$ model level and has a thickness of δz. The top and the bottom boundary of the layer each has a different set of temperature θ and vertical current velocity w. Assuming there is no net zonal and meridional current, the only advection term that contributes to its heat content is the vertical advection of temperature. The above statement is valid in our analysis as we are considering the global ocean heat content. The rate of change of heat content $\frac{dU_{adv}}{dt}$ of this slab ocean is then given by,

$$\frac{dU_{adv}}{dt} = \rho_{slab} c_{po} \big[w_n \theta_n - w_{n+1} \theta_{n+1} \big] \delta x \delta y \tag{3.3}$$

where ρ_{slab} is the density of the slab and c_{po} is the specific heat of sea water under constant pressure. Let $\theta_{n+1} > \theta_n$ upward be positive so that $w_{n+1} > w_n$. From equation 3.3 there will net energy removed from this slab of ocean by advection.

Since we are interested in vertical transfer of heat by advection, we simplify the problem by integrating the quantity over the surface of the aquaplanet. In doing so, the assumption of zero net zonal and meridional current becomes valid due to conversation of mass. A more general form of equation 3.3 is given by:

$$\frac{dU_{adv}}{dt} = \iint \rho_{slab} c_{po} \Delta_z [w\theta] dx dy \tag{3.4}$$

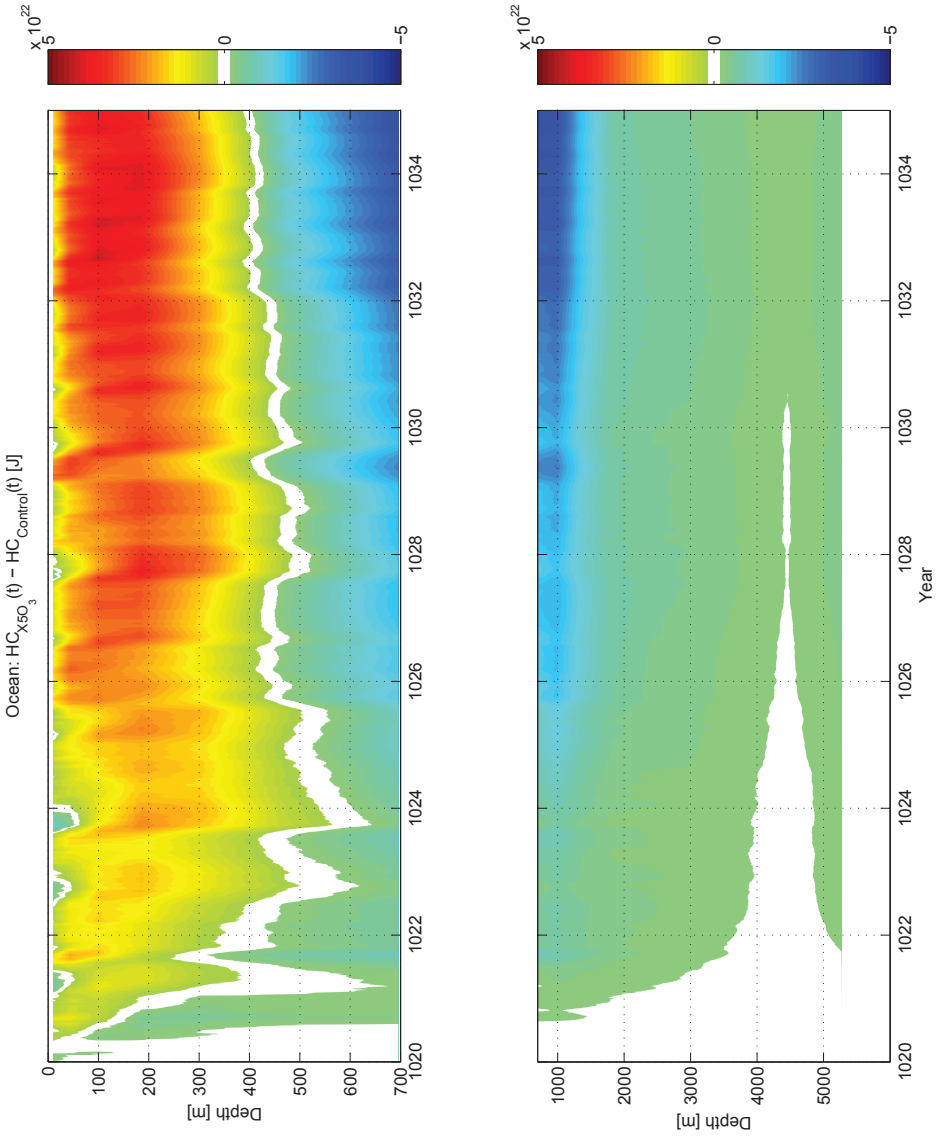


Figure 3.6.: Time series of change in ocean heat content, after a perturbation of 5 times O_3 has been applied at model year 1020. $[J]$.

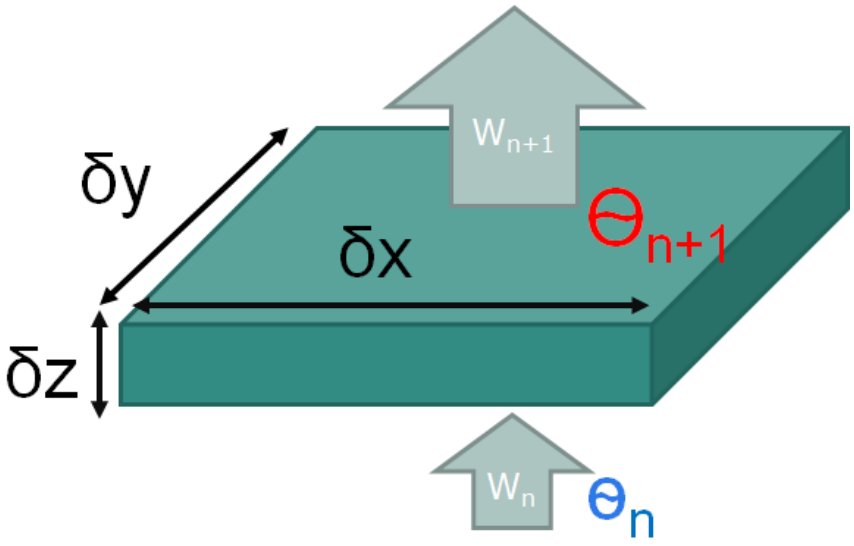


Figure 3.7.: Schematic of a slab of ocean.

For each layer in the ocean, we compute $\frac{dU_{adv}}{dt}$ and integrate with respect to time so that it can be compared with figure 3.6, which shows the actual change in ocean heat content observed in the model.

Figure 3.8 shows the heat content change for each layer in J due to vertical advection of temperature, after the ozone perturbation has been applied. At first sight it is found that the structure of figure 3.8 is very similar to the actual change in ocean heat content as shown in figure 3.6. Despite the top two layers where there is a dipole of heat content change, there is a clear sign of partitioning of heat content change between the top $450m$ and the water below. This confirms that the change in vertical structure of ocean heat content in response to a $\times 5$ ozone concentration is predominantly contributed by reduced vertical advection of temperature, and is a consequence of the weakened surface wind-stresses.

Regarding the surface dipole, considering the following. At latitudes where Ekman pumping occurs (i.e. 30^o), surface water that is light and warm is forced down and away from the surface. In contrast, at equator and 62^o, Ekman suction transfer cold and dense water up from the depths of the

ocean. The net effect of the two processes is that the wind-driven circulation tilts the isopycnals, building potential energy in the process. This is baroclinically unstable and the stored energy is released through the generation of ocean eddies. These eddies drive an opposing circulation that tends to reverse the tilting of the isopycnals by Ekman pumping/suction [43] and is parametrised in FORTE [15]. In real world scenarios, the heat transport by these ocean eddies is relatively unimportant at latitudes where the ocean is confined zonally by continents. However, at the latitudes where the Antarctic Circumpolar Current (ACC) is found, there is no land to support western boundary flow and meridional heat transport and these baroclinic eddies play a key role in ocean heat transport [44]. The ACC is analogous to our aquaplanet, where there is no land except for the polar cap. Referring to equation 3.4, we have only accounted for the vertical advection of temperature by the wind-driven mean circulation, neglecting that by the opposing eddy-induced circulation and also by the surface mixed layer parametrisation scheme in FORTE. In fact, the latter is more likely to be responsible for the dipole as the eddy parametrisation scheme in FORTE [15] is mainly important outside the mixed layer. However, ocean heat transport where there is no zonal confinement of the sea is not well developed and we should not rule out the possibility that eddy parametrisation is at least partly responsible for the observed dipole without further testing. Although the exact reason for the dipole is beyond the scope of this study, it can be deduced that the surface dipole will vanish when these modes of vertical heat transport are also considered.

In addition to the surface dipole, there are other notable differences between figure 3.8 and 3.6. Consider the depths $600m$ and $1300m$ where there is a significant decrease in heat content. The depths at which this occurs is fairly localised in depth. The contribution from depths below $1300m$ remain negligible throughout the period the ozone perturbation is applied. This is not true with the heat content change due to vertical advection of temperature. The lower boundary of the site of major heat loss varies strongly with time and have extended downwards by about $1300m$ in the last 5 years of simulation.

The discrepancies below the surface layer can also be explained by consid-

ering the other advection terms that contribute to the heat content change. As mentioned before, we have neglected vertical heat transport by eddies as equation 3.4 only accounts for large scale advection. Since the eddy parameterisation [16] in the model tends to oppose the effect of large scale flow, the magnitude of vertical heat transport by large scale processes in figure 3.8 is consistently larger than that of the actual heat content change (figure 3.6).

Regarding the surface dipole in figure 3.8, we take a step further and consider the first 5 layers in the model (top $300m$) as the topmost layer. The heat content change due to vertical advection by large scale flow is averaged over the top 5 layers and re-plotted in figure 3.9 for reference. Although information on how the heat is redistributed within the top $300m$ is lost, figure 3.9 now resembles the actual heat content change (figure 3.6) better.

3.5. Summary and conclusions

The introduction of a dynamic ocean to an atmospheric model that relies on prescribed surface fields increases the degrees of freedom of the system. In the context of ST coupling studies, we aim to determine whether ocean feedbacks play a significant role. This can not be achieved without having an understanding on the processes that are important in the ocean of an aquaplanet. The purpose of this chapter is therefore to demonstrate how the ocean respond to a perturbation of 5 times ozone in the stratosphere and the corresponding mechanisms. In an aquaplanet where there is no continent to support zonal flow, wind-driven circulation is dominant and we find the following change after the ozone has been increased:

- The surface Ekman transport has weakened in response to reduced surface windstress at all latitudes.
- Since the MOC of the aquaplanet consists of bottom-reaching Ekman cells and are strongly dependant on surface winds, the strength of MOC has also weakened.
- As the MOC weakens, the time needed for bottom water to return to the surface is longer. In other words, there is less cold water coming

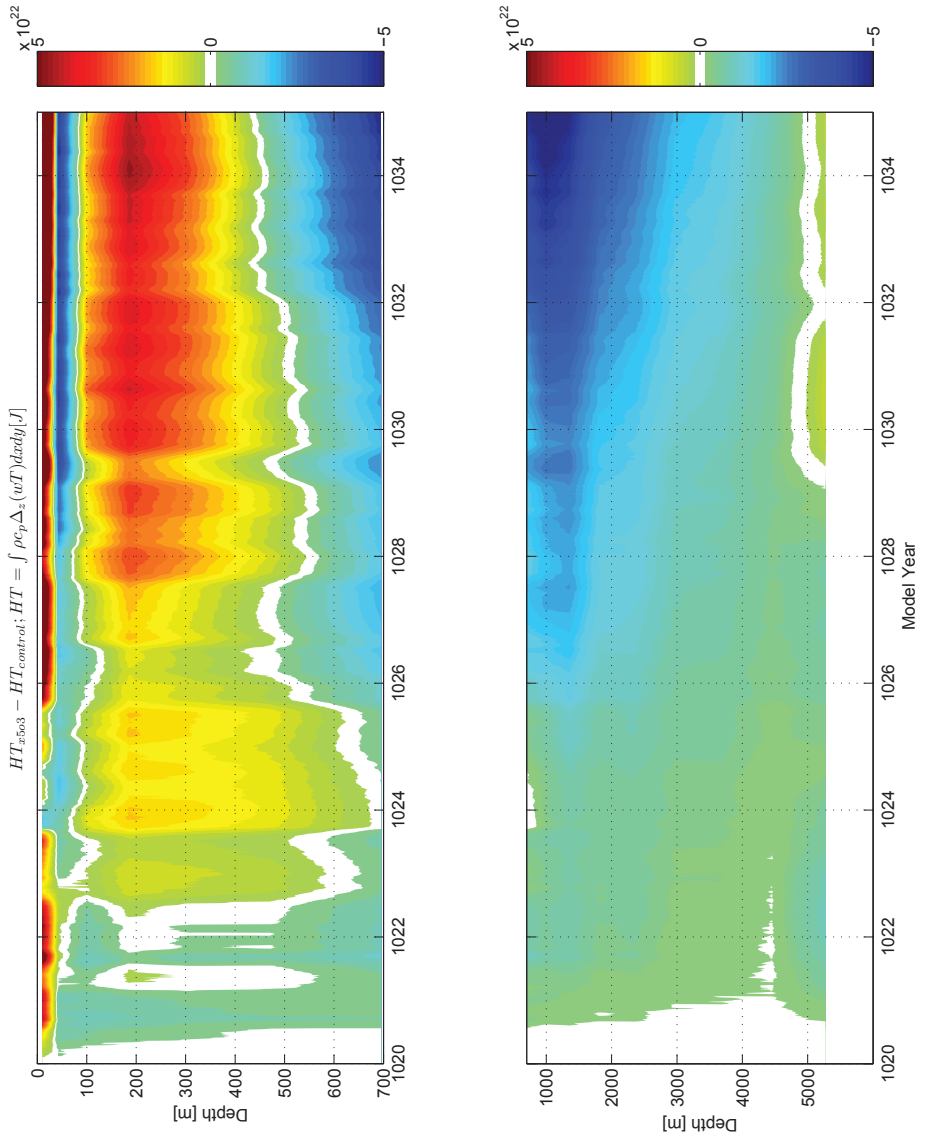


Figure 3.8.: Time series of change in ocean heat content due to vertical advection, after a perturbation of 5 times O_3 has been applied at model year 1020. $[J]$.

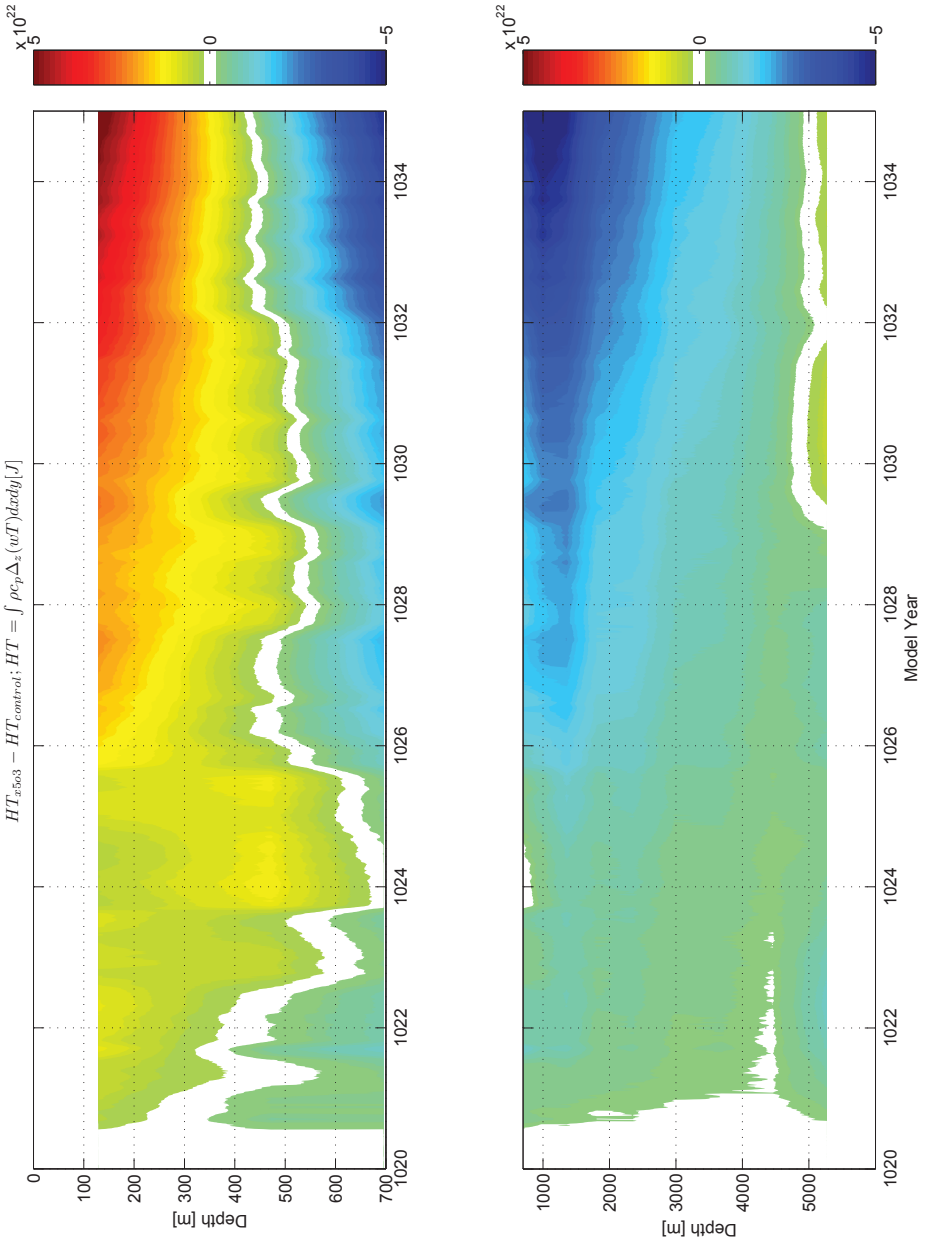


Figure 3.9.: Same as figure 3.9, but with the model levels within the top $300m$ taken as a single layer.

from the deep ocean per unit time. Similar arguments apply to warm surface water.

- The sea surface temperature has increased at all latitudes except for polar regions, where there is a polar cap. There is net gain in heat at the top $400m$ of the ocean, which is largely contributed by the water below.

- Vertical advection of temperature by large scale flow is mainly responsible for the change in ocean heat content structure.

In summary, the ocean has made both thermal and dynamical adjustments in response to the ozone perturbation, both of which is a consequence of reduced wind-stress.

4. Results: Atmosphere

By performing multiple linear regression analysis on zonal wind data from from National Centers for Environmental Prediction-National Center for Atmospheric Research (NCEP-NCAR) reanalysis dataset, it is shown by HBD05 that the 11-year solar cycle is associated with changes in the observed zonal wind field. The results indicate that during periods of maximum solar activity, there is a weakening and poleward shift of the subtropical jets.

Similar adjustments to the tropospheric circulation in response to a forcing that originates from outside the troposphere has been observed and confirmed in numerous GCM studies. For instance, Haigh [20] simulated changes in solar irradiance and stratospheric ozone over the 11-year solar cycle and showed that warming of the summer stratosphere at solar maximum would weaken and shift the subtropical jets poleward. Other GCM studies involve applying a direct thermal perturbation to the stratosphere [22, 50, 56, 68] which achieved qualitatively similar results.

Although the models and techniques these GCM studies use vary, the conclusion is that generic heating/cooling of the lower stratosphere is capable of inducing adjustments in the subtropical jets and meridional circulation in the troposphere. The direction and magnitude of the change depends on the latitudinal structure of the applied thermal forcing in the stratosphere [22].

Although advances in understanding have been made in the mechanism whereby how the stratosphere regulates the tropospheric circulation [56], the GCM studies considered do not have ocean dynamics built-in. It is therefore ambiguous whether SST feedbacks play a significant role in modulating changes in tropospheric dynamics that originates from from the

stratosphere.

Previously in chapter 3, we have demonstrated that in response to increased O_3 how MOC in the ocean respond to reduced surface windstress, and its consequential impact to the vertical structure of ocean heat content. It is also found that the the global mean SST has increased. In order to isolate the effects of these ocean feedbacks in the atmospheric response, we perform a second experiment, in which stratospheric ozone is increased by 5 times as in the $x5O_3$ run, but the SST is kept fixed at all times. This is referred to as $x5O_{3FSST}$ in the following. The chosen SST profile is taken from year 1019 of the control run (i.e. the year before the ozone perturbation is applied) instead of standard SST profiles. This is to make sure the only difference between the two ozone experiments is the absence of an interactive ocean and hence eliminates unwanted SST forcings.

In this chapter we will first discuss both the zonal wind fields and meridional circulation in the troposphere in both the $x5O_3$ and $x5O_{3FSST}$ runs. This will be followed by an analysis on the momentum budget in the atmosphere, with particular focus on the poleward transfer of zonal momentum by eddies. We will also provide possible explanations to the asymmetries observed in various aspects in our aquaplanet simulations.

4.1. Zonal Wind

The perturbations in zonal mean zonal wind in response to increased stratospheric ozone is presented in figure 4.1. Note in each of the experiments, we have doubled the amount of data by averaging zonal wind over the two hemispheres.

In both cases, the zonal wind changes show a banded structure (see figure 4.3), and agree qualitatively with that observed by HBD05. In the $x5O_3$ run, there appears a band of weakening near 43^o and a tilted band of stronger zonal wind near 25^o. This represents an equatorward shift and weakening of the jet. It is also evident that the core of the jet has shifted down towards the surface. This is consistent with the intense stratospheric heating caused by increased ozone absorption, which has pushed the ther-

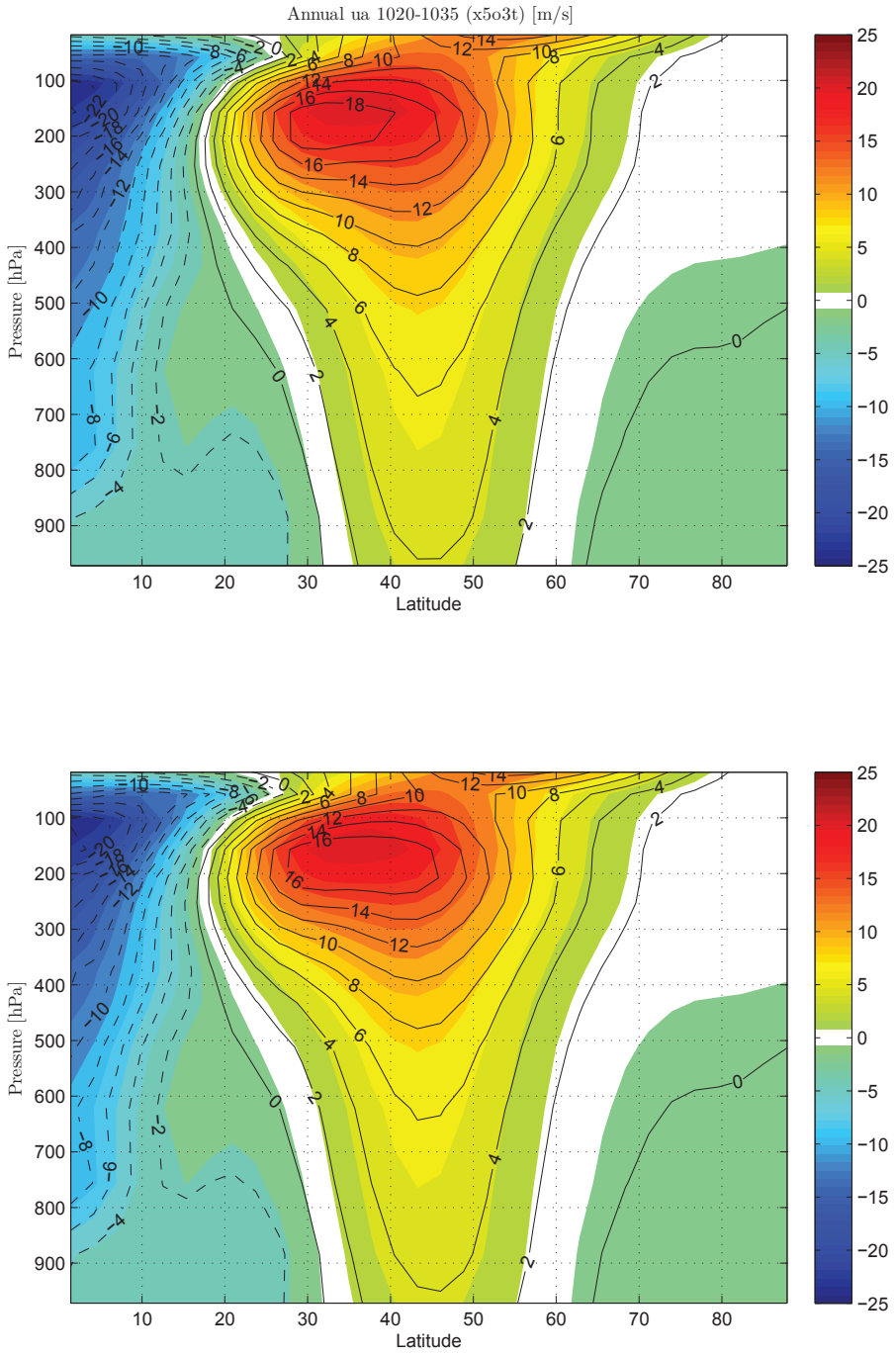


Figure 4.1.: Black contours: Zonal mean zonal wind for $x5O_3$ (top) and $x5O_{3FSST}$ (Bottom). Colored contour plot shows the control zonal wind field for comparison $[ms^{-1}]$.

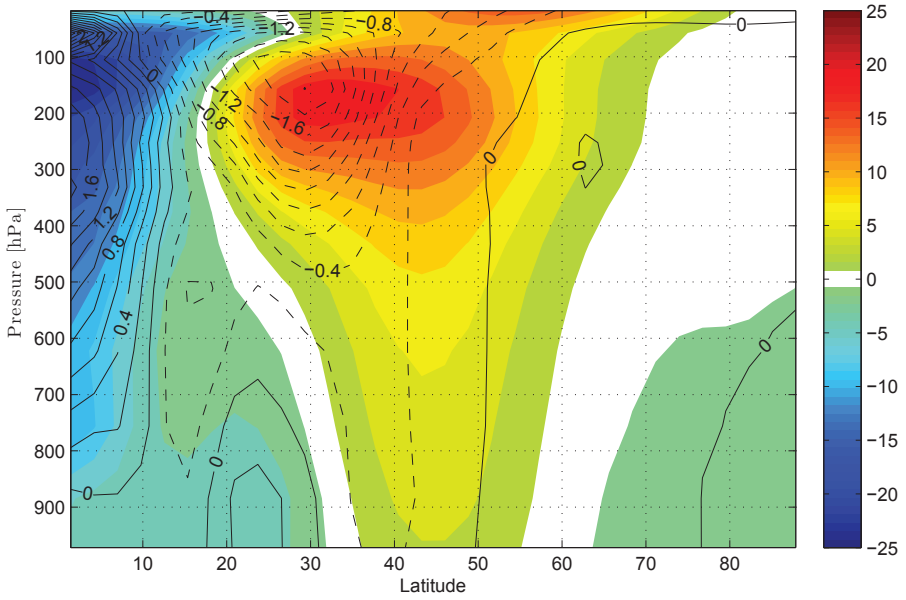


Figure 4.2.: Black contours: Difference in zonal mean zonal wind between the two ozone experiments ($x5O_{3FSST}$ - $x5O_3$). Colored contour plot shows the $x5O_3$ zonal wind field for reference $[ms^{-1}]$.

mal tropopause down. Despite the equatorward shift of the core of the jet, a slight expansion on its poleward flank is also observed.

As in the $x5O_3$ case, it is observed that there is also a weakening of the jet-stream in the $x5O_{3FSST}$ run, but of a slightly greater reduction in magnitude. The core of the jet has reduced from a control value of $21.40ms^{-1}$ to $19.89ms^{-1}$ in the $x5O_3$ run and $18.00ms^{-1}$ in the $x5O_{3FSST}$ respectively. On the other hand, the extent of the equatorward shift of the jet is comparatively weaker in the $x5O_{3FSST}$ run, as shown in figures 4.1 and 4.2.

Concerning the equatorial easterlies, these are weakened throughout the troposphere in the $x5O_{3FSST}$ run, and are fairly uniform over the latitudes concerned. This is not true in the case where there is an interactive ocean present ($x5O_3$). The top panel of figure 4.3 shows a positive band that is tilted towards the equator as it approaches the surface. In addition, despite a weakening and shrinking, it is observed that the core of the easterlies $(200 - 300hPa)$ has actually strengthened in response to increased ozone concentration when an interactive ocean is present.

4.2. Meridional Circulation

In this section we seek find out to what extent the injection of ozone affects the meridional circulation in the atmosphere. As in the zonal wind sections, we take the average of the meridional wind field of both hemispheres and integrate vertically to get the mass streamfunction ψ_a for the atmosphere,

$$\psi_a = L_\lambda \int_{Surf}^{TOA} v\rho_a dz \tag{4.1}$$

where v is the meridional wind field, L_λ is the length of a latitude circle, ρ_a is the density of air. Using the hydrostatic balance equation 1.28, we can rewrite ψ_a in pressure coordinates, as shown in equation 4.2,

$$\psi_a = -\frac{L_\lambda}{g}\int_{p_s}^{0} vdP = \frac{L_\lambda p_s}{g}\int_0^1 vd\sigma \tag{4.2}$$

where the last term is converted to σ coordinate since FORTE uses σ level as its vertical coordinate. Note p_s is a function of longitude and latitude but

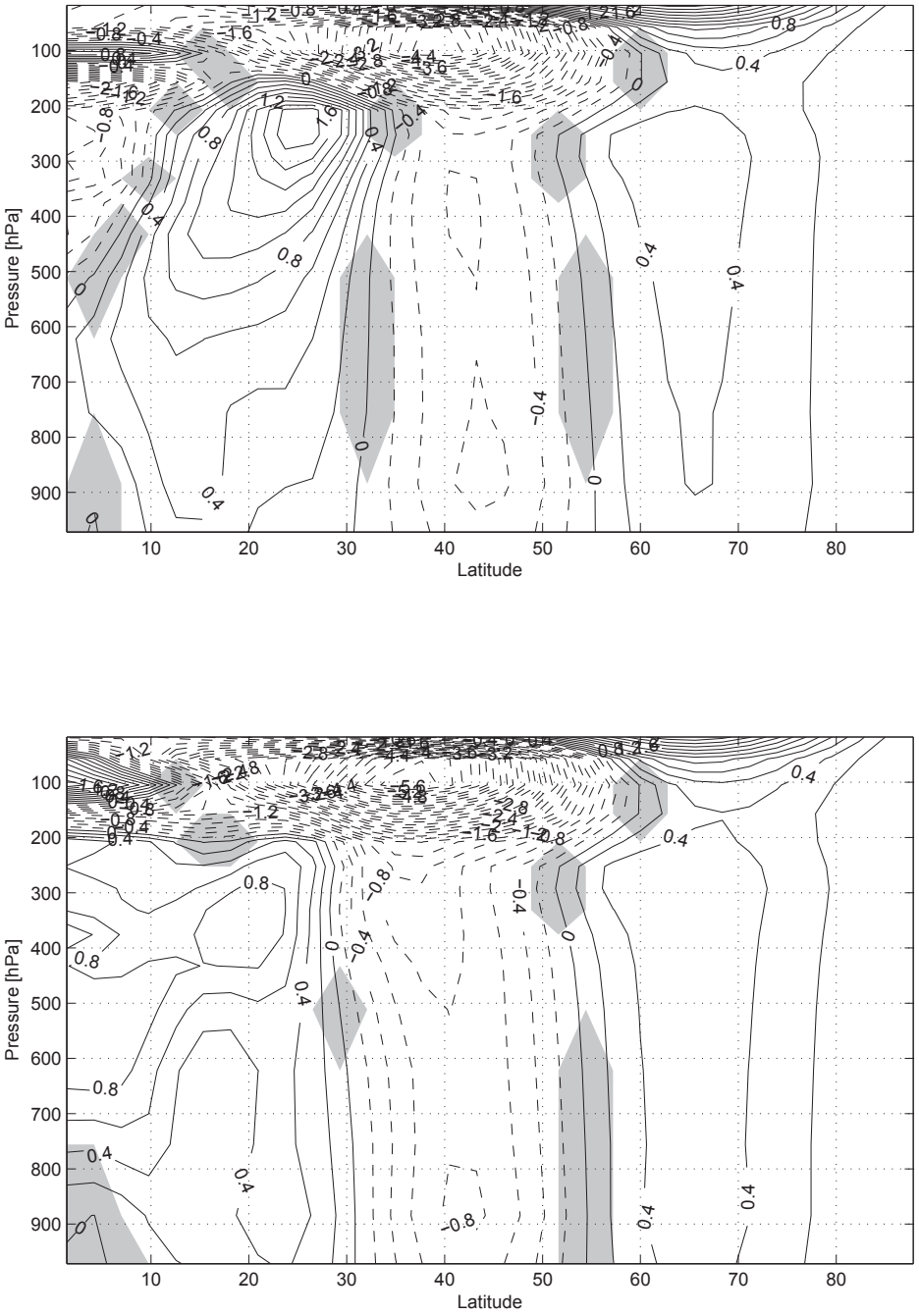


Figure 4.3.: Change in zonal mean zonal wind for $x5O_3$ (top) and $x5O_{3FSST}$ (bottom) $[ms^{-1}]$.

it is found that the spatial variation in surface pressure in our aquaplanet is small enough to assume the surface pressure is constant ($1000hPa$) for every grid point. Hence, for simplicity, we assume a constant surface pressure in the following.

The coloured plot in figure 4.4 shows the mass streamfunction of the atmosphere in the control run, in which we can identify the locations of the 'inverted' cell, Hadley cell and Ferrel cell as mentioned in section 2.5. It is identical to figure 2.9, except that meridional wind data from the two hemispheres are now averaged and plotted on a single hemisphere. In addition to having doubled the amount of data available, there is another good reason for doing this in our analysis of atmospheric meridional circulation. For instance, the control NH and SH Hadley cells as shown in figure 2.9 are not as identical as one expects from an idealised aquaplanet. By taking an average over the two hemispheres we can focus on their responses to the applied perturbation, and neglect the small discrepancies between the two hemispheres.

Changes in ψ_a in the $x5O_3$ run are shown by the contours in the top panel of figure 4.4. It is observed that, there is a negative band at 23^o flanked by two positive bands, one around 8^o and the other 42^o. This implies all of the 'inverted', Hadley and Ferrel cells have weakened since the injection of stratospheric ozone.

Despite a reduction in the strengths of the cells, the bands in figure 4.4 are not aligned perfectly with the location of the cells in the control run, which suggests shifting. It is found that the Hadley cell has slightly shifted equatorward, and hence shrinking the size of the 'inverted' cell. Similarly, there is also a sign of the Ferrel cell extending equatorward into the Hadley cell.

All of the three cells are also found to have decreased in height. This is expected as in the explanation of the downward shifting of the core of the jets, which is also due to a lower thermal tropopause.

In the case of the $x5O_{3FSST}$ run in which the SST is fixed, all of the merid-

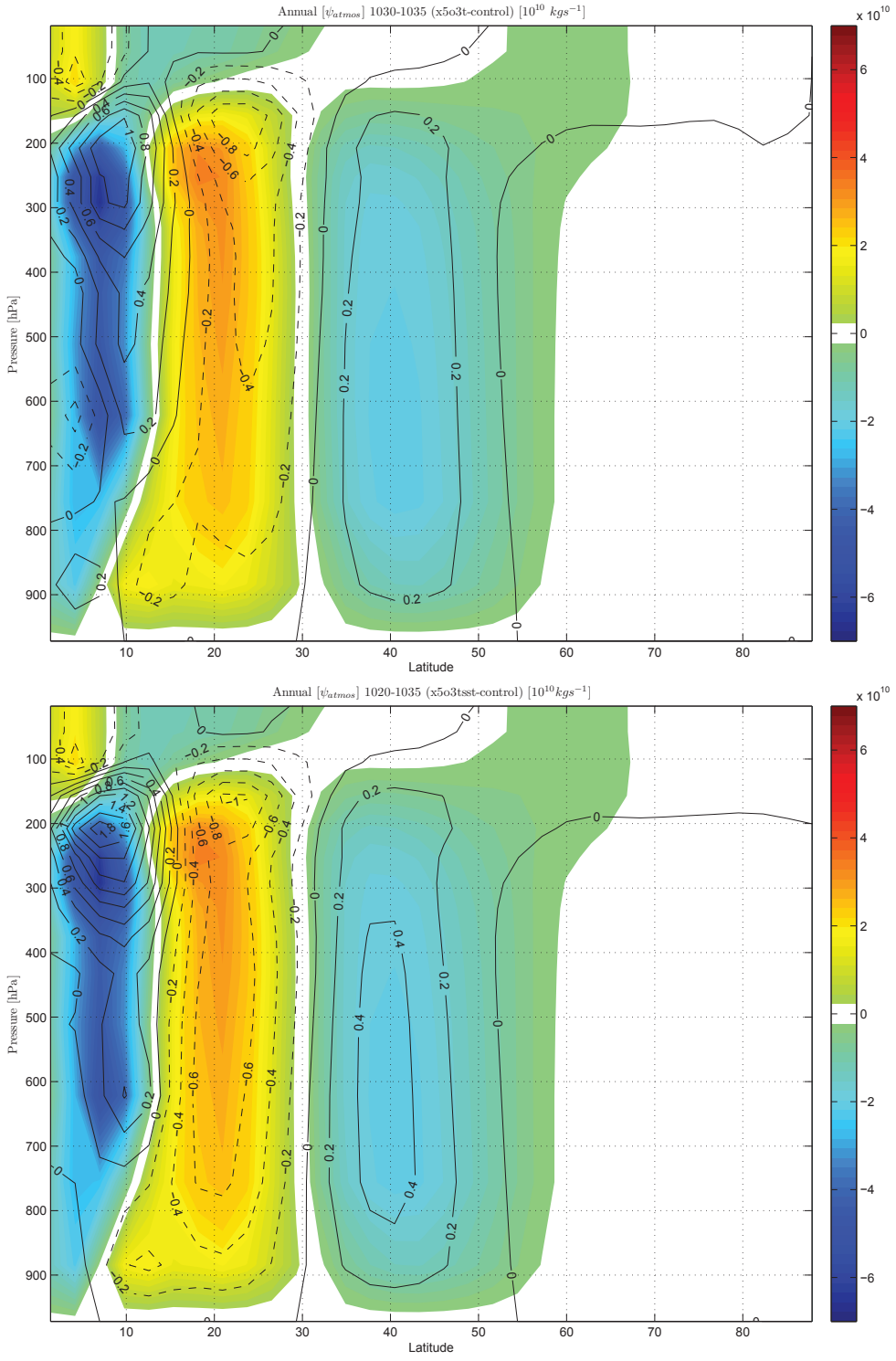


Figure 4.4.: Change in atmospheric mass streamfunction for $x5O_3$ (top) and $x5O_{3FSST}$ (bottom) runs. The control is plotted in color in the background for reference. $[10^{10}kgs^{-1}]$. Contour intervals are $0.2 \times 10^{10}kgs^{-1}$ in all cases

ional cells have also weakened, but to a greater extent, compared to the $x5O_3$ run. In section 3.2 we showed that how heat content of the top $700m$ of ocean had increased. A warmer SST in the $x5O_3$ run encourages advection of air, and hence opposes the effect of weakening of each meridional cell in the atmosphere expected from the stratospheric ozone perturbation. Hence, a less pronounced weakening of the meridional cells in the atmosphere is observed in the $x5O_3$ run.

The extent of equatorward shifting of each individual cell is not as significant as in the case where an interactive ocean is present. For example, the zero line in $x5O_{3FSST}$ (lower panel, figure 4.4) follows the rising portion of the Hadley cell from $700hPa$ to $400hPa$ while this is not the case in $x5O_3$ (upper panel, figure 4.4). This can be understood by considering the upwelling of air near the tropics. Extensive solar heating at the equator creates a region of warm SST, which causes advection of air above the surface in this region. Fixing the SST in the $x5O_{3FSST}$ run constraints the location where upwelling of air occurs. Hence, the shifting of the Hadley cell in the $x5O_{3FSST}$ run is not as distinct as that in the $x5O_3$ run. Finally, the height of each of the cells have decreased as in the $x5O_3$ case for the same reason.

4.3. Transient Eddy Momentum Fluxes

4.3.1. Decomposition of the Circulation

Although large scale circulations in the atmosphere show a certain level of constancy, many of the fields that characterise the state of the atmosphere are transient by nature. Hence, these fields exhibit anomalies that vary with time and space. Before we provide an analysis on the role of spatial eddies on zonal wind accelerations in the way as shown in equation 1.18, let us examine the structure of zonal momentum fluxes carried by transient eddies in our aquaplanet.

Instead of decomposing the wind fields into its zonal mean flow and zonally asymmetric flow as in equation 1.15, we can also expand the instantaneous wind field as a sum of its time mean and its instantaneous fluctuation from

the time mean flow. For example, in the case of u,

$$u = \overline{u} + u' \tag{4.3}$$

where the overbar represents time average of the quantity concerned and $'$ denotes the temporal deviation from it.

The third term on the left hand side of 1.14 represents the gradient of northward transport of zonal momentum by all modes of transport. If we decompose the term uv using equation 4.3 we get,

$$\overline{uv} = \bar{u}\bar{v} + \overline{u'v'} \tag{4.4}$$

we then apply the operator as shown in equation 1.15, so that equation 4.4 becomes,

$$[\overline{uv}] = [\bar{u}][\bar{v}] + [\bar{u^*}\bar{v^*}] + [\overline{u'v'}] \tag{4.5}$$

where the total northward transport of zonal momentum flux $[\overline{uv}]$ is decomposed to three different contributing terms, namely the mean meridional circulation, the stationary eddies and the transient eddies respectively [48].

The results of HBD05 suggests a thermal perturbation in the lower stratosphere will result in a dynamical response in the troposphere, in which eddy feedbacks play a primary role. Considering the fact that the poleward transfer of momentum is dominated by the transient eddies [48], in the following, we will focus on the last term of 4.5. As a side note, the second term on the right hand side of equation 4.5 is unimportant in our aquaplanet as the idealised topography does not support Rossby wave forcing.

4.3.2. Meridional Structure

The goal of this subsection is to provide an overview of the meridional structure of eddy momentum transport. For this purpose, the $[\overline{u'v'}]$ term in equation 4.5 has been computed for the control run and plotted in figure 4.5.

Eddy momentum transport maximises at around $150hPa$ and 30^o in both hemispheres and coincides with the latitudes at which the jet streams peak.

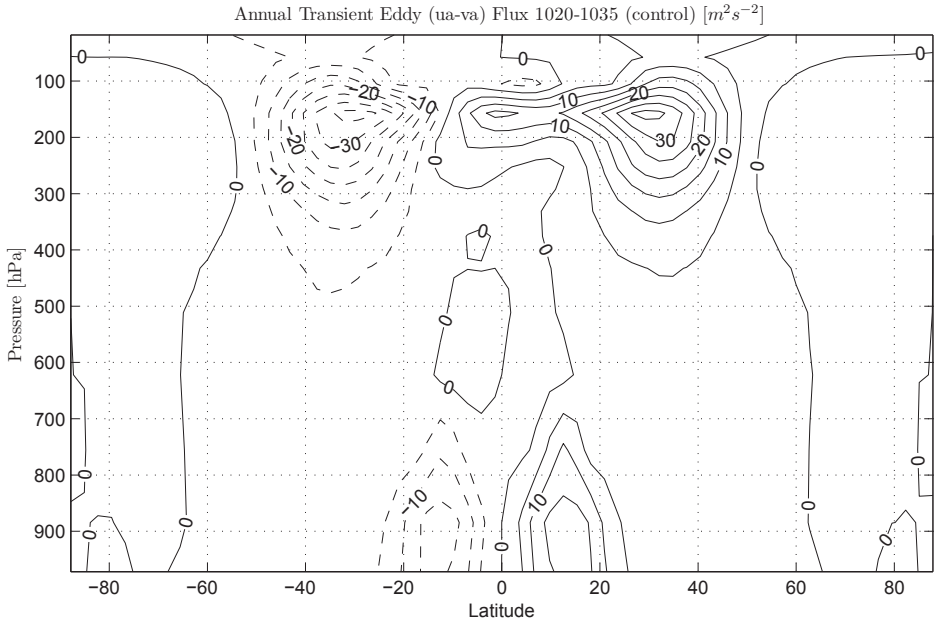


Figure 4.5.: Northward transport of momentum flux by transient eddies for the control run $[m^2s^{-2}]$. Contour intervals are $5m^2s^{-2}$.

This is expected as the jet stream meanders does not flow along a single latitude circle. Instead, the eastward-propagating jet stream meanders due to baroclinic instability. Hence, the subtropical jet exhibits a structure as shown in figure 4.5 which shows eddy transport of zonal momentum poleward, peaking at $150hPa$ and 30^o in latitude.

At the tropics, there is a local maximum of poleward momentum transport by transient eddies centred at about 15^o and stretches from the surface to the $700hPa$ level in both hemispheres. The observed up-gradient of momentum flux on the equatorward flank of this region is responsible for the strong surface easterlies near the equator as shown previously in figure 2.7.

Over the equator, there is a local maxima situated at the same pressure level as the jet streams, which suggests a transport of zonal momentum from the SH to the NH. The magnitude is also significant compared to that of the subtropical jets. This asymmetrical flow of zonal momentum is unexpected in an idealised configuration like an aquaplanet. As the quantity

$[\overline{u'v'}]$ concerns transient eddies, figure 4.5 shows that there are consistent instantaneous fluctuations of the zonal mean circulation at the tropics. It also suggests that the form of the equatorial mean flow is similar to that of the mid-latitude jets.

4.3.3. Wavenumber Analysis

We have learnt that there are wave activities in both tropical and subtropical regions in our aquaplanet. In real world scenarios, the subtropical jet stream usually consists of $4-6$ meanders. In this subsection we aim to provide a more comprehensive description of the waves found in the model.

Mathematically, any periodic signal can be decomposed as a sum of its constituent frequencies. Consider the zonal and meridional wind fields along a latitude circle at a specific time t. Here the wind field is regarded as a function of longitude and is in the space domain. It is then possible for one to isolate the each of the wind signals that corresponds to a specific spatial frequency (or wavenumber k, defined as the number of cycles within a latitude circle).

To achieve this we perform a Fourier analysis on both the zonal and meridional wind fields to extract the signals that correspond to a specific wavenumber. Using these signals, we compute $[\overline{u'v'}]$ to determine how much each wavenumber component contributes to the total transient eddy transport.

For reference the same analysis is performed on zonal and meridional wind fields from the National Centers for Environmental Prediction (NCEP) and the National Center for Atmospheric Research (NCAR) reanalysis dataset. The corresponding analysis is plotted in figure 4.7.

In the winter hemisphere, it is observed that there is a signal of poleward momentum transfer corresponding to wavenumber 4-7 in the NCEP-NCAR analysis. This is expected as this corresponds to the eddy transport by sub-tropical Rossby waves. In the case of our aquaplanet, a corresponding eddy transport that is of the same order of magnitude is found at the same location (figure 4.6). This suggests that the eddy momentum transfer by the

jet stream is comparable to that of the real world in the winter hemisphere. In the summer hemisphere, the eddy forcing ($k = 4 - 7$) at mid-latitudes in our aquaplanet is found to be much weaker than that obtained using NCEP-NCAR data.

At low wavenumbers (k=0-3), a negative flux is found at the equator in our aquaplanet, which implies southward transport of momentum across the equator. The situation in JJA is reversed (not shown) and is larger in magnitude such that the net effect is an asymmetrical flow of eddy momentum flux from the SH to the NH in the annual mean (see figure 4.5).

By definition wavenumber 0 is the zonal mean flow and the related eddy transport can not take the form shown in figure 1.7. Instead, it suggests that the zonal mean flow is fluctuates with time. In the NCEP-NCAR plot such a feature at $k = 0$ is not observed.

The equatorial eddy momentum transfer persists for $k = 1 - 3$ in our experiment, which suggests that the easterlies in our aquaplanet takes the form of a Rossby wave and varies from a single to a maximum of three meanders round the equator.

4.3.4. Origin of the Equatorial Transient Eddies

Despite the form of the circulation that correspond to the asymmetrical flow of transient eddy momentum across the equator is now made clear, its origin remains unknown. Although both the strong easterlies and the 'inverted' cell can be regarded as specific features of our aquaplanet, the design of our experiment should not support an asymmetrical eddy momentum flux in the tropics.

After a series of careful testing, it has been found that when the effects of cloud are ignored in the infra-red radiation scheme of IGCM3 (i.e. if subroutine CLDTRAN is not called), the transient eddy momentum flux is symmetrical about the equator and there is no longer a cross-equator transport of eddy momentum. A plot of $[\overline{u'v'}]$ with the clouds neglected in the radiation scheme is plotted in the lower panel of figure 4.8.

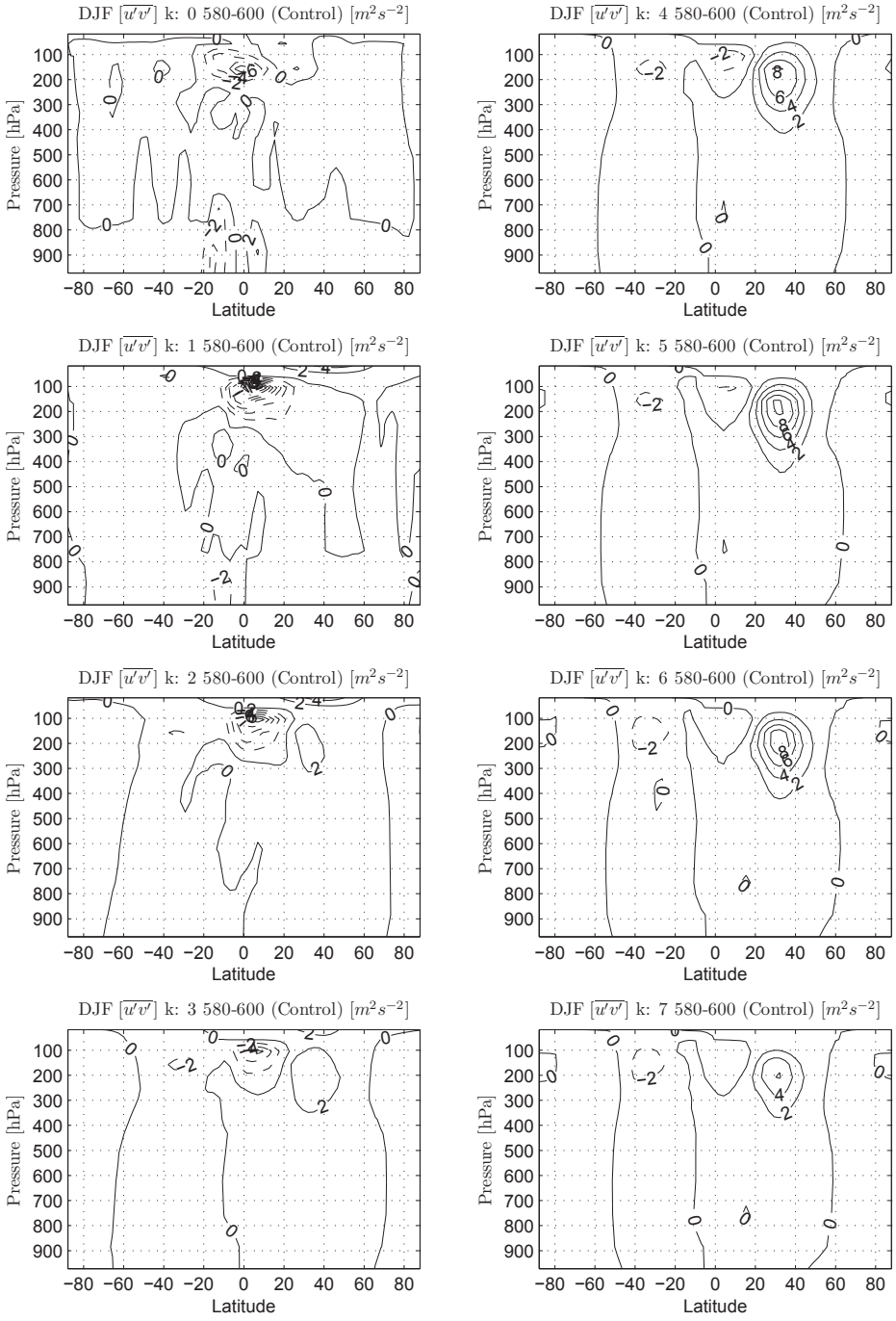


Figure 4.6.: DJF Transient eddy momentum flux (Control) by different wavenumbers. Wavenumber increases from 0 to 3 in the left column and from 4 to 7 in the right column $[m^2s^{-2}]$. Contour intervals are $2m^2s^{-2}$.

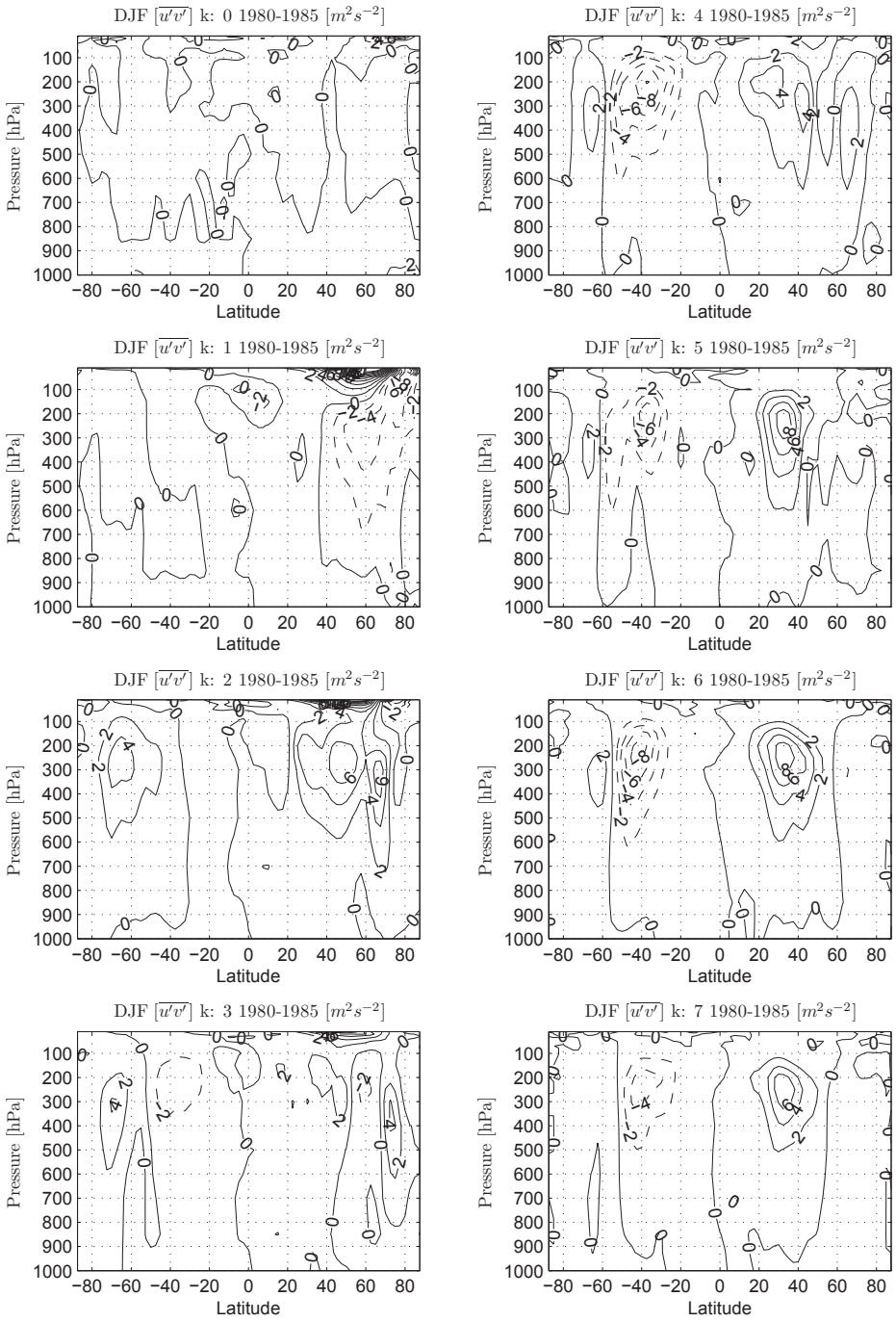


Figure 4.7.: Same as figure 4.6, but for NCEP data

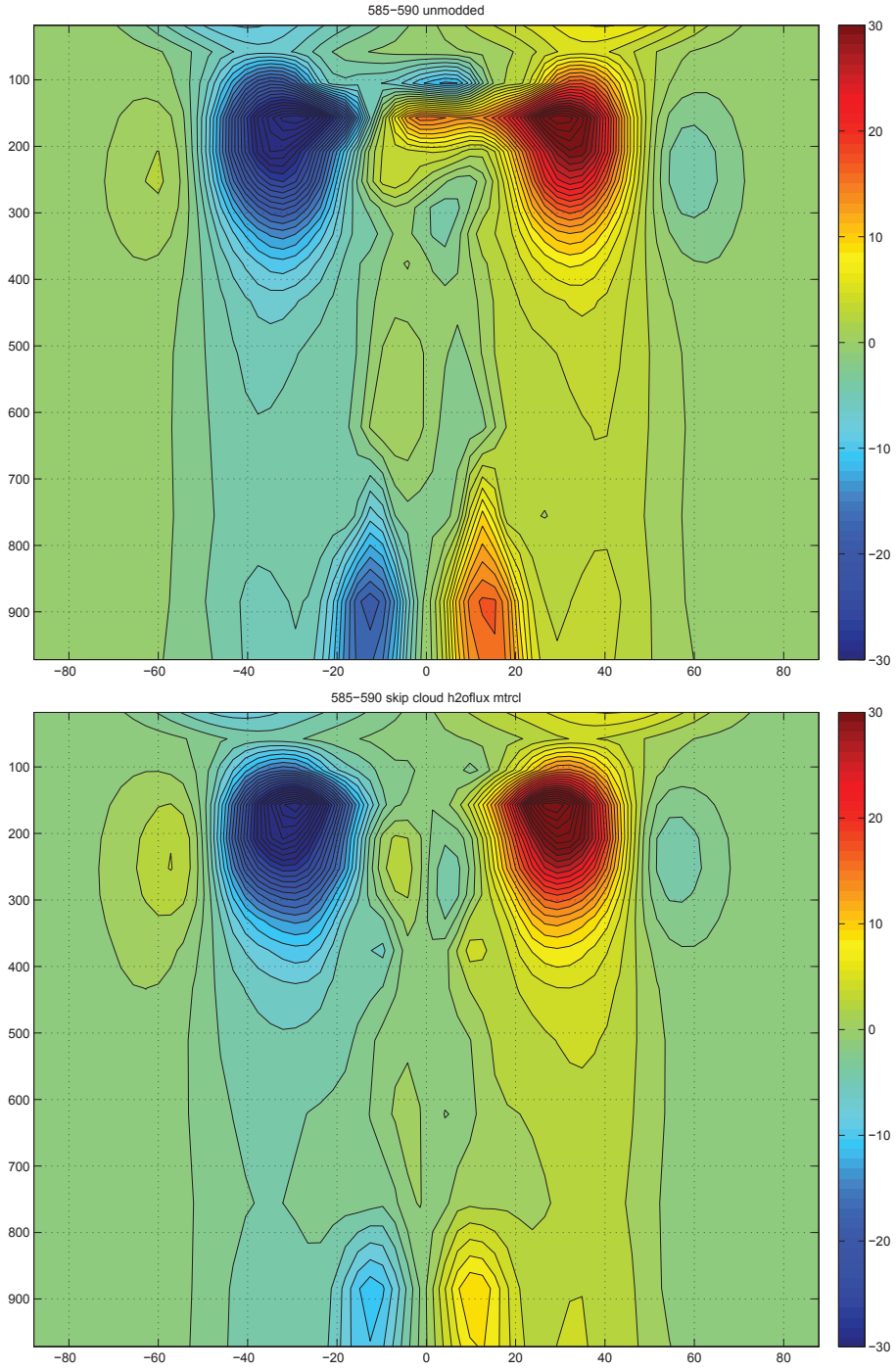


Figure 4.8.: Annual mean $[\overline{u'v'}]$ for the control run (top) and the control run with clouds removed from the radiation scheme in IGCM3. Data is computed and averaged over a period of 5 years (585-590).

The result shows that the cloud is responsible for the unusual eddy momentum transfer across the equator and possibly provides an explanation to other asymmetrical aspects of the model as mentioned before. However, the method of disabling the clouds partially in the radiation scheme only highlights the origin of the problem and cannot be used as the ultimate fix. Moreover, clouds play an important role in the Earth's radiation budget and removing them from the system would adversely affect the climatology of the aquaplanet.

Since FORTE has interactive clouds built-in, fixing the asymmetrical cloud forcing problem is not a simple task but requires one to re-run the model from rest, which can be very time-consuming. Given that our main focus is on the response of the subtropical jet-stream, we decided to proceed with the experiment and concentrate on the dynamics at higher latitudes.

4.4. Eddy Fluxes and Feedbacks

4.4.1. Steady and Non-Dissipative Flow

From section 4.1 we learnt that the zonal wind anomalies exhibit a banded structure in both the $x5O_3$ and $x5O_{3FSST}$ experiments. In this section we seek to understand the mechanisms behind these changes and decide whether eddy feedbacks are involved as in HBD05.

The field of poleward eddy momentum flux $[u^*v^*]$ for the control run is shown in figure 4.9. Note that * denotes the deviation from the zonal mean as in equation 1.18. To understand its relationship to the zonal wind field in the steady state let us consider equation 1.18. Assuming $[v]$ is on the order of the Rossby number R_o and hence, under quasigeostrophic approximation such that ($R_o << 1$), equation 1.18 can be rewritten as [48].

$$\frac{\partial [u]}{\partial t} = -\frac{1}{R\cos^2\phi}\frac{\partial [u^*v^*]\cos^2\phi}{\partial \phi} + f[v] + [F_\lambda] \tag{4.6}$$

For a steady flow, such that $\frac{\partial[u]}{\partial t} = 0$, equation 4.6 reduces to,

$$f[v] = \frac{1}{R\cos^2\phi}\frac{\partial[u^*v^*]\cos^2\phi}{\partial\phi} \tag{4.7}$$

where we have assumed the flow is non-dissipative and dropped the $[F_\lambda]$ term. This is a valid assumption as the cores of the jet streams are located in the upper portion of the troposphere and are free from surface friction.

Equation 4.7 states that, under steady, non-dissipative conditions, the eddy forcing term is perfectly balanced by the Coriolis force of the mean meridional circulation. This is indeed observed in our aquaplanet; the latitudes at which the eddy momentum flux converges/diverges coincides with the location of the meridional cells in the atmosphere. For instance, at about $170hPa$, the eddy momentum flux is up gradient between $10N$ and $30N$ (figure 4.9). Equation 4.7 suggests that this must be balanced by the Coriolis force from a poleward flow of air and is consistent the position of the Hadley cell (see figure 4.4).

4.4.2. Eddy Feedbacks

The anomalies of eddy momentum flux for both $x5O_3$ and $x5O_{3FSST}$ experiments, relative to the control run (figure 4.9), are shown in figure 4.10. In the $x5O_3$ case, eddy forcing peaks in the upper troposphere, where the core of the jet stream is located. With reference to equation 1.18, the latitudinal gradient of the eddy momentum flux $\frac{\partial[u^*v^*]\cos^2\phi}{\partial\phi}$ has increased between 33^o and 55^o in response to the injection of ozone and implies an easterly forcing. Similarly, the reduction of eddy momentum flux gradient between 10^o and 33^o suggests a westerly forcing. Similar arguments hold for other latitudes. Comparing these regions with the zonal wind anomalies (figure 4.3) affirms that they coincide with the same sign.

This does not explain the zonal wind anomalies above $150hPa$, where there is a general decrease of the sub tropical jets and no clear sign of a latitudinal structure is observed. This can be explained by noting that the stratosphere has warmed up noticeably since the introduction of 5 times ozone from year 1020. Hence, the thermal tropopause lowers and consequently forces the

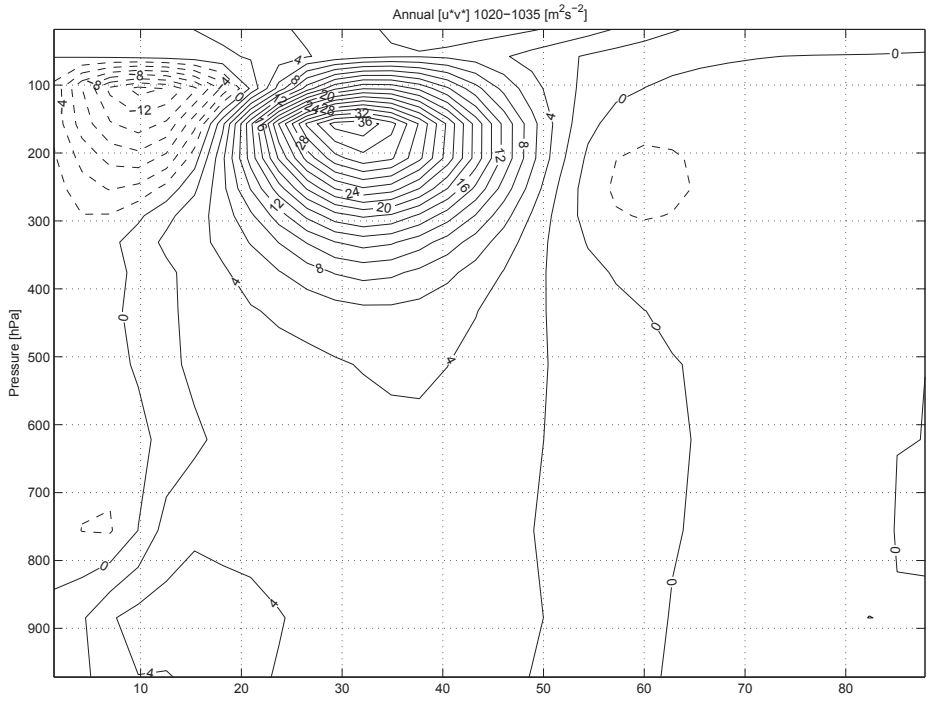


Figure 4.9.: Zonal mean eddy momentum flux $[u^*v^*]$ for the control run. Contour intervals = $2m^2s^{-2}$.

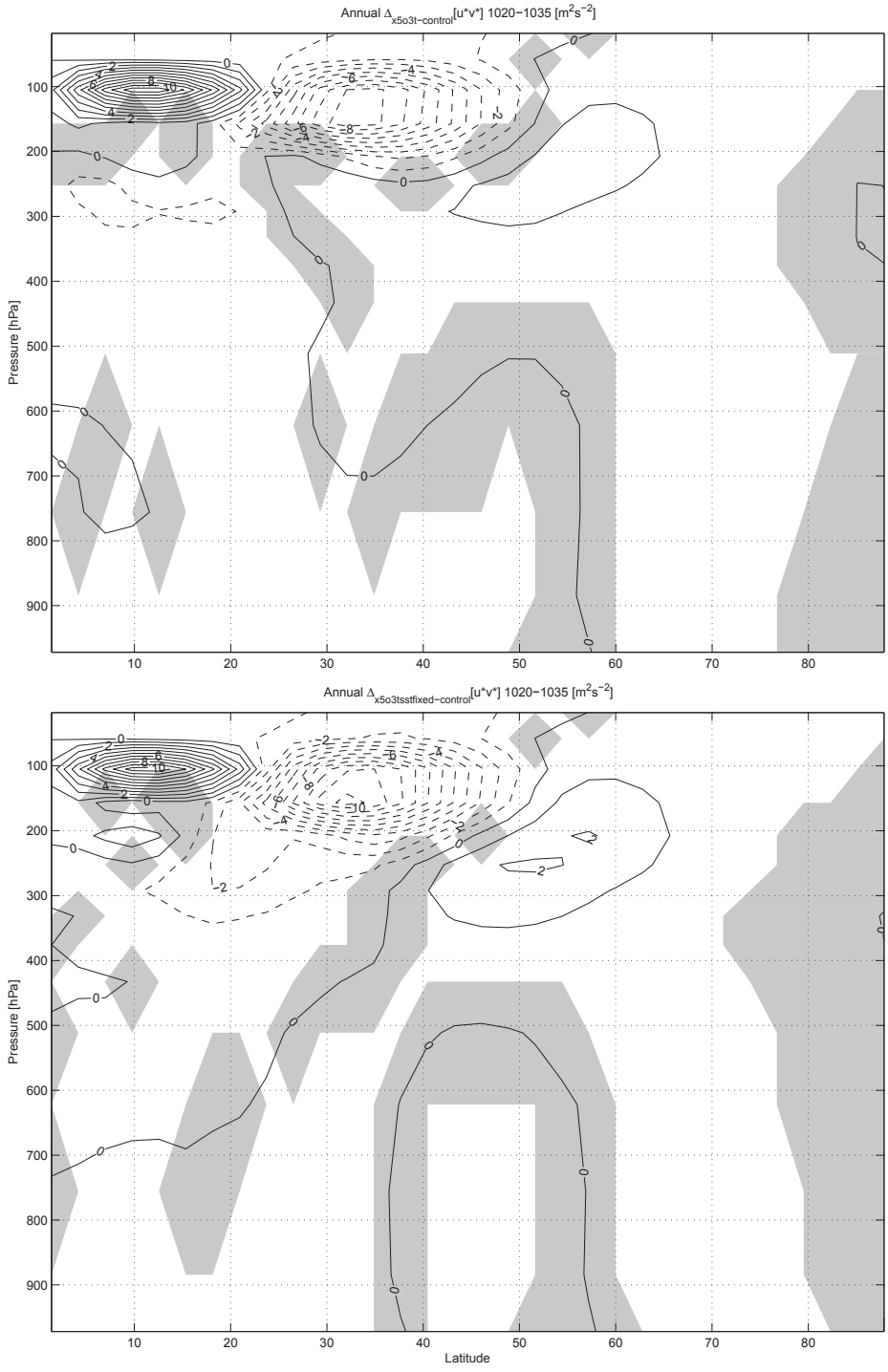


Figure 4.10.: Zonal mean eddy momentum flux anomalies $[u^*v^*]$ for the $x5O_3$ (top) and $x5O_{3FSST}$ (bottom) runs. Contour intervals $= 1m^2s^{-2}$. Signals that does not reach a 95% confidence level are shaded.

tropospheric jets downwards towards the surface. This is evident as shown in figure 4.1, from which a clear downward shift of the core of the jet is observed.

As described in HBD05, the eddy forcing anomalies peak in the upper troposphere and drives the mean state from thermal wind balance below the tropopause. Balance is achieved by the Coriolis acceleration of a counteracting anomalous meridional overturning circulation. For instance, at about $130hPa$ between 10^o and 30^o, there is a westerly forcing by the eddies which coincides with a weakening of the poleward flowing branch of the Hadley cell. The argument applies to the anomalies observed in the upper branch of the 'inverted' and Ferrel cell as well.

By continuity the anomalies in the upper branch of the meridional overturning cells must be reflected in the opposite sense at the surface. Considering the level where the eddy momentum flux peaks, the balance between the eddy forcing anomaly and Coriolis acceleration from meridional flow anomaly is no longer valid in the lower troposphere. Instead, this is partially balanced by the surface drag [22].

The pattern of eddy momentum flux anomalies of the $x5O_{3FSST}$ experiment is very similar to the result from $x5O_3$, especially in the upper troposphere region where eddies play a dominant rule in maintaining the zonal momentum budget. As would be expected from the zonal wind anomalies previously shown in figure 4.3, it is found that the anomalies in the $x5O_{3FSST}$ case are found to be generally stronger at the levels where $[u^*v^*]$ peaks, yielding a steeper anomalous meridional flux gradient. As a result, the anomalous easterly forcing in the mid-latitudes is expected to be stronger compared to the case where there is a coupled ocean. A weaker jet is indeed observed in the $x5O_{3FSST}$ case (figure 4.3).

4.4.3. Vertically Integrated Momentum Budget

From last section we observe that the eddy momentum flux divergence anomalies coincide with the change in zonal wind at mid latitude-upper troposphere region. At lower levels it is unclear whether other terms such as surface friction will dominate over the role of the eddies. In addition, the $\frac{1}{cos^2\phi}$ factor renders the divergence of both the mean meridional and eddy terms less effective in forcing the zonal wind at the equatorward flank of the jet. Referring to figure 4.3, the tropical zonal wind anomalies are found to behave rather differently in the presence of an interactive ocean. Therefore, it is useful to diagnose the contribution to zonal wind forcing from each individual term in equation 1.18.

To aid the diagnosis we calculate the vertically integrated momentum budget by integrating equation 1.18 with respect to pressure as described in HBD05. Consider the zonal force per unit area acting on a column of air that stretches from the surface to TOA, integrating 1.18 yields,

$$\int \rho_a \frac{\partial [u]}{\partial t} dz = -\int \rho_a \frac{1}{R\cos^2\phi} \frac{\partial \cos^2\phi([u][v]+[u^*v^*])}{\partial \phi} dz + \int \rho_a [F_\lambda] dz \tag{4.8}$$

where ρ_a is density of air as before. Note that by continuity $\int \rho_a f[v]dz$ vanishes and there are now fewer terms in the equation. Using the hydrostatic equation, equation 4.8 becomes,

$$\begin{aligned} \frac{1}{g}\frac{\partial}{\partial t}\int_0^{p_s}[u]dp = &-\frac{1}{g}\frac{1}{R\cos^2\phi}\frac{\partial}{\partial\phi}\left\{\cos^2\phi\int_0^{p_s}([u][v]+[u^*v^*])dp\right\} \\ &+\frac{1}{g}\int_0^{p_s}[F_\lambda]dp \end{aligned} \tag{4.9}$$

or,

$$\frac{1}{g}\frac{\partial}{\partial t}\int_0^{p_s}[u]dp = C_{Zonal} + C_{Eddy} - [\tau_\lambda] \tag{4.10}$$

where p_s is the surface pressure, $[\tau_\lambda]$ is the zonal mean zonal component of the surface wind stress in units of Nm^{-2}. In IGCM3 $[\tau_\lambda]$ follows the formulation as in [10],

$$\tau_\lambda = -\rho C_D |v'| u \tag{4.11}$$

where

$$C_D = \frac{K^2}{\ln^2(z_1/z_0)} \tag{4.12}$$

$$v' = |v| + 3ms^{-1} \tag{4.13}$$

u is the x-component of the wind velocity, $|v|$ is the horizontal wind speed and C_D is the drag coefficient respectively. K is the von Kármán constant and is set to 0.41 in the model. z_1 is the lowest model level from the surface and the roughness length z_0 is a constant.

Figure 4.11 shows the individual terms in the vertically integrated momentum budget equation (equation 4.10) for the control run. The divergence of the mean circulation term C_{Zonal} is generally small (except the tropics) compared to other terms and reveals the latitudinal location of the upper branch of the Hadley and Ferrel cells. Referring to figure 2.7, at about $150hPa$ between $0^o - 10^oN$, both the mean zonal and meridional wind fields are negative such that there is net poleward momentum transport by the mean circulation. This is in the same sense as the momentum transport by the Hadley circulation and hence the location of the 'inverted' cell can not be easily identified by C_{Zonal}. In contrast to HBD05, where the mean circulation term is small near the equator, C_{Zonal} dominates the equatorial region in our aquaplanet. This can be explained by considering the peak magnitude of the easterly flow in the tropics, which is comparable to that of the jet stream. In addition, C_{Zonal} is partially compensated by C_{Eddy} in our aquaplanet where C_{Zonal} & C_{Eddy} are both negative in HBD05. At mid-latitudes, C_{Zonal} plays a less significant role and hence the westerly jet is mainly maintained by the balance between the surface stress and the eddy term C_{Eddy}.

Note in all latitudes, the magnitude of the budget residual is significant. For instance, at mid-latitudes where we expect eddy dominates, C_{Eddy} is found to be too weak to fully balance the surface stress. To test why this is the case, we varied the output frequency f_{out} of FORTE and repeated our calculation. The result is shown in figure 4.12. We observe that as we increase f_{out}, the amplitude of C_{Eddy} also increases. For example, C_{Eddy} increases from $0.040Nm^{-2}$ to $0.055Nm^{-2}$ at the tropics as we increase the

number of model outputs from 1 per model day (our default setting) to 16 per model day. As a result, the residual in this region becomes much smaller and suggests the momentum budget in this region is approximately closed. In contrast, decreasing f_{out} of FORTE seem to have an opposite effect. The reason why varying the output frequency of FORTE only changes C_{Eddy} but not C_{Zonal} and surface stress (not shown) is due to the transient nature of eddies. By increasing the number of data points per day we are improving the temporal resolution of the model and hence the eddies are better resolved in the diagnostics.

Similar arguments apply to mid-latitudes. In addition to an increase in amplitude, a slight poleward shift of C_{Eddy} is also observed as f_{out} is increased. However, it is found that even with FORTE outputting every 90 model minutes, C_{Eddy} is still not large enough to balance the surface stress and fully close the momentum budget at mid-latitudes. An output every $15 - 20mins$ is required to adequately resolve the eddies and close the momentum budget (personal communication with Haigh J., Imperial College London). Unfortunately, this can not be tested as the output files are too large at the current spatial resolution (T42L15) for our machines. In addition, since IGCM3 and MOMA only exchanges information once per model day in FORTE, increasing f_{out} further will not help understanding the role of the ocean in ST coupling on time-scales shorter than 1 day. As a workaround to the problem, we make use of the fact that the mean flow, eddy and surface stress terms must balance each other after reaching the new equilibrium so that equation 4.10 ≈ 0 in the long run. Considering the fact that eddy interactions in ST coupling are on the time scale of $\sim 40days$ [56], this is a valid assumption as both of our ozone experiments ran for 15 model years. Hence, in the following, we decided to proceed with daily model output and calculate C_{Eddy} from C_{Zonal} & $[\tau_\lambda]$ (i.e. assuming zero residual) instead of computing it directly from the model.

Figure 4.13 shows the anomalies in each of the terms in the vertically integrated zonal momentum equation for experiments $x5O_3$ and $x5O_{3FSST}$. At mid-latitudes, the anomalies in C_{Zonal} is small compared to the surface stress anomaly, which implies that eddy flux convergence anomalies play a dominant role in maintaining the balance in momentum budget. This holds

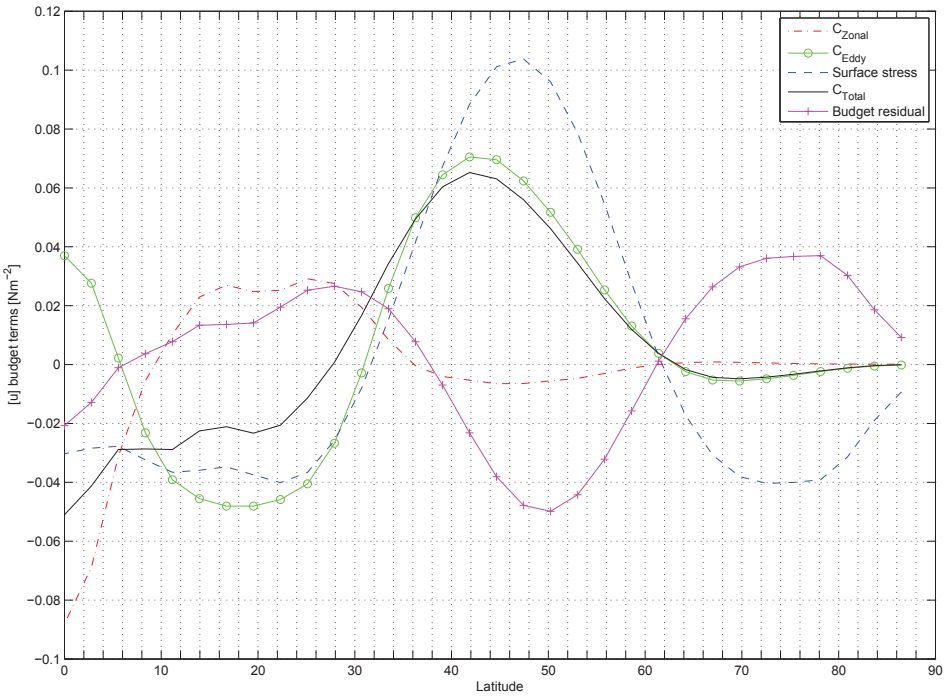


Figure 4.11.: Terms in the vertically integrated zonal momentum equation for the control run $[Nm^{-2}]$.

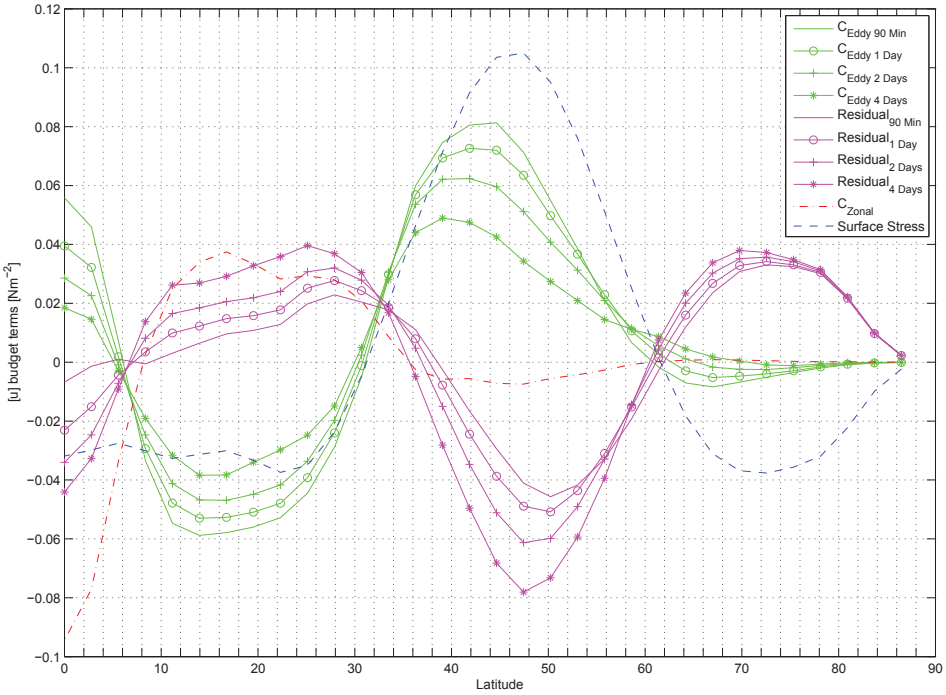


Figure 4.12.: Magnitudes of C_{Eddy} (green) term in the control run, calculated using different model output intervals: 90 mins, 1 day, 2days, 4days (see legend). Only data from year 1020 is used. C_{Zonal} (red), surface stress (blue) are constant in all cases and are plotted as a reference. The corresponding residuals (magenta) in the vertical momentum budget for each output interval are also plotted. All units in $[Nm^{-2}]$.

true for both $x5O_3$ and $x5O_{3FSST}$ and is consistent with the findings of HBD05. In the tropics, anomalies of the mean circulation become significant and are mainly balanced by that of eddies. In addition, as would have expected from the result from zonal wind changes shown previously, the magnitude of the anomalies of each term are generally larger when there is no ocean coupling.

A careful inspection on the C_{Zonal} term shows that, although there is a general weakening on its contribution to the acceleration of zonal wind, there is no latitudinal shift of the divergence of $[u][v]$ at mid-latitude when the SST is held fixed. For instance, equatorward (poleward) of 36^o there is a positive (negative) contribution of zonal wind acceleration by the mean meridional circulation in the control run (figure 4.11). The anomalies of C_{Zonal} at the corresponding latitude crosses the zero line at 38^o instead of 36^o, such that the mean meridional anomalies play a role in shifting the jets equatorward in the case where there is an interactive ocean. Similar argument applies to the boundary between the 'inverted' and Hadley cell ($\sim 12^o$). In $x5O_3$, the mean circulation anomalies crossed the zero line at 14^o instead of 9^o, which is a sign of the expansion of the equatorward flank of the jets. In the fixed SST experiment, the shifting of the $[u]$ by C_{Zonal} is not as pronounced.

Since C_{Zonal} represents the contribution to zonal momentum by the mean meridional circulation, our results suggests the mean flow does not contribute to the displacement of the jets in the fixed SST experiment as the positions of the Hadley and Ferrel cells are limited by the SST. In other words, the mean meridional cells do not feel the effect of surface water heating up as a result of weakened Ekman cell but follows the same seasonal cycle of SST for each year in $x5O_{3FSST}$. In contrast, except the magnitude of the response, there is no significant discrepancies in the anomalies of C_{Eddy} and surface stress between the two experiments.

The mechanism by which stratospheric heating changes circulations in the troposphere is described in SBH09. Heating the stratosphere alters both the vertical and meridional temperature gradients around the tropopause, which also changes the horizontal heat and momentum fluxes in that region. The initial eddy momentum flux anomalies drive anomalous zonal wind lo-

cally in the upper troposphere, and at the same time, imposes changes to the mean meridional circulation. The altered meridional circulation influences both zonal wind and temperature throughout the troposphere and in return, feeds back on to the system by creating further changes to the horizontal eddy momentum flux. In section 4.2 we find that a warmer SST in the $x5O_3$ run encourages convection of air, which opposes the weakening of meridional cells caused by eddy momentum flux anomalies. As the anomalies in meridional circulation is suppressed in $x5O_3$, the effect of eddy feedbacks are also weaker, as shown in figure 4.13.

To summarise, the anomalies of C_{Eddy}, C_{Zonal} and surface stress are more pronounced when the SST is held constant, consistent with the zonal wind responses described in section 4.1. On the other hand, our results show that the anomalous mean flow plays a significant role in shifting the jet equatorward in a fully coupled aquaplanet despite its small magnitude compared to the rest of the terms in equation 4.10. This is because the relative positions of the mean meridional cells in the atmosphere, which are regulated by the spatial distribution of the SST, are not fixed in $x5O_3$.

4.5. Summary and Conclusions

The purpose of this chapter is to study how the zonal wind changes in response to a thermal perturbation in the stratosphere in the presence of an interactive ocean. Previous studies [22, 56] show that eddy momentum flux adjustments play a key role for such changes. Hence, in this chapter we have decomposed the terms of the zonal momentum equation into its mean and eddy components in order to highlight their relative significance in regulating zonal wind in a atmosphere-ocean coupled model.

- In response to a thermal perturbation in the stratosphere induced by an increased amout of O_3, the jets have weakened and shifted equatorward in the $x5O_{3FSST}$ run.
- When the atmosphere is coupled with the ocean ($x5O_3$), the troposphere shows a similar result, but of a weaker response. Also, the extent to which the jets have shifted towards the equator is greater when the SST is not fixed.

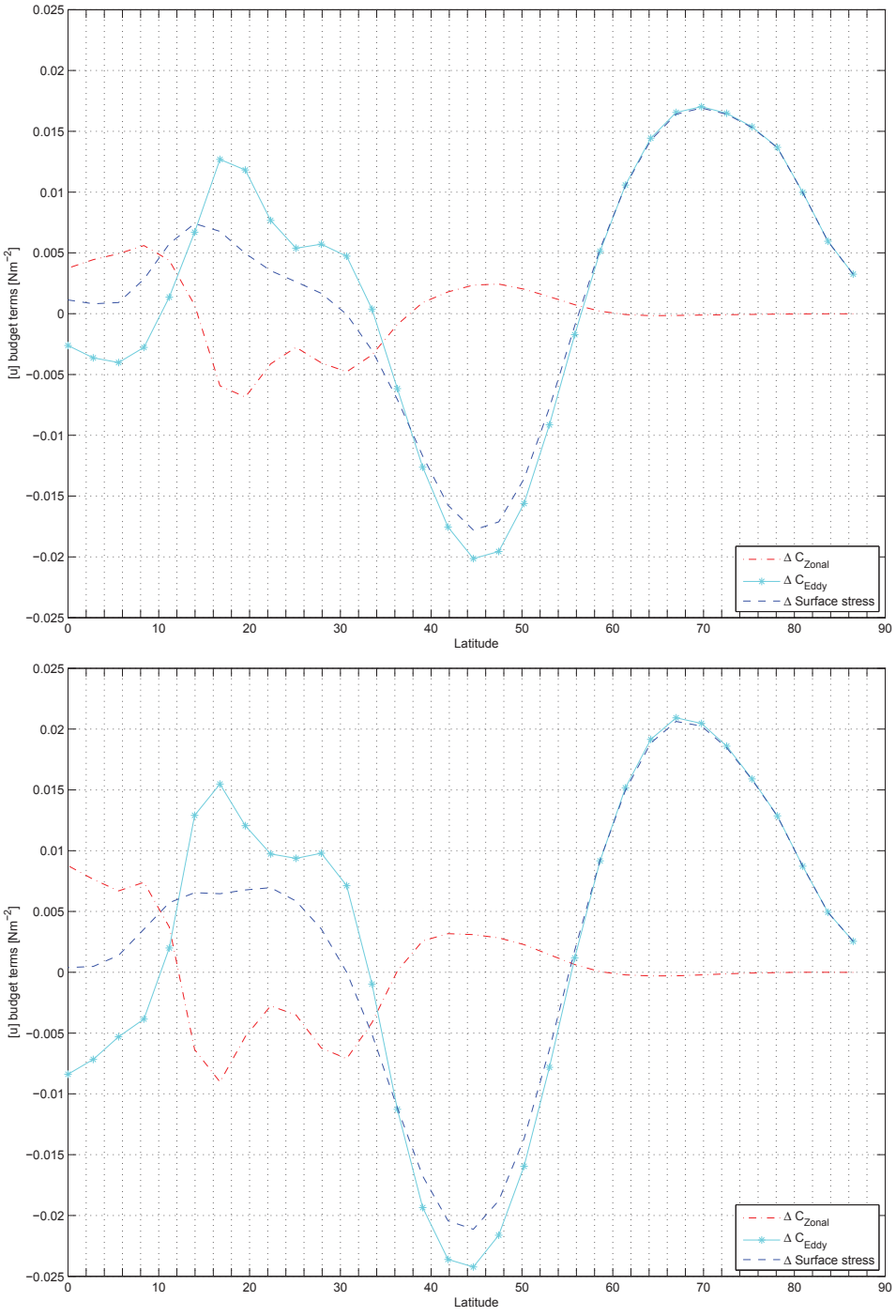


Figure 4.13.: Anomaly of different terms in the vertically integrated zonal momentum equation for $x5O_3$ (top) and $x5O_{3FSST}$ (bottom) $[Nm^{-2}]$.

- Due to increased UV absorption in the stratosphere, the thermal tropopause is found at a lower level. As a result, the cores of the jets have shifted towards the surface and the height of the meridional cells in the atmosphere have also decreased.

- The 'inverted', Hadley and Ferrel cells have weakened in both the experiments. As in the zonal wind anomalies, when the SST is fixed, the weakening is found to be more pronounced while there is less meridional shifting of the cells.

- By decomposing the wind fields as a sum of their time mean and instantaneous fluctuation from the symmetric flow (e.g. $u = \bar{u} + u^{'}$), we find that the time averaged eddy momentum flux across the equator is asymmetrical and have a wavenumber of 0-3. This suggests that the zonal mean flow at tropical regions fluctuates with time and exhibits wave-like behaviour.

- The asymmetrical eddy momentum transfer over the equator is found to be caused by the subroutine CLDTRN, which calculates cloud transmittances in the radiation scheme of IGCM3. The exact origin of the problem is yet to be determined.

- The anomalies of the divergence of eddy momentum flux is found to coincide with the pattern of the zonal wind changes in both experiments. Consistent with the zonal wind response, the anomalies in the eddy flux is also stronger when the SST is fixed.

- Compared to the fixed SST experiment, both anomalies of C_{Eddy} and surface stress of $x5O_3$ are smaller as far as the vertically integrated momentum budget is concerned. Although the magnitude of the C_{Zonal} term is generally small compared to the other terms, it plays a role of contributing to the equatorward shift of the jets when the SST is not fixed and the meridional cells are free to move.

- A possible mechanism in explaining the difference in zonal wind response in the presence of an interactive ocean is proposed. The weakening of the meridional cells caused by ozone heating in the stratosphere is partially compensated by enhanced SST-induced convection in the $x5O_3$ run. As a result, there is less forcing on zonal wind

throughout the troposphere by anomalous meridional circulation and hence less eddy feedback effects in the case which the ocean is dynamic.

5. Results: Energy Budgets

The primary source contributing towards the Earth's energy budget comes from solar radiation. However, upon entering the atmosphere, not all of the solar energy retains in the Earth's system. Instead, about 23% and 7% gets reflected back into space by clouds and surface respectively [63].

About 23% of the solar radiation, which spans over a range of wavelengths, is absorbed by different chemical species in the atmosphere, where it deposits energy as heat. The rest of the solar radiation (47%) makes its way to the surface where it is absorbed by the landmass & ocean and hence also contributes to the internal energy of the system [63]. To achieve radiative equilibrium, the inflow of solar energy is balanced by an outgoing radiation from the Earth, which takes the form of thermal radiation from the surface and emission by greenhouse gases.

Previously in chapters 3 and 4 we gained an insight into how the atmosphere and ocean respond dynamically to a situation in which stratospheric ozone had increased by 5 times. In this chapter we focus on the radiative aspects of the experiment. For instance, since ozone is a strong absorber of UV, one expects the stratosphere to heat up due to increased absorption of incoming solar radiation. This results in augmented LW and a reduction of SW radiation entering the troposphere. However, the SW and LW anomalies are of different magnitude and do not balance each other. Hence, radiative balance at each pressure level is achieved by internal adjustments of the system, which include altered terrestrial radiation, sensible and latent heat fluxes.

5.1. Air Temperature

5.1.1. Stratosphere

Figure 5.1 shows air temperature anomalies for both the $x5O_3$ and $x5O_{3FSST}$ runs. In both cases, it is observed that the stratosphere has heated up by an enormous amount due to increased UV absorption by ozone. The warming is uneven with latitude and altitude such that the meridional temperature gradient is altered differently with each pressure level.

For instance, at the $150hPa$ level, there is a warming of $8K$ and $16K$ at the tropics and 60^o respectively. The increase in the latitudinal temperature gradient implies negative forcing to the zonal winds across the specified pressure level and coincides with the zonal wind anomalies as shown in figure 4.3. In contrast, the temperature gradient at $50hPa$ between the same latitudes has decreased in both experiments. As a result, there is a strengthening of zonal wind in the stratosphere in these regions (see also figure 4.3).

5.1.2. Troposphere

While the temperature anomalies in the stratosphere can largely be explained by a change in direct radiative heating, the tropospheric thermal response is not straightforward. As the concentration of ozone increases, more absorption of UV takes place in the stratosphere and is therefore more opaque to incoming solar radiation. As a result, one would expect that less SW radiation entering the troposphere and reaching the Earth's surface.

With no other effects, in order to achieve radiative equilibrium, the tropospheric temperature must also decrease such that its thermal radiation balances the reduced downward SW flux. An alternative explanation is to consider the incoming solar flux arriving at the tropopause as the energy source required to maintain a specific mean tropospheric temperature. As there is less energy input into the troposphere, its global mean temperature is required to drop if there is no other energy source.

The above statement is valid if the reduced downward SW is the only radia-

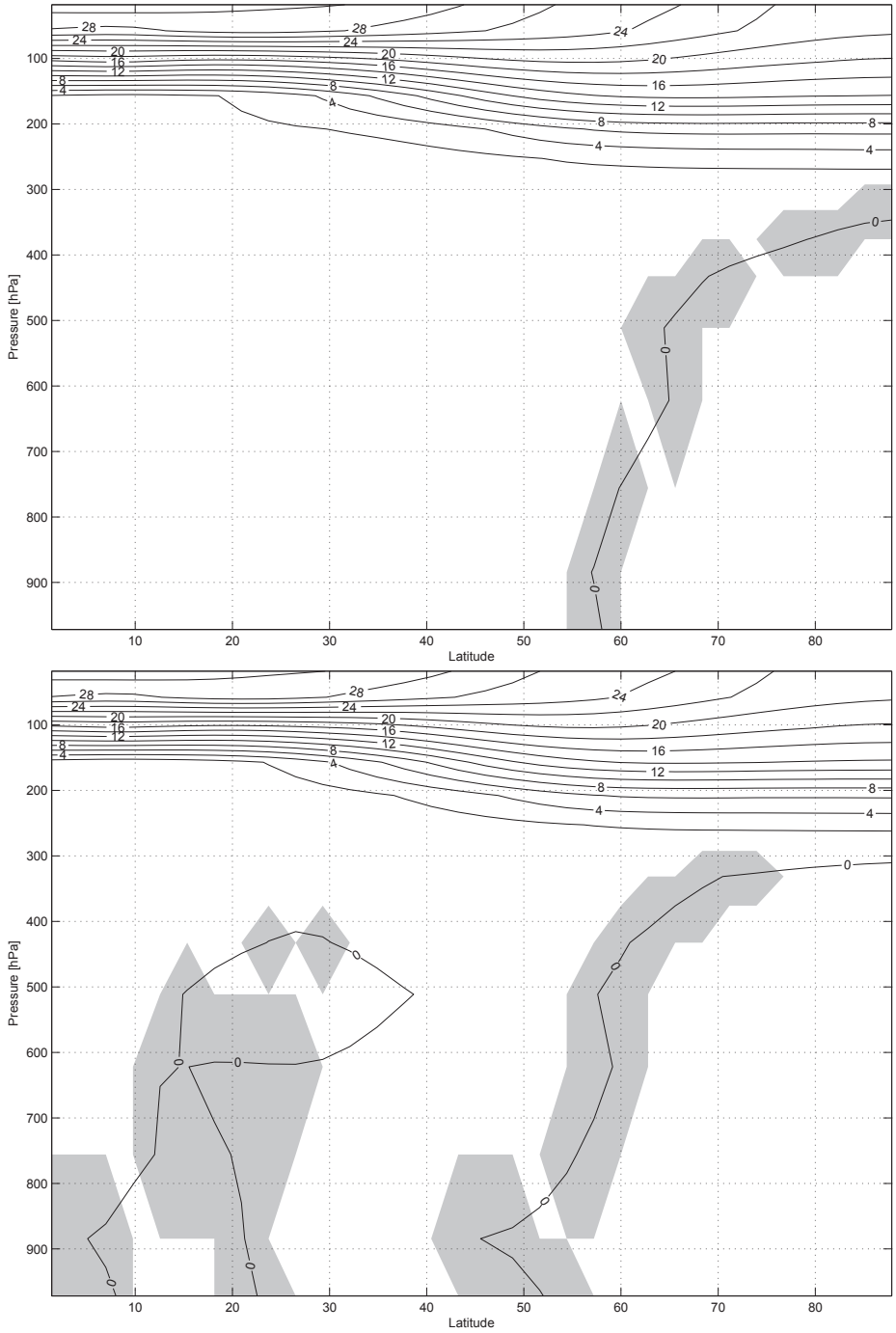


Figure 5.1.: Air temperature anomalies for $x5O_3$ (top) and $x5O_{3FSST}$ (bottom) runs [K]. Regions that does not reach the 95% significance level are shaded. Contour intervals = $2K$.

tive forcing acting on the troposphere. As the stratosphere warms up, however, it emits more LW radiation in both upward and downward direction. Therefore, given a fixed surface temperature, the global mean tropospheric temperature is dependent on the balance between the perturbed downward SW and LW radiation at the tropopause.

Figure 5.2 is the same as figure 5.1 but with contours chosen to highlight the temperature anomalies in the troposphere. In both $x5O_3$ and $x5O_{3FSST}$, the tropospheric temperature response is small compared to that in the stratosphere, but our analysis shows that there are regions of statistically significant warming and cooling. In the fixed SST experiment (bottom panel), there is a vertical band of warming centered at 40^o, with cooling in its equatorward flank and poleward of 60^o.

In the case of $x5O_3$ run (figure 5.2, upper panel), there is a general increase in temperature in the troposphere except for latitudes higher than 60^o. While the polar response is similar, the results from $x5O_3$ lacks the dipole pattern as observed in the $x5O_{3FSST}$ run. In addition, the temperature anomaly from $x5O_3$ shows a clear sign that the global mean tropospheric temperature has increased while it is not so clear whether the $x5O_{3FSST}$ troposphere has gained energy in response to the ozone perturbation. Since the response patterns are significantly different from each other, this is regarded as one of the major findings of this thesis.

In order to give a more comprehensive understanding on the energy budget of the system, we make use of equation 1.30 to compute the moist static energy for each atmospheric layer. The benefits of doing a global integral is that it removes the need for esimates of latitudinal heat transport.

5.2. Moist Static Energy

5.2.1. Stratosphere

Figure 5.3 shows the change in globally integrated moist static energy for both experiments. Referring to the upper panel, it is observed that the moist static energy has increased sharply by about $3.2 \times 10^{22} J$ over the first

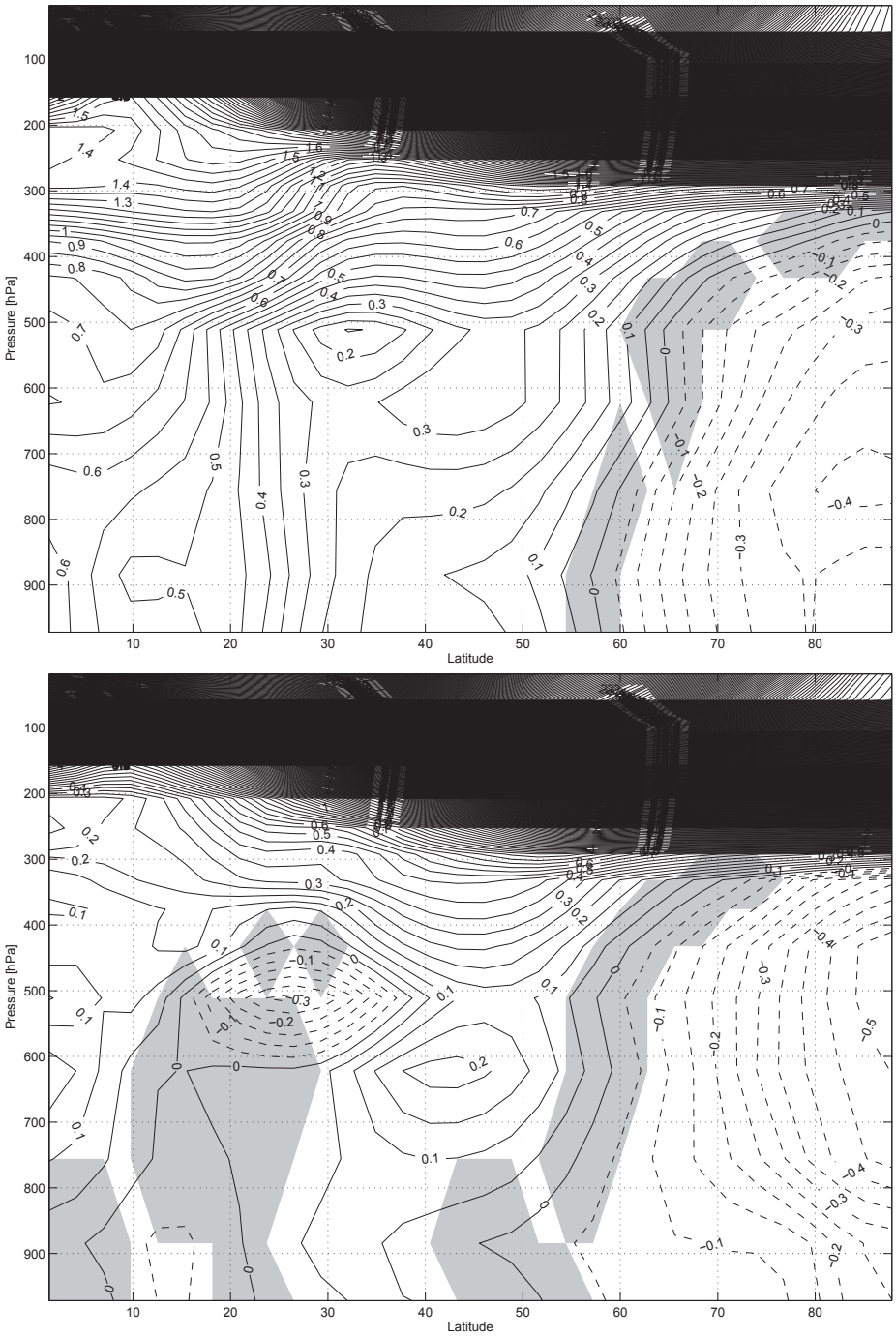


Figure 5.2.: Same as figure 5.1, but contour levels are chosen to put emphasis on the anomalies in the troposphere. Contour intervals = $0.05K$.

three months after the ozone perturbation is applied. This is expected as radiative effects are almost instantaneous.

As stratospheric air is very dry, the observed anomaly is dominated by changes in its internal energy. On the other hand, due to the fact that the stratosphere is remote from the surface, there is no significant difference between the two experiments.

5.2.2. Troposphere

As can be inferred from figure 5.1, the moist static energy of the troposphere (figure 5.3, lower panel) in the $x5O_3$ run has increased, by about $6 \times 10^{21} J$ over 15 years of model time. In contrast, there is no obvious trend in the case where the SSTs are fixed. Compared to the stratosphere, the signal to noise ratio of the moist static energy anomaly is much lower in both experiments.

Considering the fact that the SST field is the only field IGCM3 reads from MOMA at the end of each model day, even if both the atmospheric and ocean components are run simultaneously, the atmosphere does not actually 'see' the ocean and is isolated from its effect in the $x5O_{3FSST}$ run. Given the same perturbation in the stratosphere, the discrepancies in the global mean tropospheric temperature between the two runs should depend predominantly on changes in surface flux.

5.3. Radiation Budget

As described in previous sections O_3 is a strong absorber of ultraviolet which limits the amount of SW radiation entering the troposphere. Upon absorption of incoming solar radiation by ozone, energy is also deposited in the ozone-rich stratosphere in the form of heat which in return, the stratosphere also emit energy via longwave radiation into the troposphere and also back into space.

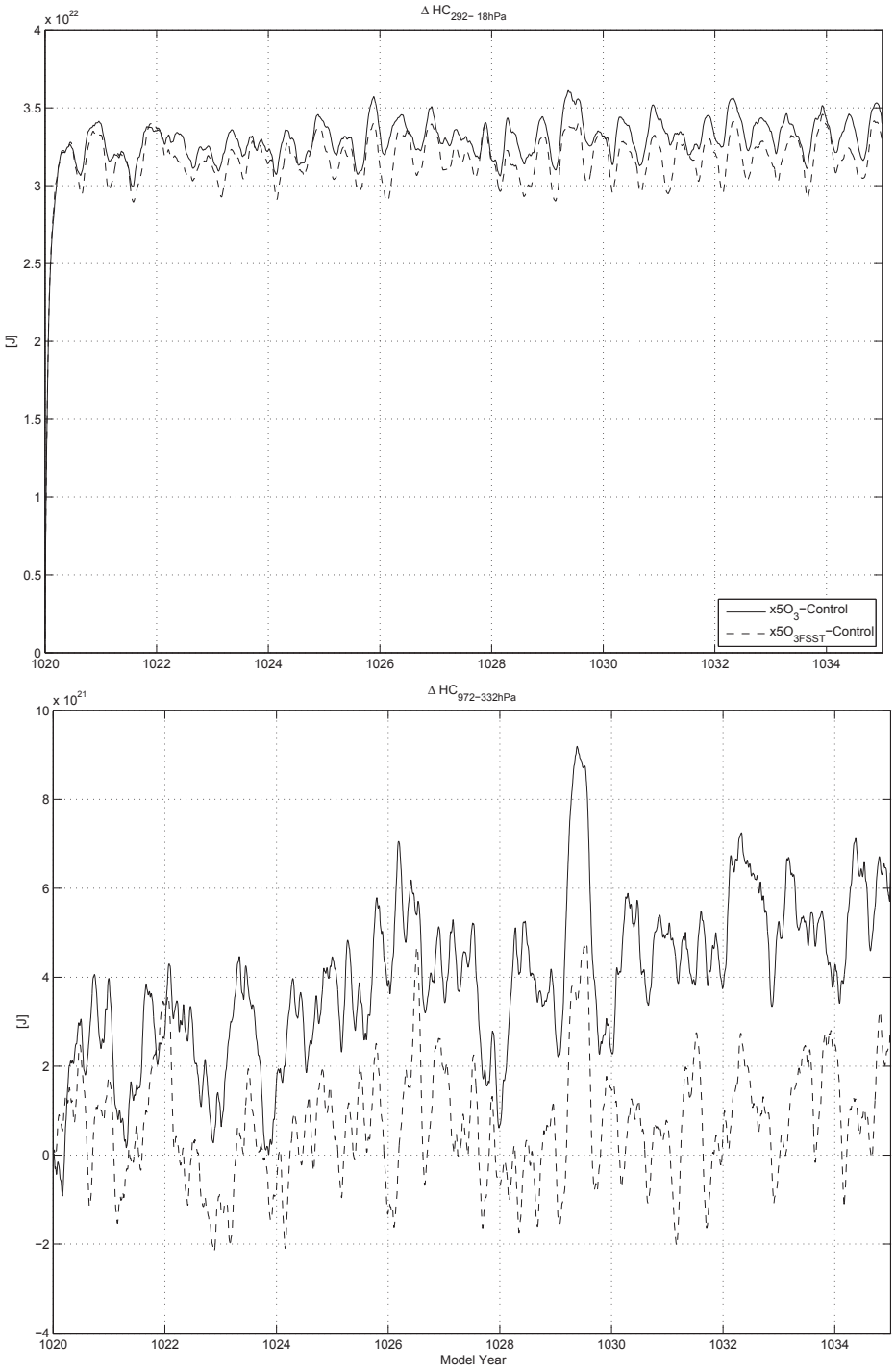


Figure 5.3.: Globally integrated stratospheric (top) and tropospheric (bottom) moist static energy anomaly for $x5O_3$ (solid) and $x5O_{3FSST}$ (dashed) [J].

Regarding the radiation budget of our experiments, consider the net radiative flux F_{Net} across a specific pressure level,

$$F_{Net} = F_{SW\downarrow} - F_{SW\uparrow} + F_{LW\downarrow} - F_{LW\uparrow} \tag{5.1}$$

where F is the radiative flux integrated globally over a specific pressure level (in units of W) and the subscripts SW & LW denote the nature of the radiation. The arrows indicate the flux direction. Note that at radiative equilibrium, F_{Net} at the top of atmosphere is approximately zero (when averaged over period of several years [48]).

In section 5.2 we observe that the moist static energy in the stratosphere has increased enormously due to increased UV absorption by ozone. However, it is unclear how the different terms in equation 5.1 adjusts in response to the applied perturbation to achieve radiative equilibrium. Therefore, in this section we focus on comparing radiative flux terms in equation 5.1 in both O_3 perturbation experiments with the control.

5.3.1. TOA

The change in TOA upward and downward SW flux compared to the control run for both $x5O_3$ and $x5O_{3FSST}$ experiments is presented in figure 5.4. For easier interpretation, we choose to divide equation 5.1 by the Earth's surface area such that the plots in the rest of this section are in units of Wm^{-2} unless otherwise stated. In addition, due to the noise involved, the time series is also smoothed using a central moving average with a span of 29 days using equation 5.2.

$$F_t^{Smoothed} = \frac{F_{t-14} + F_{t-13} + .. + F_t + .. + F_{t+13} + F_{t+14}}{29} \tag{5.2}$$

Since no adjustment is made regarding the incoming solar flux in both $x5O_3$ and $x5O_{3FSST}$ runs, the downward SW radiation at TOA is exactly the same as the control run and its anomaly is therefore omitted in figure 5.4. On the other hand, it is observed that there is a reduction of upward SW at TOA in both cases, which is again an anticipated result. As incoming SW flux enters the atmosphere, about 30% [63] is reflected by clouds at different levels and also by the Earth's surface. In our ozone perturbation experiments,

the increased ozone absorption of solar radiation implies that there is less SW entering the troposphere. Since the majority of clouds lie within the moisture-rich troposphere, less SW radiation is available to be reflected into space. Upon reflection, the SW radiation passes through the greater ozone again which results in further absorption. Hence, in both ozone perturbation experiments, a decreased upward SW flux is observed at the TOA. The planetary albedo of the control run is 0.307 and is found to have reduced to 0.281 and 0.278 in the $x5O_3$ and $x5O_{3FSST}$ runs respectively.

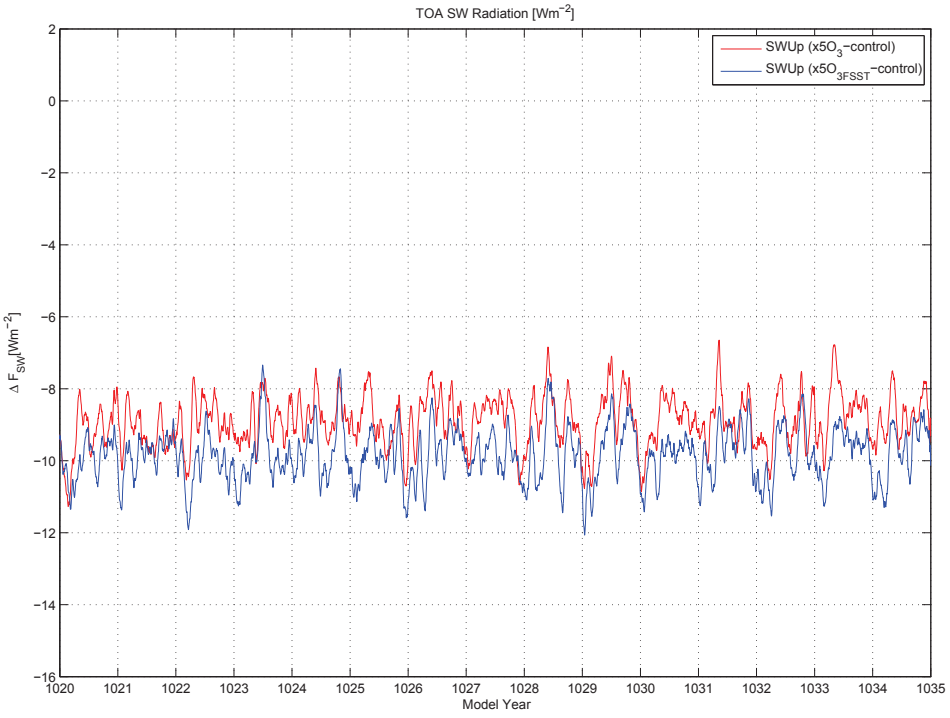


Figure 5.4.: Global mean upward shortwave radiative flux ($F_{SW\uparrow}$) anomalies at TOA for $x5O_3$ (Red) and $x5O_{3FSST}$ (Blue) [Wm^{-2}].

Figure 5.5 shows the longwave anomalies for both $x5O_3$ and $x5O_{3FSST}$. Note that the downward LW anomalies are omitted from the plot as there is no LW radiation from the Sun. The upward longwave flux has increased in both $x5O_3$ and $x5O_{3FSST}$ runs. In figure 5.1 we observed that there is enormous warming throughout the stratosphere due to increased UV absorption of ozone. As a result, $\Delta F_{LW\uparrow}$ is positive which implies enhanced

LW radiation emitted by the stratosphere into space and also into the troposphere (not shown).

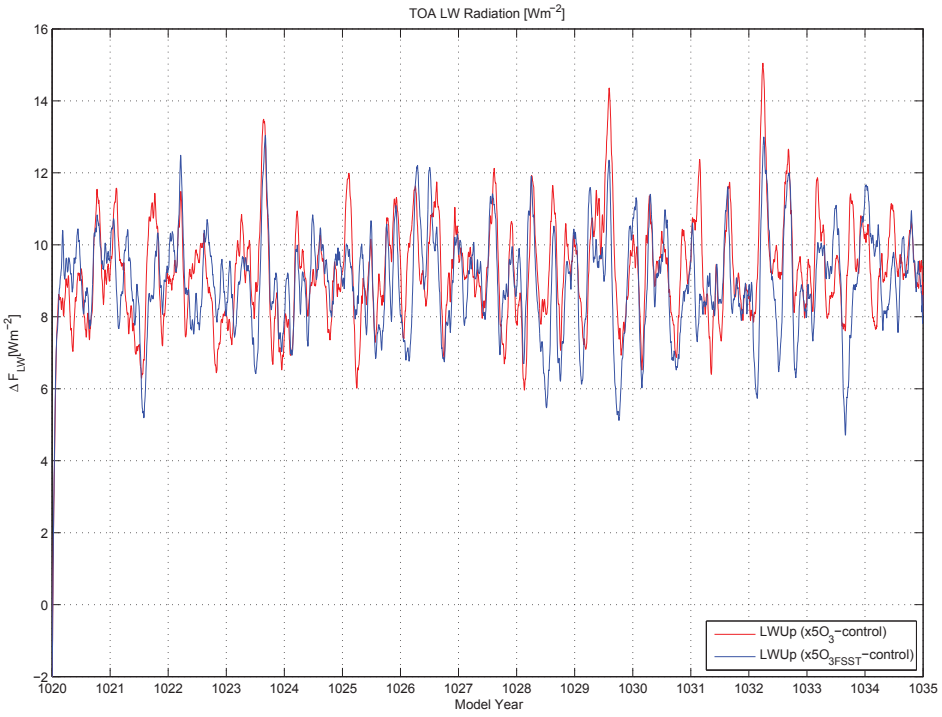


Figure 5.5.: Global mean upward longwave radiative flux ($F_{LW\uparrow}$) anomalies at TOA for $x5O_3$ (Red) and $x5O_{3FSST}$ (Blue) $[Wm^{-2}]$.

Previously in figure 2.17 we deduce that the control aquaplanet is close to but not in perfect equilibrium as there is a small drift in global mean sea potential temperature in year 1020. Since the heat content of the atmosphere is small compared to that of the ocean, the observed temperature drift implies a radiative imbalance at the TOA and there is a net inflow of energy into the system by radiation. The radiative imbalance (SW+LW) at the TOA averaged over the last 15 years for the control run is found to be $0.1097Wm^{-2}$.

The time series of the net effect of SW and LW radiative flux anomalies in response to the ozone perturbation is shown in figure 5.6. In both $x5O_3$ and $x5O_{3FSST}$ runs, there is a initial positive imbalance of $12Wm^{-2}$ at the

TOA which sharply reduces in magnitude such that the perturbed aquaplanet is in close radiative equilibrium. By comparing the SW and LW anomalies in year 1020 as shown in figure 5.4 and 5.5 we observe that the initial positive imbalance in net radiative flux is caused by a reduction in reflected SW at TOA. In contrast, it takes 30 days for the magnitude of $\Delta F_{LW\uparrow}$ to become comparable to that of $\Delta F_{SW\uparrow}$ in both experiments.

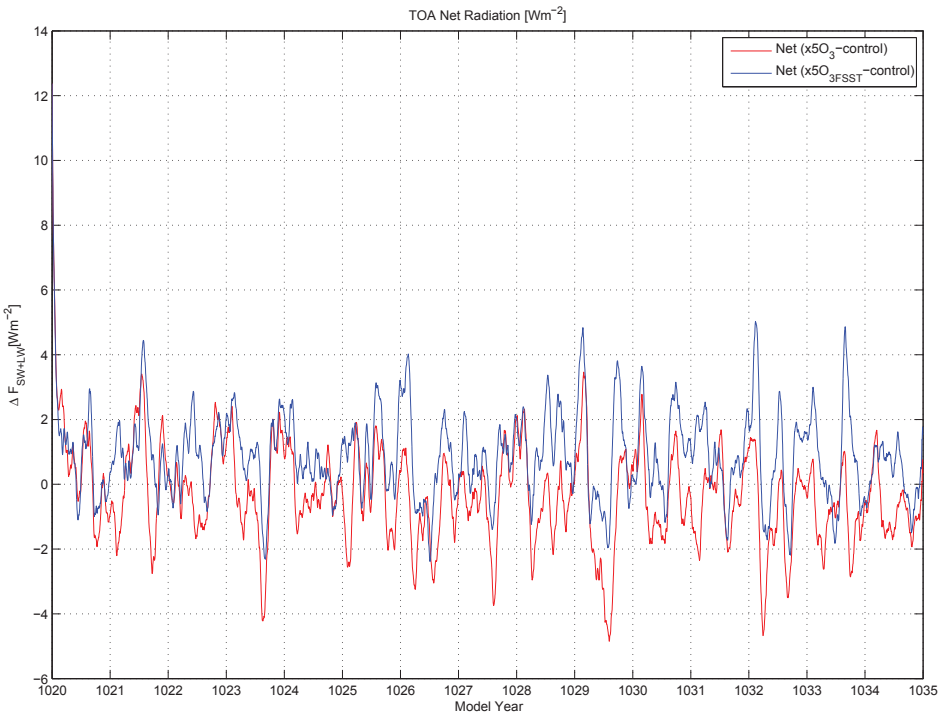


Figure 5.6.: Global mean net (SW+LW) downward radiative flux anomalies at TOA for $x5O_3$ (red) and $x5O_{3FSST}$ (blue) $[Wm^{-2}]$.

As the stratosphere heats up due to enhanced ozone absorption of UV, the increase in emitted LW by the stratosphere becomes comparable to the reflected SW anomalies at TOA. However, in neither of the ozone experiments do the SW and LW anomalies balance each other perfectly. Table 5.1 shows the time averaged values for the anomalies in each of the terms in equation 5.1. From section 3.3.2 we learn that the global mean SST has increased in response to an increased ozone concentration in the stratosphere in the $x5O_3$ run, which also implies increased LW emitted from the sea sur-

face. As a result, given the same perturbation in the stratosphere, there is more outgoing LW radiation and hence $\Delta F_{LW\uparrow}$ in $x5O_3$ is larger than that in the fixed SST run. However, the LW anomalies appear to be dominated by stratospheric heating as the difference of $\Delta F_{LW\uparrow}$ between the two ozone experiments is small compared to $\Delta F_{SW\uparrow}$.

	$x5O_3$	$x5O_{3FSST}$
$\Delta F_{SW\downarrow}$	0.00 ± 0.00	0.00 ± 0.00
$\Delta F_{SW\uparrow}$	-8.90 ± 0.20	-9.85 ± 0.14
$\Delta F_{LW\downarrow}$	0.00 ± 0.00	0.00 ± 0.00
$\Delta F_{LW\uparrow}$	9.24 ± 0.40 †	8.95 ± 0.23 †
$\Delta F_{Net\downarrow}$	-0.35 ± 0.52 †	0.90 ± 0.25

Table 5.1.: Change in SW and LW radiative flux at TOA, averaged over year 1020-1035 [Wm^{-2}]. The standard deviations of their annual means are also shown. Terms that have a negative contribution to the energy of the system are marked with †.

The discrepancies between the magnitudes of $\Delta F_{SW\uparrow}$ at the TOA in $x5O_3$ and $x5O_{3FSST}$ can be explained by comparing the amount of cloud cover in the two experiments. Table 5.2 lists the cloud fractions of all the cloud types in FORTE for both $x5O_3$ and $x5O_{3FSST}$ runs. It is observed that there are more middle and low clouds in the $x5O_3$ experiment. The enhanced SW absorption by ozone is partially compensated by changes in cloud cover such that there is less reduction of reflected SW at TOA in $x5O_3$ compared to the $x5O_{3FSST}$ run.

Unlike the other clouds, convective clouds are related to the precipitation rate (see equation 2.4) but not relative humidity in the model. The more convective cloud cover in the fixed SST experiment simply imply a higher rate of precipitation, as its troposphere is less able to hold moisture than that of $x5O_3$, which is considerably warmer. Regarding cloud optical properties, the SW optical depth of convective clouds are on the same order as low and middle clouds in IGCM's SW scheme [45]. A rough estimate shows that, with the assumption that all cloud types have the same optical properties, the differences in cloud cover could account for $0.485 Wm^{-2}$ of reflected SW, and is large enough to explain about half of the discrepancies

in $\Delta F_{SW\uparrow}$. Hence, as inferred from table 5.2, our previous argument on less reduction of reflected SW at TOA in $x5O_3$ compared to the $x5O_{3FSST}$ run remains valid, mainly due to low and middle cloud cover anomalies.

Referring to table 5.1, from the aspect of radiative forcing at the TOA, the SW and LW flux anomalies suggest there is a net energy loss in the fully coupled aquaplanet when stratospheric ozone is perturbed and increased by 5 times. In contrast, there is a net inflow of energy at the TOA into the system in the case when the SST is fixed. In $x5O_{3FSST}$, MOMA supplies IGCM3 with the same sea surface temperature at the end of each model day, ignoring all surface forcings (including radiative and heat fluxes) on the ocean by the overlying air. Hence, the ocean in the $x5O_{3FSST}$ can be thought as a infinite energy sink and the above statement of net energy gain by radiative imbalance cannot be considered as a solid statement about the energy content of the system in the case of the fixed SST aquaplanet as energy is not conserved.

Figure 5.7 shows a 360-day-smoothed time series of globally integrated net radiative flux at TOA for control, $x5O_3$ and $x5O_{3FSST}$, from which it is observed that the TOA imbalance in $x5O_{3FSST}$ does not evolve like the $x5O_3$ run does. As mentioned earlier, the initial positive imbalance in both experiments is dominated by a reduction of reflected SW. In the $x5O_3$ run, as the SST increases via the mechanism discussed in section 3.4.2, the positive imbalance is gradually cancelled by a supplement of LW radiation from the surface. Three years after the perturbation, the sea surface continues to heat up due to ocean dynamics and F_{Net} overshoots and becomes negative. The imbalance remains negative till the end of the experiment and suggests that the model has not reached its new radiative equilibrium.

	$x5O_3$	$x5O_{3FSST}$
$High$	0.387	0.387
$Middle$	0.265	0.261
Low	0.304	0.302
$Convective$	0.235	0.237

Table 5.2.: Global mean cloud fraction for high, middle, low and convective clouds for $x5O_3$ and $x5O_{3FSST}$ runs.

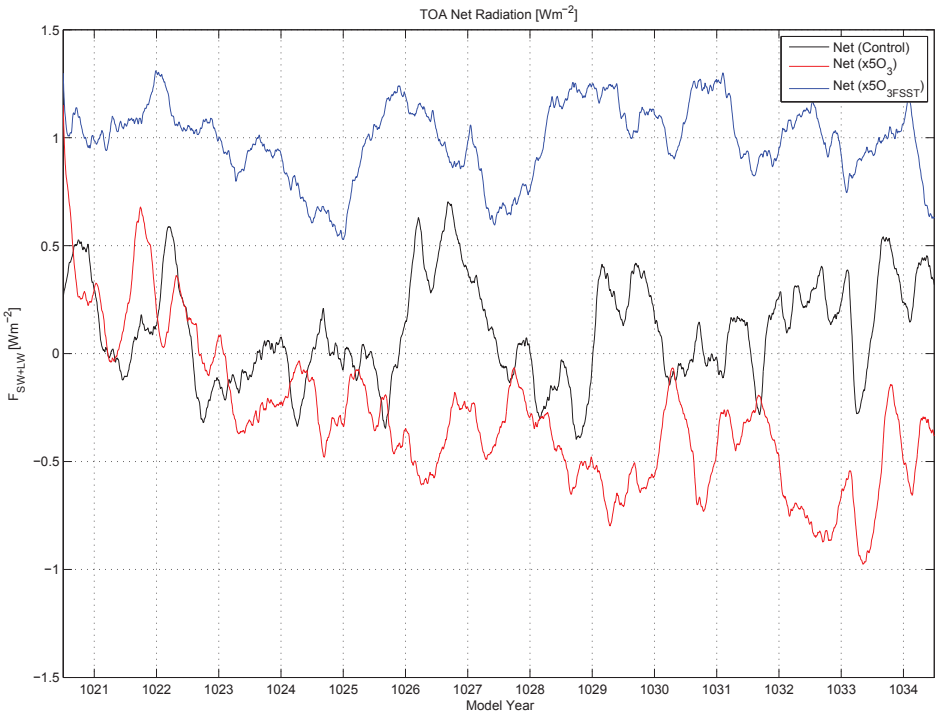


Figure 5.7.: Time series (360-day-smoothed) of global mean net (SW+LW) downward radiative flux at TOA for control (black), $x5O_3$ (red) and $x5O_{3FSST}$ (blue) $[Wm^{-2}]$.

5.3.2. Surface

At the surface, apart from radiative transfer, energy exchange between surface air and the ocean also takes place in the form of latent and sensible heat flux. As surface water evaporates due to excessive solar heating, an extra amount of energy is needed to support the phase change of water from liquid to gas. This is known as the latent heat and is specified by $L_v q$, where L_v is the latent heat of vaporisation and q is the specific humidity. Atmospheric temperature is independent on the amount of latent heat content in the air parcel until it is cold enough for condensation to occur such that latent heat is released to the surrounding atmosphere. In contrast, sensible heat is the heat transfer via conduction and convection and results in a change of temperature.

Hence, the energy budget equation as shown in equation 5.1 has to be modified for the surface and becomes,

$$F_{Net}^{Surf} = F_{SW\downarrow}^{Surf} - F_{SW\uparrow}^{Surf} + F_{LW\downarrow}^{Surf} - F_{LW\uparrow}^{Surf} - F_{Latent\uparrow} - F_{Sensible\uparrow} \quad (5.3)$$

where $F_{Latent\uparrow}$ and $F_{Sensible\uparrow}$ are the upward latent and sensible heat flux in Wm^{-2} respectively. The superscript ^{Surf} denotes radiative flux at surface level.

The surface upward and downward SW anomalies are shown in figure 5.8. As mentioned in section 5.3.1 the planetary albedo of the $x5O_3$ aquaplanet is higher than that of $x5O_{3FSST}$. Hence we expect less downward SW radiation arriving at the sea surface which is indeed observed in figure 5.8. On the other hand, the reflected SW is also reduced in $x5O_3$ relative to $x5O_{3FSST}$ but because the surface is covered with water $\Delta F_{SW\uparrow}^{Surf}$ is small in both experiments. Hence, there is net SW cooling of the ocean.

Regarding surface LW anomalies, in the $x5O_{3FSST}$ run where the SST is fixed we expect minimal changes to the upward LW flux. This is confirmed in figure 5.9 where upward LW anomalies in the fixed SST run is found to oscillate around the zero line. In the $x5O_3$ run where the SST has increased due to a weakening of the Ekman cells in the ocean as described in section 3.2, the upward LW flux at the surface is also expected to increase. Note

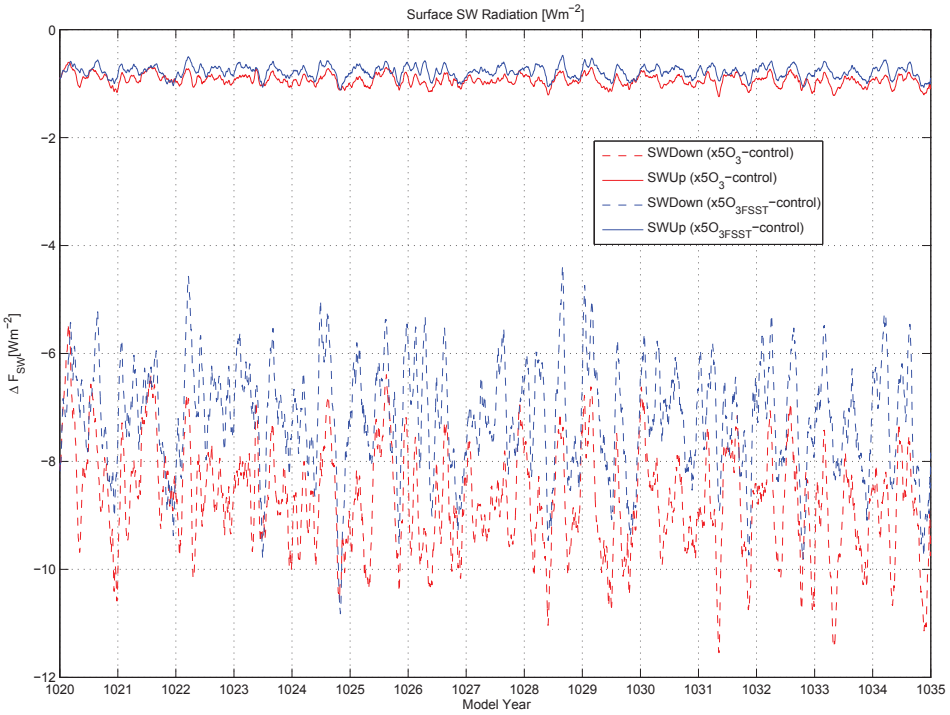


Figure 5.8.: Global mean upward (solid) and downward (dashed) shortwave radiative flux anomalies at sea surface for $x5O_3$ (red) and $x5O_{3FSST}$ (blue) $[Wm^{-2}]$.

the anomalies in upward LW in the $x5O_3$ run is not uniform like the SW but increases over the span of the experiment. This suggests the system is not in equilibrium and surface water is still warming via the dominant mechanism described in section 3.4.2 15 years after the ozone perturbation is applied.

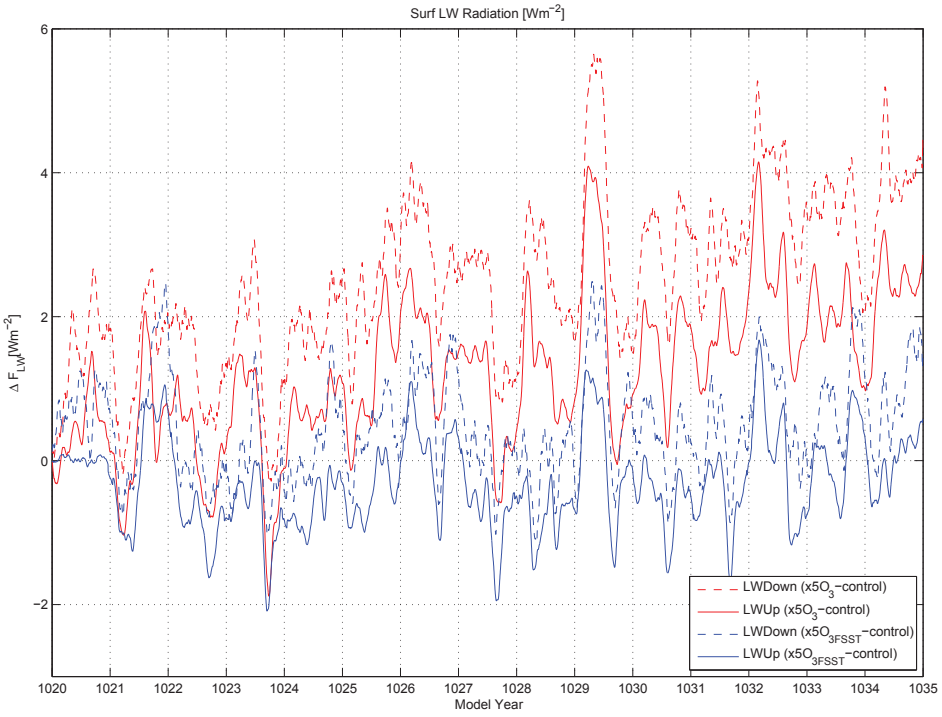


Figure 5.9.: Global mean upward (solid) and downward (dashed) longwave radiative flux anomalies at sea surface for $x5O_3$ (red) and $x5O_{3FSST}$ (blue) $[Wm^{-2}]$.

Figure 5.10 shows the latent and sensible heat flux anomalies for both $x5O_3$ and $x5O_{3FSST}$ runs. In both cases, the contrast in temperature between the surface water and the overlying air is small such that the latent heat flux anomalies dominate over that of the sensible heat flux. Referring to figure 3.1, the surface windstress has weakened in the $x5O_3$, which limits the rate of evaporation of sea water. As a result, there is less latent heat transferred from the ocean to the atmosphere per unit time. Similar arguments apply to the $x5O_{3FSST}$ case.

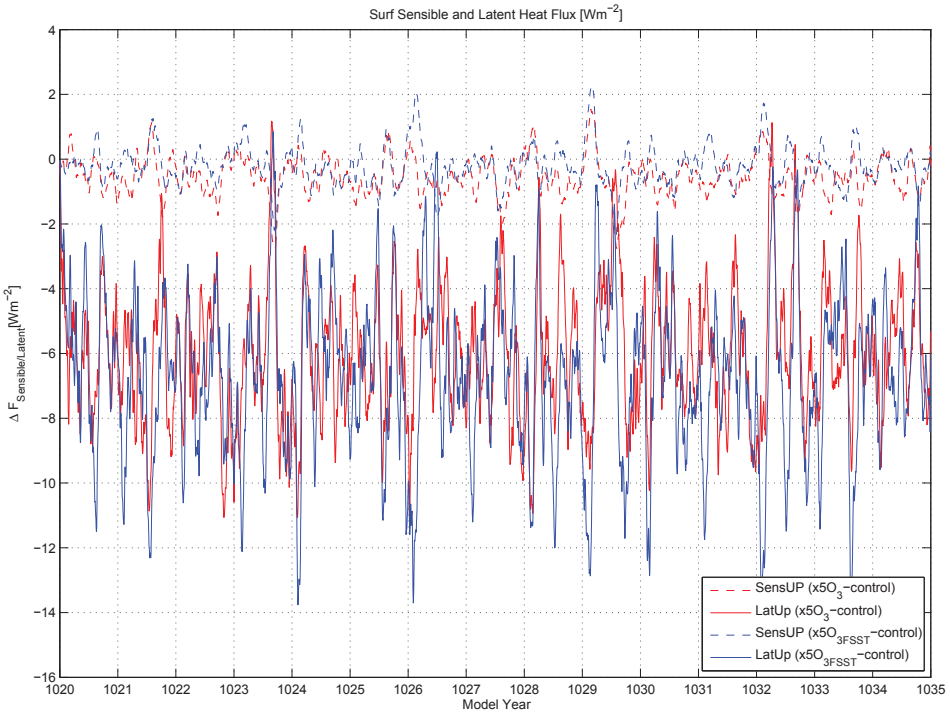


Figure 5.10.: Global mean upward latent (solid) and sensible (dashed) heat flux anomalies at sea surface for $x5O_3$ (red) and $x5O_{3FSST}$ (blue) $[Wm^{-2}]$.

The time-averaged values for the anomalies of each of the terms in equation 5.3 is presented in table 5.3. The dominant term in both experiments is $\Delta^{Surf}_{SW\downarrow}$ (a direct consequence of enhanced ozone absorption of incoming solar radiation as described before), which is largely compensated by a reduction of latent heat flux into the atmosphere. The reduction in upward latent heat flux in the $x5O_{3FSST}$ is more severe than the $x5O_3$ case, which agrees with the fact that the fixed SST run has a lower specific humidity than the fully coupled experiment. The specific humidity for $x5O_3$ and $x5O_{3FSST}$ are found to be $3.0549g/kg$ and $2.9898g/kg$ respectively.

Due to the nature of the fixed SST and fully coupled experiments, the upward and downward longwave anomalies are bound to be different for the $x5O_3$ and $x5O_{3FSST}$. However, in both cases, the net effect of the LW anomalies ΔF^{Surf}_{LWNet},

$$\Delta F^{Surf}_{LWNet} = \Delta F^{Surf}_{LW\downarrow} - \Delta F^{Surf}_{LW\uparrow} \tag{5.4}$$

does not exceed the difference of the two dominant terms in the budget ΔF^{Surf}_{Dom}, where

$$\Delta F^{Surf}_{Dom} = \Delta F^{Surf}_{SW\downarrow} - \Delta F^{Surf}_{Latent\uparrow} \tag{5.5}$$

For instance, ΔF^{Surf}_{LWNet} is $1.240Wm^{-2}$ for $x5O_3$ and $0.785Wm^{-2}$ for $x5O_{3FSST}$. On the other hand, there is a larger difference in the ΔF^{Surf}_{Dom} term between the two experiments, which is calculated to be $-2.661Wm^{-2}$ ($x5O_3$) and $-0.469Wm^{-2}$ ($x5O_{3FSST}$) respectively. This suggests that contrast in surface energy budget is not predominately affected by direct LW effects but by other factors. In the case of our experiment, these include a different evaporation rate and cloud cover, both as a consequence of the weakening of the surface winds.

In both cases, the net effect at the surface is that there is an energy flux anomaly of $0.080Wm^{-2}$ and $1.315Wm^{-2}$ into the ocean over the last 15 year of model run in $x5O_3$ and $x5O_{3FSST}$ respectively. This implies that in our ozone perturbation experiment, the atmosphere loses more energy to the ocean when the SST is held fixed. Although this does not explain the latitudinal structure of the air temperature anomaly as shown in figure 5.2,

we gain an insight of why there is a significant temperature increase (except for polar regions) of surface air in the fully coupled run while not observed in the fixed SST experiment. The time series of the net energy flux anomaly at the surface is presented in figure 5.11.

	$x5O_3$	$x5O_{3FSST}$
$\Delta F^{Surf}_{SW\downarrow}$	-8.71 ± 0.35 †	-7.18 ± 0.20 †
$\Delta F^{Surf}_{SW\uparrow}$	-0.94 ± 0.04	-0.78 ± 0.02
$\Delta F^{Surf}_{LW\downarrow}$	2.50 ± 0.89	0.47 ± 0.40
$\Delta F^{Surf}_{LW\uparrow}$	1.24 ± 0.76 †	-0.32 ± 0.37
$\Delta F_{Sensible\uparrow}$	-0.55 ± 0.10	-0.22 ± 0.11
$\Delta F_{Latent\uparrow}$	-6.04 ± 0.34	-6.71 ± 0.44
$\Delta F^{Surf}_{Net\downarrow}$	0.08 ± 0.40	1.32 ± 0.43

Table 5.3.: Change in radiative, sensible heat and latent heat flux at surface, averaged over year 1020-1035 [Wm^{-2}]. The standard deviations of their annual means are also shown. Terms that have a negative contribution to the ocean heat content are marked with †.

Finally, to justify the validity of energy exchange between the atmosphere and the ocean in FORTE, the time integrated global surface energy flux at the surface and the gain in ocean heat content for the control run is plotted in figure 5.12. Despite the small residual, which is due to the fact that the surface flux is integrated over both the ocean and the polar caps, it is observed that the net energy flux into the ocean agrees well with its heat content increase.

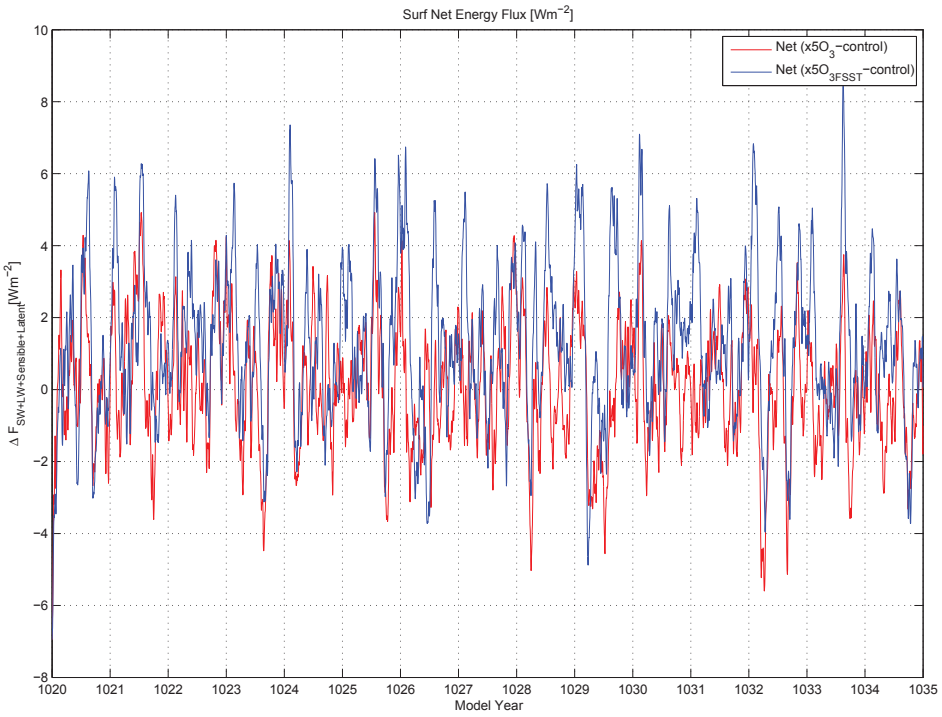


Figure 5.11.: Global mean net (SW+LW+sensible+latent) downward energy flux anomalies at sea surface for $x5O_3$ (Red) and $x5O_{3FSST}$ (Blue) $[Wm^{-2}]$.

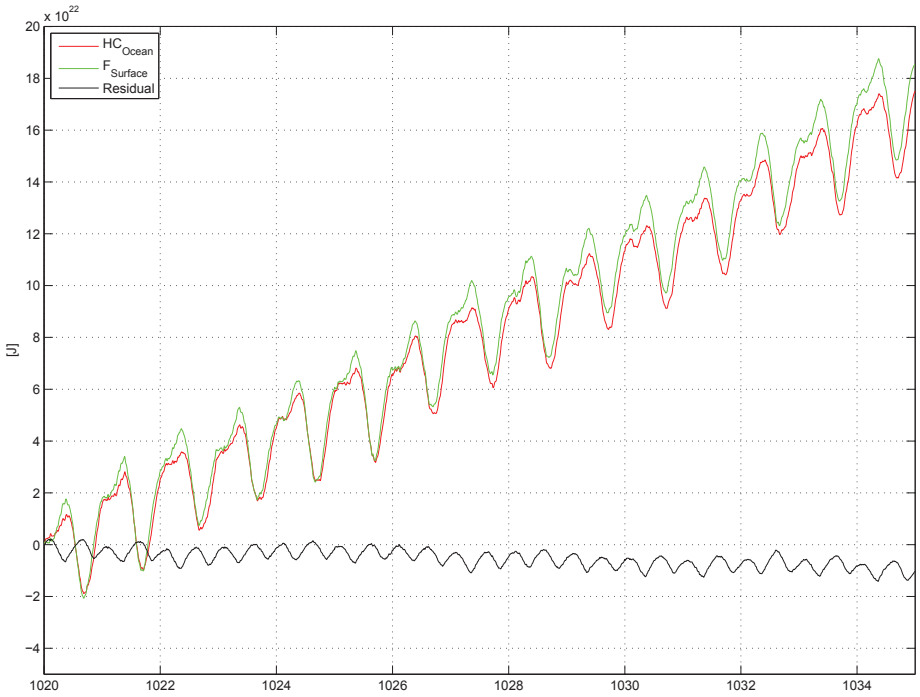


Figure 5.12.: Time series of gain in ocean heat content (red) and time-integrated total net downward energy flux at the surface (green) since year 1020 for the control run [J]. Residual of the two is shown in black.

5.4. Remarks

Regarding the total energy content (atmosphere + ocean, neglect kinetic energy) of the $x5O_3$, we observe an increase in both the moist static energy of the atmosphere (figure 5.3) and total ocean heat content in response to the applied perturbation. Theoretically, this should equal to the net radiative flux anomalies at TOA. However, our results from our radiative flux analysis in section 5.3.1 suggest that the system should be losing energy and therefore contradicts with our findings.

Figure 5.13 highlights the difference between the net energy flux into the atmosphere and the actual moist static energy change since year 1020 for the control run. In theory the residual between the two should be zero which is clearly not true in our case. From figure 5.12 we learn that the surface flux corresponds to the change in ocean heat content. Given that the atmosphere does conserve heat exactly (personal communication with Sinha B. from National Oceanography Centre, Southampton), this suggests that the TOA flux from the model output could be wrong. Therefore, it is not possible for any further analysis to be made on the energy budget of the system until the issue is resolved. Nevertheless, we still manage to obtain an insight of the changes in ocean heat content in our five times ozone experiment.

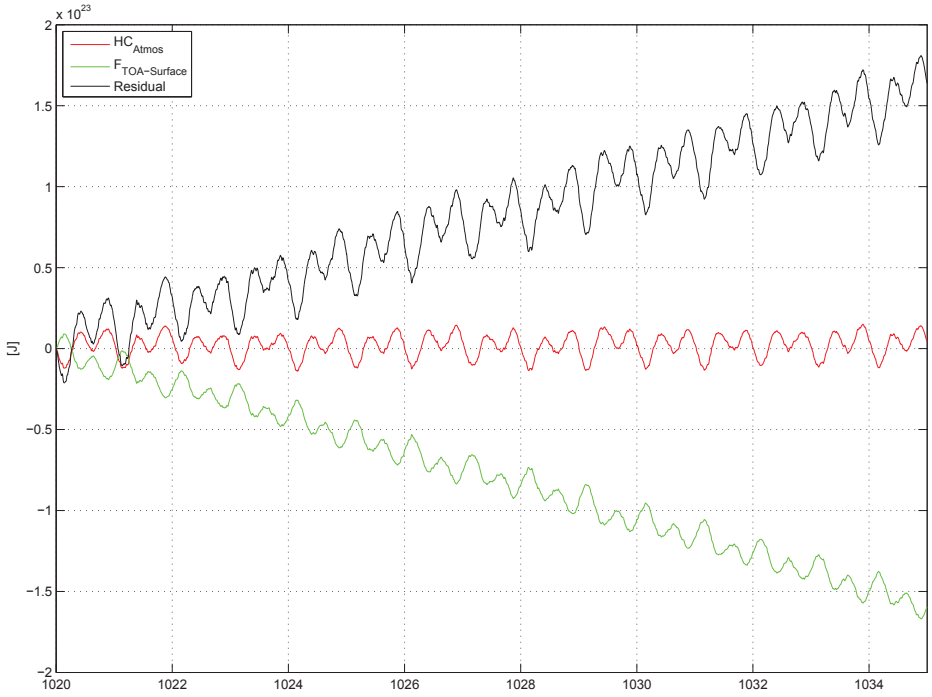


Figure 5.13.: Time series of gain in moist static energy (red) and time-integrated net (TOA-Surface) global energy flux into the atmosphere (green) since year 1020 for the control run [J]. Residual of the two is shown in black.

5.5. Summary and Conclusions

In this chapter we demonstrated how the air temperature changes in response to the applied ozone perturbation and highlighted the difference in latitudinal tropospheric response. We have also analysed the radiative and heat fluxes at both the TOA and the surface in an attempt to explain the observed changes in moist static energy in the atmosphere and the ocean heat content. We find the following:

- The stratosphere has warmed up by a maximum of $30K$ at the tropics and $20K$ at the poles due to enhanced UV absorption by ozone in both experiments. The heating is non-uniform in latitude such that the meridional temperature gradient in the stratosphere is altered and becomes a driver of zonal wind anomalies.

- There is a general increase in temperature in the troposphere except for latitudes higher than 60^o in the $x5O_3$ run. In contrast, latitudinal bands of positive and negative tropospheric temperature anomalies is observed in the case of the fixed SST run.

- At the TOA, there is reduced reflected SW and increased outgoing LW radiation due to increased UV absorption by ozone. The upward LW anomaly is dominated by stratospheric heating rather than difference in surface SST. The discrepancies in the SW anomalies between the two experiments is potentially affected by the amount of cloud cover.

- Despite the difference in SST conditions, the surface energy budget is dominated by downward SW and latent heat anomalies. In both $x5O_3$ and $x5O_{FSST}$, the net effect at the surface is that there is net energy inflow into the ocean.

6. Summary and Conclusions

The first chapter of this thesis began with an in-depth review on past stratosphere-troposphere coupling studies. This was followed by an overview of the Earth's general circulations, which included both atmospheric and oceanic features such as Hadley cells, mid-latitude jet streams, surface winds, Ekman cells and thermohaline circulation. These discussions highlighted the fact that the models used in existing stratosphere-troposphere coupling studies do not have an interactive ocean present. Considering the vast variability that is associated with air-sea interactions such as ENSO, we are motivated to investigate into the ocean's dynamical response to thermal forcing in the stratosphere (chapter 3), and its subsequent feedback to the general circulation in the atmosphere (chapter 4). This was achieved by using a fully coupled atmosphere-ocean model with an idealised aquaplanet setup. Instead of applying a direct thermal perturbation to the stratosphere, we chose to increase the concentration of stratospheric ozone by five times. Despite an unrealistic perturbation, it allowed responses relevant to the goal of this thesis to be identified more clearly. To date, there are a number of studies that suggest correlations between the 11-year solar cycle and various aspects of Earth's climate (e.g. [35, 36, 37, 38]). As far as ozone is concerned, there are both SW and LW forcings associated with solar activity. For instance, during solar maximum, the downward SW entering the troposphere reduces as a result of increased UV absorption by ozone. At the same time, the extra ozone heating in the stratosphere enhances its LW radiation. Hence, the choice of applying a perturbation to stratospheric ozone over a direct thermal forcing in the stratosphere allows a more complete study of the role of the ocean in ST coupling. An analysis regarding changes to radiation and heat budgets in our perturbation experiments was presented in chapter 5.

Idealised aquaplanet is not the most common type of model setup in ST

coupling studies. In addition, the climatology of an aquaplanet vary from model to model (e.g. [42, 59]) and hence there is no easy answer to what the climate of an aquaplanet should look like. For the purpose of our study, our aquaplanet model was spun up from a standard reference state for 1020 model years until the ozone perturbation was applied. The climatology of our aquaplanet was described in chapter 2, with various key features described as follows:

Atmosphere

- Compared to real world climatology, the aquaplanet air temperature is warmer, especially at the polar regions where the annual mean surface temperature is 6^oC.
- The global mean rainfall in the aquaplanet is $3.89mmday^{-1}$, which is 45% higher than real world observation. The rainfall distribution is zonally uniform, with two ITCZs at 10^oN and 10^oS.
- The strength of the aquaplanet jetstream is slightly weaker compared to reality, and is located higher up in the atmosphere than expected.
- The meridional circulation in our aquaplanet consists of four cells - the standard Hadley, Ferrel & polar cell and an unique 'inverted' cell which is located between $0^o - 10^o$. The 'inverted' cell is driven by the local SST minimum at the equator and is responsible for the unusually strong easterlies in the upper troposphere at the tropics.
- The end state of the control aquaplanet is at close but not perfect radiative equilibrium, with a net downward TOA flux of $0.110Wm^{-2}$. The planetary SW albedo is found to be 0.307.

Ocean

- The surface currents are found to be zonally symmetrical, as there is no continient to support ocean gyres.
- The meridional overturning circulation is mainly wind-drive, and consists of three Ekman cells that extends from the surface to the bottom of ocean. The locations of these cells coincide with the surface wind field and spans over 30^o in latitude each.

- The upwelling branch of the tropical Ekman cell carries cold water from the depths of the ocean, which results in a cold tongue at the equator. The resultant SST distribution is responsible for the 'inverted' cell observed in the atmosphere.

- The temperature drift of global mean sea potential temperature is found to be $0.007K$ per decade by the end of model year 1035. As with the TOA radiative flux, this suggests the control aquaplanet is not at perfect equilibrium.

Following the aquaplanet climatology as described in chapter 2, chapter 3 focused on the ocean's response to the applied ozone perturbation. From previous literature (e.g. [22, 50, 56, 68]), it was shown that the thermal perturbations in the stratosphere would alter the tropospheric circulation, and hence changing the surface wind stress. This motivated an investigation into corresponding changes in the strength of MOC in our aquaplanet, and its subsequent impact on the vertical structure of ocean heat content. The key results of chapter 3 are summarised as follows:

- In our aquaplanet where the ocean MOC was dominated by wind-driven Ekman transport, the strength of the MOC was found to decrease at all latitudes in response to the surface wind anomalies in the $x5O_3$ run. In response to the meridional expansion of surface westerlies at mid-latitudes, the Ekman cell originally centered at about 45^o was also found to extend towards to the pole.

- The SST in $x5O_3$ was found to be warmer than the control SST by $0.4K$ 15 years after the ozone perturbation had been applied. However, the rate of increase in SST was not linear over time span of the experiment (15 years). No clear sign of SST increased was observed in the first four years of ozone experiment.

- An analysis of the vertical structure of the internal energy of the ocean confirmed that, there was a transfer of heat content to the top layers $(0-400m)$ of the ocean from sea water below, and hence contributing towards a warmer SST.

- A mechanism explaining the observed upward transport of ocean heat content, which involved reduced upward advection of sea potential

temperature, was identified. To first order, the change in vertical structure of ocean heat content of $x5O_3$ due to the proposed mechanism was found to be consistent with the observed anomalies.

In chapter 4, we focused on the comparison of the dynamical response of the troposphere to ozone in $x5O_3$ and $x5O_{3FSST}$, in which the two runs are identical except that the SST is held constant (with a seasonal cycle) in the latter. For each experiment, we also performed an analysis on the zonal mean momentum equation (equation 1.18 and evalutated the importance of each of the terms to the momentum budget of the atmosphere. The key results of chapter 4 are detailed as follows:

- In both $x5O_3$ and $x5O_{3FSST}$, a weakening and equatorward shift of the jet stream were observed, and is qualitatively consistent with that observed in the literature (e.g. HBD05). Despite the similarities, the zonal wind response in the $x5O_{3FSST}$ run was found to be more pronounced than that in $x5O_3$.

- Regarding the meridional circulation in the atmosphere, all of the 'inverted', Hadley and Ferrel cells were weakened in response to the applied ozone in both experiments. In the $x5O_3$ where the SST was higher than that of $x5O_{3FSST}$ due to ocean dynamics, the weakening of the meridional cells was partially balanced by increased convection of air. Hence, the weakening of the meridional cells in $x5O_3$ is not as pronounced as $x5O_{3FSST}$.

- Equatorward shifts of the Hadley and Ferrel cells were found, and hence shrinking the width of the 'inverted' cell in both experiments. In $x5O_{3FSST}$, the fixing of the SST constrained the location of the meridional cells to a certain extent. Hence, the shifting in $x5O_{3FSST}$ was not as distinct as that in $x5O_3$.

- By decomposing the wind field into a sum of its time mean and instantaneous fluctuation from the time mean flow, we were able to compare the structure of mid-latitude eddies ($[\overline{u'v'}]$) of the control run with that observed in NCEP-NCAR analysis data. In the winter hemisphere of the aquaplanet, the eddy momentum transport at mid-latitude was found to be contributed by waves of wavenumber

$k = 4 - 7$, with a magnitude comparable to real world observations. In the summer hemisphere, the mid-latitude eddy momentum transport at these wavenumbers was found to be much weaker than that obtained using NCEP-NCAR data.

- A net transport of eddy momentum flux by wavenumber $k = 0 - 3$ was found at the equator, transferring momentum from the SH to the NH. This implied that the equatorial easterlies in our aquaplanet took the form of a Rossby wave and also that the zonal mean fluctuated heavily with time.

- It was found that the asymmetrical eddy momentum transport across the equator vanished when the clouds were ignored in the LW radiation scheme in IGCM3. The exact origin of the unusual eddy momentum flux had not been identified.

- An analysis on the zonal mean zonal momentum equation (equation 1.18) showed that the divergence of the eddy momentum flux anomalies ($\frac{\partial[u^*v^*]cos^2\phi}{\partial\phi}$) is consistent with the zonal wind changes in $x5O_3$. The eddy momentum flux anomalies in $x5O_{3FSST}$ showed a similar pattern, but with a stronger eddy response such that the anomalous meridional eddy flux gradient was steeper. As a result, a more pronounced weakening of the jet stream was found in $x5O_{3FSST}$ compared to that with a coupled ocean.

- Although the contribution from mean circulation to the vertically integrated zonal momentum budget is generally small compared to that from eddies and friction, the results from our ozone perturbation experiments show that the mean flow does contribute to the equatorward displacement of the jets when there is an interactive ocean, while this is not the case when the SST is fixed.

- A possible mechanism in explaining the difference in zonal wind response in the presence of an interactive ocean is proposed. The weakening of the meridional cells caused by ozone heating in the stratosphere is partially compensated by enhanced SST-induced convection in the $x5O_3$ run. As a result, there is less forcing on zonal wind by anomalous meridional circulation. Hence, the effects of eddy feedback described in SBH09 is also reduced when there is an interactive ocean.

As introduced earlier in this section, the introduction of extra ozone in the stratosphere would reduce the amount of downward SW entering the troposphere while the troposphere would receive augmented LW from stratospheric heating. In the first part of chapter 5, the air temperature anomalies were studied and the key results are summarised as follows:

Stratosphere

- The stratosphere was found to warmed by an enormous amount (maximum $30K$) due to increased UV absorption by ozone in both experiments. The altered meridional temperature gradient was found to be consistent with the zonal wind anomalies in the stratosphere.
- As radiative effects are almost instantaneous, the globally integrated moist static energy of the stratosphere was found to increased sharply over the first 90 days and remained approximately constant for the rest of the experiment.

Troposphere

- In $x5O_{3FSST}$, the tropospheric temperature anomaly showed latitudinal bands of warming and cooling, in a similar fashion as described in HBD05. In $x5O_3$, an increase in tropospheric temperature was observed at all latitudes lower than 60^o.
- In contrast to the stratosphere, the globally integrated moist static energy of the troposphere increased by $6 \times 10^{21} J$ over 15 model years in $x5O_3$ while no significant increase was observed in $x5O_{3FSST}$.

We then focused on the radiative aspects in an attempt to explain the observed heat budget anomalies in the experiments:

TOA

- In both experiments, the outgoing LW at the TOA $F^{TOA}_{LW\uparrow}$ was found to increase due to ozone heating in both experiments. Despite the same perturbation, there was a positive contribution by the warm SST in

$x5O_3$ and hence $\Delta F^{TOA}_{LW\uparrow}$ in $x5O_3$ was observed to be larger than that of $x5O_{3FSST}$.

- In response to increased ozone, a reduction in reflected SW was observed as expected. The middle and low cloud fractions in $x5O_3$ were found to be higher than that in $x5O_{3FSST}$. As a result, the enhanced SW absorption by ozone was partially compensated by the difference in cloud cover such that there is less reduction of reflected SW at TOA in $x5O_3$ compared to $x5O_{3FSST}$.

- The net downward flux (SW+LW) anomalies for $x5O_3$ and $x5O_{3FSST}$ were found to be -0.348 ± 0.517 and 0.893 ± 0.252 respectively.

Surface

- In both $x5O_3$ and $x5O_{3FSST}$, the surface energy (SW+LW+latent+sensible) flux anomaly was dominated by the reduction of downward SW flux (due to enhanced UV absorption by ozone). This was found to be largely compensated by a decrease in latent heat flux into the atmosphere.

- It was found that the difference in surface flux balances between $x5O_3$ and $x5O_{3FSST}$ was not predominately affected by contrast in LW effects but by difference in evaporation rate and cloud cover, both as a direct consequence of the weakening of the winds.

- When averaged over the time span of experiment, an increase in net downward surface energy flux of magnitude 0.080 ± 0.402 was found in $x5O_3$. The observed surface flux anomalies were also found to be consistent with the total change in ocean heat content.

- The change in moist static energy was found to be inconsistent with the net energy flux anomalies into the atmosphere (TOA-Surf). It was concluded that there could be errors in the TOA flux output from FORTE, and hence the apparent paradox.

In conclusion, our results show that there are two key differences when an AOGCM is used in ST coupling studies. In the context of atmospheric dynamics, the jet stream's response to increased stratospheric ozone is weaker where there is an interactive ocean present in the model. However, the jet

streams are displaced to a greater extent by the mean flow when the SST is not fixed. On the other hand, the tropospheric temperature anomaly in our coupled experiment lack the banded structure observed in our fixed SST run and other literature (e.g. HBD05).

Our analysis described above, together with the work of SBH09, leads us to propose a mechanism whereby ocean dynamics influence the tropospheric zonal wind response to thermal forcing in the stratosphere. We find that the mechanism suggested by SBH09 holds in both of our ozone experiments, except in the case of $x5O_3$, the anomalous meridional circulations in the atmosphere that are responsible for driving changes to zonal wind anomalies are partially compensated by enhanced convection caused by the warmer SST. Hence, the effects of eddy feedback described in SBH09 are also reduced. This results in a weaker but similar zonal wind response compared to $x5O_{3FSST}$.

We confirm that an interactive ocean does have a significant effect on the results of our idealised ozone perturbation experiments. Although its exact impact on real world scenario simulation experiments is yet to be determined, our work suggests future ST coupling studies will benefit from using a fully coupled AOGCM.

6.1. Future Work

The aim of this project was not to reproduce what is observed in real world scenario but to understand the role of the ocean in ST coupling using an idealised aquaplanet model. In chapter 2 we identified a strong flow of easterly wind at the tropics, with a magnitude comparable to the core of the mid-latitude jet stream. Although later in section 4.3 we managed to get an insight on the structure of the flow, the exact causes of the equatorial easterlies and the unusual wave activities in the tropics remained unknown. In a similar aquaplanet setup by [42], the westward flow at the tropics is not as strong (only 40% of the core of their jet stream) as the one in our study. Although there is no real answer to what the climate of an aquaplanet should look like, it is worthwhile to compare different aquaplanet models and investigate into the origin the concerned easterlies in our study.

In our aquaplanet where there was no barrier in the ocean, there was no east-west pressure gradient to support zonally asymmetrical flow (e.g. ocean gyres) in the ocean. Hence, ocean current around a latitude circle was uniform in our aquaplanet and consequently lacked the zonal variations of SST required to drive atmospheric circulations like the Walker cells, in the zonal and vertical direction. Therefore, future work could involve repeating our ozone experiments in a setup where the zonal flow of water is restricted by the introduction of barriers similar to those described in [60] (see figure 2.1).

In chapter 5 we found a general increase in tropospheric temperature in response to the applied ozone perturbation in $x5O_3$, which lacked the latitudinal bands observed in the tropospheric temperature anomalies of $x5O_{3FSST}$ and other fixed SST ST coupling experiments (e.g. HBD05). Considering the fact that the energy exchange between the atmosphere and the ocean was exact and IGCM3 does conserves heat, we concluded that the TOA radiative flux in the output file could be wrong. Although the TOA-surface imbalance was small ($-0.669W^{-2}$ in the control run) compared to other studies (for instance, in the Bergen climate model [46], the TOA flux is $2.4Wm^{-2}$ while only about $0.1Wm^{-2}$ of that is stored in the ocean based on its heat content change described in the paper), it is difficult to address the exact mechanism causing the difference in tropospheric temperature response in our experiments, which is on the order of $0.1 - 1K$. Once the problem of having incorrect fluxes at the TOA has been fixed, we would be able to identify the cause of the lack of banded tropospheric response by considering columns of air confined in specific latitude bands and calculating their divergences of energy inflow by dynamical and radiative processes, and hence making our study complete.

Bibliography

[1] David G. Andrews. *An Introduction to Atmospheric Physics*. Cambridge, 2000.

[2] M. P. Baldwin. Comment on "tropospheric response to stratospheric perturbations in a relatively simple general circulation model" by lorenzo m. polvani and paul j. kushner. *Geophysical Research Letters*, 30(15):–, 2003. 713PN Times Cited:2 Cited References Count:10.

[3] M. P. Baldwin. Atmosphere: How will the stratosphere affect climate change? *Science*, 316(5831):1576, 2007.

[4] S. Bethan, G. Vaughan, and S. J. Reid. A comparison of ozone and thermal tropopause heights and the impact of tropopause definition on quantifying the ozone content of the troposphere. *Quarterly Journal of the Royal Meteorological Society*, 122(532):929–944, 1996. Part B Ut570 Times Cited:79 Cited References Count:17.

[5] A. T. Blaker, B. Sinha, V. O. Ivchenko, N. C. Wells, and V. B. Zalesny. Identifying the roles of the ocean and atmosphere in creating a rapid equatorial response to a southern ocean anomaly. *Geophysical Research Letters*, 33(6):–, 2006. 031UM Times Cited:6 Cited References Count:17.

[6] K. Bryan. A numerical method for the study of the circulation of the world ocean (reprinted from the journal of computational physics, vol 4, pg 347-376, 1969). *Journal of Computational Physics*, 135(2):154–169, 1997. Xq327 Times Cited:5 Cited References Count:20.

[7] K. Bryan, F. G. Komro, S. Manabe, and M. J. Spelman. Transient climate response to increasing atmospheric carbon dioxide. *Science*, 215(4528):56–58, 1982.

[8] P. Chen and W. A. Robinson. Propagation of planetary-waves between the troposphere and stratosphere. *Journal of the Atmospheric Sciences*, 49(24):2533–2545, 1992. Kg493 Times Cited:48 Cited References Count:25.

[9] M.-D. Chou and M. J. Suarez. An efficient thermal infrared radiation parameterization for use in general circulation models. *NASA Technical Memorandum 104606*, 3, 1994.

[10] G. A. Corby, A. Gilchrist, and R. L. Newson. A general circulation model of the atmosphere suitable for long period integrations. *Quarterly Journal of the Royal Meteorological Society*, 98(418):809–832, 1972.

[11] Rainer Feistel. Equilibrium thermodynamics of seawater revisited. *Progress In Oceanography*, 31(2):101–179, 1993.

[12] P. M. Forster, M. Blackburn, R. Glover, and K. P. Shine. An examination of climate sensitivity for idealised climate change experiments in an intermediate general circulation model. *Climate Dynamics*, 16(10-11):833–849, 2000. 368LD Times Cited:50 Cited References Count:29.

[13] Edward J. Tarbuck Frederick K. Lutgens. *The Atmosphere*. Prentice Hall, 2000.

[14] C. Frohlich and J. Lean. Solar radiative output and its variability: evidence and mechanisms. *Astronomy and Astrophysics Review*, 12(4):273–320, 2004. 884PD Times Cited:88 Cited References Count:144.

[15] P. R. Gent and J. C. Mcwilliams. Isopycnal mixing in ocean circulation models. *Journal of Physical Oceanography*, 20(1):150–155, 1990. Cm516 Times Cited:1130 Cited References Count:12.

[16] P. R. Gent and J. C. McWilliams. Isopycnal mixing in ocean circulation models. *J. Phys. Oceanogr.*, 20:150–155, 1990.

[17] Adrian E. Gill. *Atmosphere-Ocean Dynamics*. International Geophysics Series, 1982.

[18] A. Goudie and ed. D.Cuff. *Oxford Companion to Global Change*. Oxford University Press, 2008.

[19] J. D. Haigh. The role of stratospheric ozone in modulating the solar radiative forcing of climate. *Nature*, 370(6490):544–546, 1994. Pc537 Times Cited:171 Cited References Count:31.

[20] J. D. Haigh. The impact of solar variability on climate. *Science*, 272(5264):981–984, 1996. Ul619 Times Cited:290 Cited References Count:26.

[21] J. D. Haigh. The effects of solar variability on the earth's climate. *Philosophical Transactions of the Royal Society of London Series a-Mathematical Physical and Engineering Sciences*, 361(1802):95–111, 2003. 637VV Times Cited:82 Cited References Count:58.

[22] J. D. Haigh, M. Blackburn, and R. Day. The response of tropospheric circulation to perturbations in lower-stratospheric temperature. *Journal of Climate*, 18(17):3672–3685, 2005. 972RJ Times Cited:45 Cited References Count:21.

[23] J. Hansen, M. Sato, R. Ruedy, A. Lacis, K. Asamoah, K. Beckford, S. Borenstein, E. Brown, B. Cairns, B. Carlson, B. Curran, S. deCastro, L. Druyan, P. Etwarrow, T. Ferede, M. Fox, D. Gaffen, J. Glascoe, H. Gordon, S. Hollandsworth, X. Jiang, C. Johnson, N. Lawrence, J. Lean, J. Lerner, K. Lo, J. Logan, A. Luckett, M. P. McCormick, R. McPeters, R. Miller, P. Minnis, I. Ramberran, G. Russell, P. Russell, P. Stone, I. Tegen, S. Thomas, L. Thomason, A. Thompson, J. Wilder, R. Willson, and J. Zawodny. Forcings and chaos in interannual to decadal climate change. *Journal of Geophysical Research-Atmospheres*, 102(D22):25679–25720, 1997. Yh593 Times Cited:125 Cited References Count:146.

[24] I. M. Held and M. J. Suarez. A proposal for the intercomparison of the dynamical cores of atmospheric general-circulation models. *Bulletin of the American Meteorological Society*, 75(10):1825–1830, 1994. Pn886 Times Cited:240 Cited References Count:17.

[25] M. P. Hoerling, T. K. Schaack, and A. J. Lenzen. Global objective tropopause analysis. *Monthly Weather Review*, 119(8):1816–1831, 1991. Gb419 Times Cited:108 Cited References Count:25.

[26] JR Holton. *An Introduction to Dynamical Meterology*. Academic Press, 1972.

[27] B. J. Hoskins and A. J. Simmons. Multilayer spectral model and semi-implicit method. *Quarterly Journal of the Royal Meteorological Society*, 101(429):637–655, 1975. Ak844 Times Cited:254 Cited References Count:17.

[28] Pearce RP Hoskins, BJ. *Large Scale Dynamical Processes in the Atmosphere*. Academic Press, 1983.

[29] B. G. Hunt and N. C. Wells. An assessment of the possible future climatic impact of carbon dioxide increases based on a coupled one-dimensional atmospheric-oceanic model. *Journal of Geophysical Research*, 84(C2):787–791, 1979.

[30] D. R. Jackson. Assimilation of eos mls ozone observations in the met office data-assimilation system. *Quarterly Journal of the Royal Meteorological Society*, 133(628):1771–1788, 2007. Part A 238EF Times Cited:8 Cited References Count:48.

[31] S. P. E. Keeley, N. P. Gillett, D. W. J. Thompson, S. Solomon, and P. M. Forster. Is antarctic climate most sensitive to ozone depletion in the middle or lower stratosphere? *Geophysical Research Letters*, 34(22):–, 2007. 237AN Times Cited:6 Cited References Count:17.

[32] P. D. Killworth, D. Stainforth, D. J. Webb, and S. M. Paterson. The development of a free-surface bryan-cox-semtner ocean model. *Journal of Physical Oceanography*, 21(9):1333–1348, 1991. Gm788 Times Cited:204 Cited References Count:19.

[33] K. Kodera and Y. Kuroda. Dynamical response to the solar cycle. *Journal of Geophysical Research-Atmospheres*, 107(D24):–, 2002. 650FZ Times Cited:98 Cited References Count:51.

[34] Y. Kushnir, W. A. Robinson, I. Blade, N. M. J. Hall, S. Peng, and R. Sutton. Atmospheric gcm response to extratropical sst anomalies:

Synthesis and evaluation. *Journal of Climate*, 15(16):2233–2256, 2002. 585MW Times Cited:169 Cited References Count:115.

[35] K. Labitzke. Sunspots, the qbo, and the stratospheric temperature in the north polar-region. *Geophysical Research Letters*, 14(5):535–537, 1987. H6587 Times Cited:219 Cited References Count:4.

[36] K. Labitzke and H. Vanloon. Associations between the 11-year solar-cycle, the qbo and the atmosphere .1. the troposphere and stratosphere in the northern hemisphere in winter. *Journal of Atmospheric and Terrestrial Physics*, 50(3):197–206, 1988. N2616 Times Cited:334 Cited References Count:12.

[37] K. Labitzke and H. Vanloon. Associations between the 11-year solar-cycle, the quasi-biennial oscillation and the atmosphere - a summary of recent work. *Philosophical Transactions of the Royal Society of London Series a-Mathematical Physical and Engineering Sciences*, 330(1615):577–589, 1990. Dc346 Times Cited:26 Cited References Count:13.

[38] K. Labitzke and H. Vanloon. Association between the 11-year solar-cycle and the atmosphere .5. summer. *Journal of Climate*, 5(3):240–259, 1992. Hp486 Times Cited:35 Cited References Count:11.

[39] J. Lean. Contribution of ultraviolet irradiance variations to changes in the suns total irradiance. *Science*, 244(4901):197–200, 1989. U1116 Times Cited:54 Cited References Count:32.

[40] J. Lean. Variations in the suns radiative output. *Reviews of Geophysics*, 29(4):505–535, 1991. Gr588 Times Cited:173 Cited References Count:147.

[41] Jian Lu, Gang Chen, and Dargan M. W. Frierson. The position of the midlatitude storm track and eddy-driven westerlies in aquaplanet agcms. *Journal of the Atmospheric Sciences*, 67(12):3984–4000, 2010.

[42] J. Marshall, D. Ferreira, J. M. Campin, and D. Enderton. Mean climate and variability of the atmosphere and ocean on an aquaplanet. *Journal of the Atmospheric Sciences*, 64(12):4270–4286, 2007. 244WQ Times Cited:7 Cited References Count:29.

[43] J. Marshall and T. Radko. Residual-mean solutions for the antarctic circumpolar current and its associated overturning circulation. *Journal of Physical Oceanography*, 33(11):2341–2354, 2003. 735GF Times Cited:86 Cited References Count:37.

[44] Plumb R. Alan Marshall J. *Atmosphere, Ocean, and Climate Dynamics, An introductory Text.* Academic Press, 2007.

[45] J. J. Morcrette. Impact of changes to the radiation transfer parameterizations plus cloud optical-properties in the ecmwf model. *Monthly Weather Review*, 118(4):847–873, 1990. Dd035 Times Cited:165 Cited References Count:59.

[46] O. H. Ottera, M. Bentsen, I. Bethke, and N. G. Kvamsto. Simulated pre-industrial climate in bergen climate model (version 2): model description and large-scale circulation features. *Geoscientific Model Development*, 2(2):197–212, 2009. V15eg Times Cited:5 Cited References Count:72.

[47] S. Pawson, K. Kodera, K. Hamilton, T. G. Shepherd, S. R. Beagley, B. A. Boville, J. D. Farrara, T. D. A. Fairlie, A. Kitoh, W. A. Lahoz, U. Langematz, E. Manzini, D. H. Rind, A. A. Scaife, K. Shibata, P. Simon, R. Swinbank, L. Takacs, R. J. Wilson, J. A. Al-Saadi, M. Amodei, M. Chiba, L. Coy, J. de Grandpre, R. S. Eckman, M. Fiorino, W. L. Grose, H. Koide, J. N. Koshyk, D. Li, J. Lerner, J. D. Mahlman, N. A. McFarlane, C. R. Mechoso, A. Molod, A. O'Neill, R. B. Pierce, W. J. Randel, R. B. Rood, and F. Wu. The gcm-reality intercomparison project for sparc (grips): Scientific issues and initial results. *Bulletin of the American Meteorological Society*, 81(4):781–796, 2000. 300PY Times Cited:104 Cited References Count:62.

[48] Oort AH Peixoto, JP. *Physics of Climate.* American Institute of Physics, 1992.

[49] Robin Glover Piers Forster and Suzanne Rosier. Documentation for igcm3. 1999.

[50] L. M. Polvani and P. J. Kushner. Tropospheric response to stratospheric perturbations in a relatively simple general circulation model.

Geophysical Research Letters, 29(7):–, 2002. 609DE Times Cited:65 Cited References Count:12.

[51] V. Ramanathan, Eric J. Pitcher, Robert C. Malone, and Maurice L. Blackmon. The response of a spectral general circulation model to refinements in radiative processes. *Journal of the Atmospheric Sciences*, 40(3):605–630, 1983.

[52] S. H. Schneider and S. L. Thompson. Atmospheric co2 and climate: Importance of the transient response. *Journal of Geophysical Research*, 86(C4):3135–3147, 1981.

[53] R. Seager, Y. Kushnir, M. Visbeck, N. Naik, J. Miller, G. Krahmann, and H. Cullen. Causes of atlantic ocean climate variability between 1958 and 1998. *Journal of Climate*, 13(16):2845–2862, 2000. 350YR Times Cited:89 Cited References Count:49.

[54] K. Semeniuk and T. G. Shepherd. The middle-atmosphere hadley circulation and equatorial inertial adjustment. *Journal of the Atmospheric Sciences*, 58(21):3077–3096, 2001. 489QC Times Cited:16 Cited References Count:26.

[55] T. G. Shepherd. Issues in stratosphere-troposphere coupling. *Journal of the Meteorological Society of Japan*, 80(4B):769–792, 2002. 615FN Times Cited:45 Cited References Count:70.

[56] I. R. Simpson, M. Blackburn, and J. D. Haigh. The role of eddies in driving the tropospheric response to stratospheric heating perturbations. *Journal of the Atmospheric Sciences*, 66(5):1347–1365, 2009. 452KI Times Cited:6 Cited References Count:37.

[57] J. M. Slingo. The development and verification of a cloud prediction scheme for the ecmwf model. *Quarterly Journal of the Royal Meteorological Society*, 113(477):899–927, 1987. K2951 Times Cited:414 Cited References Count:57.

[58] R. S. Smith. Ocean circulation and climate dynamics under idealised continental configurations in a coupled ocean atmosphere model. 2004.

[59] R. S. Smith, C. Dubois, and J. Marotzke. Ocean circulation and climate in an idealised pangean oagcm. *Geophysical Research Letters*, 31(18):–, 2004. 857OC Times Cited:4 Cited References Count:23.

[60] R. S. Smith, C. Dubois, and J. Marotzke. Global climate and ocean circulation on an aquaplanet ocean-atmosphere general circulation model. *Journal of Climate*, 19(18):4719–4737, 2006. 090XI Times Cited:3 Cited References Count:49.

[61] J. Thuburn and G. C. Craig. Stratospheric influence on tropopause height: The radiative constraint. *Journal of the Atmospheric Sciences*, 57(1):17–28, 2000. 268DJ Times Cited:46 Cited References Count:29.

[62] J. R. Toggweiler and R. M. Key. Ocean circulation: Thermohaline circulation.

[63] K. E. Trenberth, J. T. Fasullo, and J. Kiehl. Earth's global energy budget. *Bulletin of the American Meteorological Society*, 90(3):311–+, 2009. 430ZT Times Cited:44 Cited References Count:67.

[64] G. K. Vallis. *Atmospheric and Oceanic Fluid Dynamics : Fundamentals and Large-scale Circulation*. 2006.

[65] JM Wallace and PV Hobbs. *Atmospheric Science An Introductory Survey*. Academic Press, 2006.

[66] B. A. Warren. Approximating the energy transport across oceanic sections. *Journal of Geophysical Research-Oceans*, 104(C4):7915–7919, 1999. 187KA Times Cited:27 Cited References Count:10.

[67] D. J. Webb. An ocean model code for array processor computers. *Computers and Geosciences*, 22(5):569–578, 1996. Uq205 Times Cited:48 Cited References Count:16.

[68] G. P. Williams. Circulation sensitivity to tropopause height. *Journal of the Atmospheric Sciences*, 63(7):1954–1961, 2006. 067MT Times Cited:12 Cited References Count:17.

[69] C. Wilson, B. Sinha, and R. G. Williams. The effect of ocean dynamics and orography on atmospheric storm tracks. *Journal of Cli-*

mate, 22(13):3689–3702, 2009. 472JQ Times Cited:2 Cited References Count:29.

[70] Chris Wilson, Bablu Sinha, and Richard G. Williams. The shaping of storm tracks by mountains and ocean dynamics. *Weather*, 65(12):320–323, 2010.

[71] R. A. Wood, A. B. Keen, J. F. B. Mitchell, and J. M. Gregory. Changing spatial structure of the thermohaline circulation in response to atmospheric co2 forcing in a climate model. *Nature*, 399(6736):572–575, 1999. 204RR Times Cited:171 Cited References Count:30.

[72] C. Wunsch. What is the thermohaline circulation? *Science*, 298(5596):1179–+, 2002. 612MQ Times Cited:55 Cited References Count:9.

[73] P. P. Xie and P. A. Arkin. Global precipitation: A 17-year monthly analysis based on gauge observations, satellite estimates, and numerical model outputs. *Bulletin of the American Meteorological Society*, 78(11):2539–2558, 1997. Yh372 Times Cited:1354 Cited References Count:48.

Appendices

A. Derivation of Equations

A.1. Motion in a Rotating System

Given a system rotating at an angular speed $\vec{\Omega}$, a stationary mass with position vector at $\vec{r}$ relative to the system will carry an absolute velocity of $\vec{\Omega} \times \vec{r}$ when observed from an inertial frame. Hence, in the case of a moving mass, the rates of change of position of the mass measured in the inertial frame and the rotating frame are related by equation A.1,

$$\frac{d_A \vec{r}}{dt} = \frac{d\vec{r}}{dt} + \vec{\Omega} \times \vec{r} \tag{A.1}$$

or,

$$\vec{U_A} = \vec{U_r} + \vec{\Omega} \times \vec{r} \tag{A.2}$$

where $\vec{U}$ is the velocity and subscripts A and r denote quantities measured in the inertial and relative frame of reference respectively as before.

In fact equation A.1 could be applied to any vector and replacing the position vector $\vec{r}$ with absolute velocity $\vec{U_A}$ yields:

$$\frac{d_A \vec{U_A}}{dt} = \frac{d\vec{U_A}}{dt} + \vec{\Omega} \times \vec{U_A} \tag{A.3}$$

Substituting equation A.2 into A.3,

$$\frac{d_A \vec{U_A}}{dt} = \frac{d}{dt}(\vec{U_r} + \vec{\Omega} \times \vec{r}) + \vec{\Omega} \times (\vec{U_r} + \vec{\Omega} \times \vec{r}) \tag{A.4}$$

and with the aid of the vector identity $\vec{\Omega} \times (\vec{\Omega} \times \vec{r}) = -\Omega^2 \vec{R}$, equation A.4 could be rewritten as:

$$\frac{d_A \vec{U_A}}{dt} = \frac{d\vec{U_r}}{dt} + 2\vec{\Omega} \times \vec{U_r} - \Omega^2 \vec{R} \tag{A.5}$$

where $\vec{R}$ is a vector perpendicular to the axis of rotation and has magnitude proportion to cosine of latitude ϕ, i.e. $\vec{R} = |\vec{R}|cos\phi$.

A.2. Hydrostatic Equilibrium

Consider a column of air of density ρ, area A, height δz, and mass m as shown in figure A.1. The only forces acting on the column are the gravitational force g and the pressure forces p acting at the top and bottom respectively. Assuming the net force acting on the column is zero, balancing the vertical forces gives:

$$A[p(z) - p(z + \delta z)] = \rho A \delta z g \tag{A.6}$$

Rearranging equation A.6 and assuming δz is small yields,

$$\frac{p(z + \delta z) - p(z)}{\delta z} = -\rho g \tag{A.7}$$

$$\frac{dp(z)}{dz} = -\rho g \tag{A.8}$$

the equation of hydrostatic balance, as shown in equation A.8.

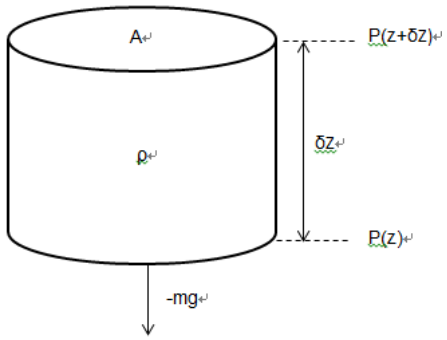


Figure A.1.: A vertical column of air of density ρ, area A, height δz, and mass m. The pressure acting at the top and bottom of the column are $p(z + \delta z)$ and $p(z)$ respectively.

B. Technical Issues

B.1. Vertical Sea Water Velocity

During our investigation into the vertical advection of potential temperature in the ocean (section 3.4.2), we identified errors in FORTE's output of vertical sea water velocity at specific points. An example is shown in B.1, which highlights the difference between the vertical sea water velocities at 79^oN and 79^oS. In addition to the contrast in magnitude, there seem to be a discontinuity in the vertical velocity pattern between longitudes 0^o and 140^o at 79^oN. This is not expected in our aquaplanet, which is zonally symmetrical in every aspect.

Hence, in our analysis, we manually calculated the vertical sea water w_o velocity using the continuity equation with the assumption that sea water is incompressible,

$$\frac{\partial u_o}{Rcos\phi\partial\lambda} + \frac{\partial v_o cos\phi}{Rcos\phi\partial\phi} + \frac{\partial w_o}{\partial p} = 0 \tag{B.1}$$

where u_o and v_o are the horizontal sea water velocity in the zonal and meridional directions respectively. R is the radius of Earth. Figure B.2 shows a sample of zonal mean vertical sea water velocity calculated using equation B.1.

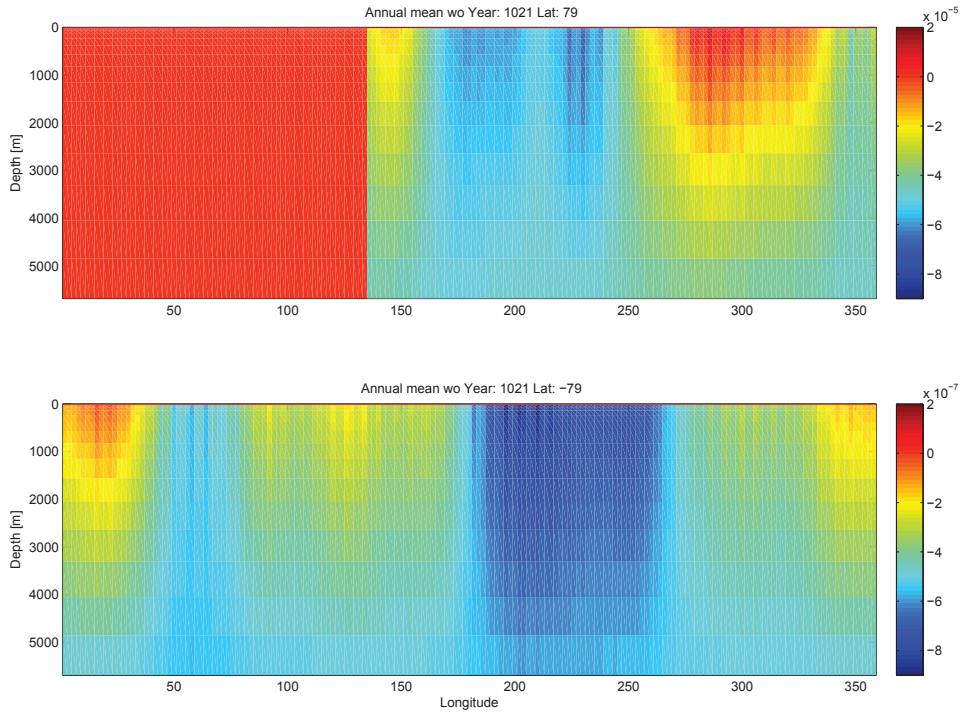


Figure B.1.: Annual mean vertical sea water velocity at $79^o N$ (top) and $79^o S$ (bottom) $[ms^{-1}]$.

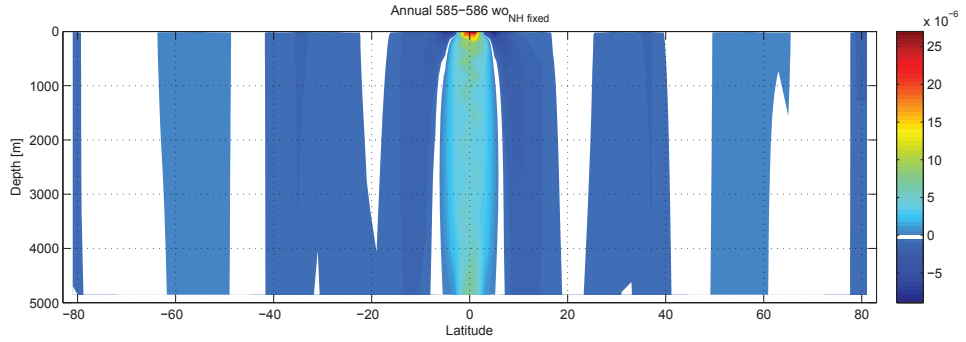


Figure B.2.: Time averaged zonal mean vertical sea water velocity calculated using equation B.1 $[ms^{-1}]$.

C. IGCM3 Updates

This section lists the additional codes (shown in bold, some original code is also shown in normal text as an indication of the line number of the concerned IGCM3 update file) required for our fixed SST experiment and additional model outputs.

C.0.1. Extracting SST Data

T42.oasis-test.upd

```
*I MLTRI.56
          IF (abs(MOD(DOY,1.)-delt/pi2).lt.1e-4) THEN
              CALL fromcpl(nint(DAY-ifirstday)*nexca, imjm, zsst, glace)

C ======= Write SST to file ======
        open(301,FILE='zsst.dat',ACCESS='APPEND')
        PRINT *,'size sst= ',size(zsst)
        do I=1,8192
          write(301,*)zsst(I)
        enddo
        close(301)
C ================================
```

C.0.2. Reading SST Data

T42.oasis-test.upd

```
*I MLTRI.56
          IF (abs(MOD(DOY,1.)-delt/pi2).lt.1e-4) THEN
              CALL fromcpl(nint(DAY-ifirstday)*nexca, imjm, zsst, glace)

C ======== Fix SST Experiment =======
      open(301,FILE='zsst.dat')
C Read blanks
      if ((DOY-0.015625).gt.1.) then
        do I=1,8192*(DOY-0.015625-1.)
            read(301,*)
        enddo
      endif
C Re-initialise sst array
      do I=1,8192
        zsst(I)=0.
      enddo
C Read from datafile
      do I=1,8192
        read(301,*) zsst(I)
      enddo
      close(301)
C ======= Fix SST Experiment End =======
```

C.0.3. Radiative Flux Output at Every Model Level

T42-accumulate-new.upd

```
*I MLTRI.126
                avtg1(i,ih)=avtg1(i,ih)+tg1(i,ih)/(real(kounth))
                avug1(i,ih)=avug1(i,ih)+ug1(i,ih)/(real(kounth))
                avvg1(i,ih)=avvg1(i,ih)+vg1(i,ih)/(real(kounth))
                avqg1(i,ih)=trag(i,1)+trag(i,1)/(real(kounth))

C ========== Extra flux output ========
*B MLTRI.128
      DO I=1,4160
         avflup(i,ih)=avflup(i,ih)+FLUP(i,ih)/(real(kounth))
         avfldwn(i,ih)=avfldwn(i,ih)+FLDWN(i,ih)/(real(kounth))
         avfsup(i,ih)=avfsup(i,ih)+FSUP(i,ih)/(real(kounth))
         avfsdwn(i,ih)=avfsdwn(i,ih)+FSDWN(i,ih)/(real(kounth))
      ENDDO
```

T42-common.upd

```
*COMDECK OUTfields
      common/outfields/avswlw(imjm),avheatlat(imjm),avwater(imjm)
     $     ,avsensible(imjm),avtaux(imjm),avtauy(imjm)
     $     ,avexwater(imjm),avtg1(igd,jg),avug1(igd,jg)
     $     ,avvg1(igd,jg),avqg1(igd,jg)
     $     ,avswtopup(imjm),avswtopdn(imjm)
     $     ,avlwtopup(imjm)
     $     ,avswsurfup(imjm)
     $     ,avswsurfdn(imjm)
     $     ,avlwsurfup(imjm)
     $     ,avlwsurfdn(imjm)
     $     ,avflup(4160,jg),avfldwn(4160,jg)
     $     ,avfsup(4160,jg),avfsdwn(4160,jg)
*COMDECK tavg
      common/tavg/    tstar_avg(igc,jg),pstar(igc,jg)
     $                     ,pstar_avg(igc,jg),navg
      integer navg
      real tstar_avg,pstar,pstar_avg
*COMDECK netcdf_var
      common /netcdf_var/ timeid,tid,pid,svid,suid
     $           ,uid,vid,aid,sdbid,subid,sntid,ldbid
     $           ,thid,lhid,shid,wfid,lubid,lutid
     $           ,qid,exid,nrec,ncunit
     $           ,r1id,r2id,r3id,r4id,r5id,r6id,r7id
     $           ,fldwnid,flupid,fsdwnid,fsupid

      integer*4 timeid,tid,pid,svid,suid
     $           ,uid,vid,aid,sdbid,subid,sntid,ldbid
     $           ,thid,lhid,shid,wfid,lubid,lutid
     $           ,qid,exid,nrec,ncunit
     $           ,r1id,r2id,r3id,r4id,r5id,r6id,r7id
     $           ,fldwnid,flupid,fsdwnid,fsupid
```

T42-netcdf-proper1.upd

```
do ij=1,igd
   avtg1(ij,ji) =0.
   avug1(ij,ji) =0.
   avvg1(ij,ji) =0.
end do

do ij=1,4160
   avflup(ij,ji)=0.
   avfldwn(ij,ji)=0.
   avfsup(ij,ji)=0.
   avfsdwn(ij,ji)=0.
end do
```

T42-netcdf-proper1.upd

```
      include 'netcdf.inc'

      integer*4 nlon,nlat,nlev,ntime
      integer*4 nflev
      parameter(nlon=128,nlat=64,nlev=15,ntime=1)
      parameter(nflev=16)
      real lon(nlon)
      real lev(nlev)
      real flev(nflev)
      integer*4 ierr,i
      integer*4 lonid,latid,levid
      integer*4 flevid
      integer*4 leveldim(4),singledim(3)
      integer*4 fleveldim(4)
      character*20 varname,filename

      data lev/0.0179 ,0.0577 ,0.1050 ,0.1570 ,0.2077
     1,0.2526 ,0.2923 ,0.3315 ,0.3759 ,0.4325
     1,0.5114 ,0.6220 ,0.7558 ,0.8844 ,0.9717/

      data flev/0.0092 ,0.0390 ,0.0825 ,0.1286 ,0.1741
     1, 0.2184 ,0.2632 ,0.3118 ,0.3685 ,0.4376
     1, 0.5217 ,0.6202 ,0.7279 ,0.8342 ,0.9255
     1, 0.9982/

      do i=1,nlon
         lon(i)=(i-1)*360./float(nlon)
      enddo

      ierr=nf_create(filename,0,ncunit)
      ierr=nf_def_dim(ncunit,'longitude',nlon,lonid)
      ierr=nf_def_dim(ncunit,'latitude',nlat,latid)
      ierr=nf_def_dim(ncunit,'level',nlev,levid)
      ierr=nf_put_att_text(ncunit,levid,'long_name',14,'Level (Centre)')
      ierr=nf_def_dim(ncunit,'flevel',nflev,flevid)
      ierr=nf_def_dim(ncunit,'time',nf_unlimited,timeid)
```

```
      leveldim(1)=lonid
      leveldim(2)=latid
      leveldim(3)=levid
      leveldim(4)=timeid

      fleveldim(1)=lonid
      fleveldim(2)=latid
      fleveldim(3)=flevid
      fleveldim(4)=timeid

      singledim(1)=lonid
      singledim(2)=latid
      singledim(3)=timeid

      ierr=nf_def_var(ncunit,'fldwn',nf_double,4,fleveldim,fldwnid)
      ierr=nf_put_att_text(ncunit,fldwnid,'units',5,'W/m^2')
      ierr=nf_put_att_text(ncunit,fldwnid,'long_name',22,
     1       'downward_longwave_flux')
      ierr=nf_def_var(ncunit,'flup',nf_double,4,fleveldim,flupid)
      ierr=nf_put_att_text(ncunit,flupid,'units',5,'W/m^2')
      ierr=nf_put_att_text(ncunit,flupid,'long_name',20,
     1       'upward_longwave_flux')
      ierr=nf_def_var(ncunit,'fsdwn',nf_double,4,fleveldim,fsdwnid)
      ierr=nf_put_att_text(ncunit,fsdwnid,'units',5,'W/m^2')
      ierr=nf_put_att_text(ncunit,fsdwnid,'long_name',23,
     1       'downward_shortwave_flux')
      ierr=nf_def_var(ncunit,'fsup',nf_double,4,fleveldim,fsupid)
      ierr=nf_put_att_text(ncunit,fsupid,'units',5,'W/m^2')
      ierr=nf_put_att_text(ncunit,fsupid,'long_name',21,
     1       'upward_shortwave_flux')
```

T42-netcdf-proper1.upd

```
ierr=nf_enddef(ncunit)

ierr=nf_put_var_double(ncunit,lonid,lon)
ierr=nf_put_var_double(ncunit,latid,alat)
ierr=nf_put_var_double(ncunit,levid,lev)
ierr=nf_put_var_double(ncunit,flevid,flev)
```

T42-netcdf-proper1.upd

```
call write_nc_lv(avttrd,day,1.,nrec,ncunit,timeid,ttrdid)
call write_nc_lv(avttlr,day,1.,nrec,ncunit,timeid,ttlrid)
call write_nc_lv(avttcr,day,1.,nrec,ncunit,timeid,ttcrid)
call write_nc_lv(avttvd,day,1.,nrec,ncunit,timeid,ttvdid)
call write_nc_lv(avtnlg,day,1.,nrec,ncunit,timeid,tnlgid)

call write_nc_flv(avflup,day,1.,nrec,ncunit,timeid,flupid)
call write_nc_flv(avfsup,day,1.,nrec,ncunit,timeid,fsupid)
call write_nc_flv(avfldwn,day,1.,nrec,ncunit,timeid,fldwnid)
call write_nc_flv(avfsdwn,day,1.,nrec,ncunit,timeid,fsdwnid)

do i=1,igd
do j=1,jg
   avtg1(i,j)=0.
   avug1(i,j)=0.
   avvg1(i,j)=0.
end do
end do

do i=1,4160
do j=1,jg
   avflup(i,j)=0.
   avfldwn(i,j)=0.
   avfsup(i,j)=0.
   avfsdwn(i,j)=0.
end do
end do
```

T42-netcdf-proper1.upd

```
      subroutine write_nc_flv(field,day,ct,nrec,ncunit,timeid,tempid)
      include 'netcdf.inc'
      integer*4 nlon,nlat,nflev
      parameter(nlon=128,nlat=64,nflev=16)
      real field(nflev*(nlon+2)*2,nlat/2)
      real tmp_field(nlon,nlat,nflev)
      real time
      real day
      real ct
      integer*4 i,j,k,flev,ierr
      integer*4 ncunit,nrec
      integer*4 tempid,timeid,start(4),count(4)
      do flev=1,nflev
      do i=1,nlon
         do j=1,nlat/2
            tmp_field(i,j,flev)=field(
     $                              ((nlon+2)*2)*(nflev-flev)+i,j )*ct
         enddo
         k=nlat/2+1
         do j=nlat/2,1,-1
            tmp_field(i,k,flev)=field(
     $                              ((nlon+2)*2)*(nflev-flev)+i+nlon+2,j)*ct
          k=k+1
         enddo
      enddo
      end do
      start(1)=1
      start(2)=1
      start(3)=1
      count(1)=nlon
      count(2)=nlat
      count(3)=nflev
      count(4)=1
      time=day
      ierr=nf_put_vara_double(ncunit,timeid,nrec,1,time)
      start(4)=nrec
      write(*,*) nrec
      ierr=nf_put_vara_double(ncunit,tempid,start,count,tmp_field)
      status = nf_sync(ncunit)
      return
      end
```

jacob.upd

```
*D RADSW.6
*B RADSW.7
      :                         ZCARDI,ZSCT,PDP,PR,SWALB,FLS,GA,GASCON,
      :                         ZFSDWN,ZFSUP)

*B NIKOS.67
C Declaration from RADSW.dk
       REAL ZFSUP(1,NLP+1),ZFSDWN(1,NLP+1)

*D NIKOS.240
*B NIKOS.241
      :                    ZCARDI,PSOL,SWDP,PFLUX,SWALB,FLS,GA,GASCON,
      :                    ZFSDWN,ZFSUP)

*D NIKOS.6
*B NIKOS.7
      $       RFLUXES,SWALB,ALON,FUP,FDWN,ZFSUP,ZFSDWN)

*I CPIERS.4
C (nlon+2)*2*16 = 4160
      :                     ,FLUP(4160,32),FLDWN(4160,32)
      :                     ,FSUP(4160,32),FSDWN(4160,32)
*I MORC.31
       REAL FUP(16)
       REAL FDWN(16)
       REAL ZFSUP(17)
       REAL ZFSDWN(17)
*D MORC.430
*B MORC.431
      $       fluxes,swalb,alon,FUP,FDWN,ZFSUP,ZFSDWN)
C (nlon+2)*2 = 260
       DO ILAY=NL+1,1,-1
            FLUP((NL+1-ILAY)*(260)+IM,JH)=FUP(ILAY)
            FLDWN((NL+1-ILAY)*(260)+IM,JH)=FDWN(ILAY)
            FSUP((NL+1-ILAY)*(260)+IM,JH)=ZFSUP(ILAY+1)
            FSDWN((NL+1-ILAY)*(260)+IM,JH)=ZFSDWN(ILAY+1)
       ENDDO
C ================================
C SW fix from Southampton
*D NIKOS.245
       RFLUXES(1,1,2)=FLS(2)/(1.0-SWALB)     ! SW down bottom
C ================================
```